THE CRITICAL HEAT FLUX UNDER POOL BOILING AND CONFINED BOILING CONDITIONS

THESIS

submitted in part fulfilment of the
requirements for admittance to the degree

of

DOCTOR OF PHILOSOPHY

of the

UNIVERSITY OF GLASGOW

by

JAMES A. RILEY
M.Sc., M.I.Mech.E.

1973

TO

ALICE

MARTYN and SUSAN

A C K N O W L E D G E M E N T S

The author wishes to thank sincerely his supervisors Professor R. S. Silver and Professor H. W. Wilson for their advice and encouragement given throughout this project.

The author is also grateful to Mr. J. A. Izatt, Deputy Director of the Scottish Universities Research and Reactor Centre for help in many different ways throughout the research programme. Mr. J. R. Tyldesley of the University of Glasgow kindly read and criticised the text and for this the author offers his thanks. Invaluable help was given to the author by his technicians, Mr. W. McLaughlin and Mr. H. Hastings in constructing and in operating the heat transfer rigs. Mr. H. Hastings also gave assistance with some of the calculations.

The author acknowledges with gratitude the support given by Professor H. W. Wilson in the form of time to carry out the research programme, and also, inconjunction with the University of Glasgow, and the Scientific Research Council, for the provision of the necessary research equipment.

Finally the author thanks Miss Linda I. W. Nelson for undertaking the typing of this thesis, and for fulfilling this arduous task in a competent manner.

PREFACE

This thesis contains an account of research work carried out by the author at the Scottish Universities Research and Reactor Centre at East Kilbride, Scotland. The subject of the research was an investigation into the critical or limiting heat flux phenomenon under pool boiling and confined boiling conditions. This phenomenon is of interest in the field of Nuclear Reactor Technology because it is a phenomenon that can limit the maximum power output of liquid cooled nuclear reactors.

The research reported is divided into two sections, Part I dealing with the critical heat flux phenomenon for horizontally mounted heater specimen under pool boiling conditions and Part II dealing with the critical or limiting heat flux phenomenon for vertically mounted specimen under pool boiling and confined boiling conditions.

In Part I both the rig and the heater assemblies were designed and commissioned by the author who also built the rig with Technician and Workshop assistance. The rig was operated by the author with Technician assistance and the experimental results were obtained by the author. The analysis, discussion and presentation of the results in Part I is due to the author and where these results are compared to other researchers work due recognition is given by an appropriate reference to the researcher involved.

In Part II the rig and annuli heater assemblies were designed and commissioned by the author. The rig was also built by the author with Technician assistance. All the experimental results reported were obtained by the author with Technician assistance. Analysis, discussion and presentation of the results is due to the author. The theory developed in this part of the thesis is also mainly due to the author and where the author has drawn on the work of others this has been duly acknowledged in the text.

The results of the horizontal pool boiling investigation reported in Part I tend to support the critical heat flux model due to Zuber (17,18) and to show that this model is still applicable to results obtained under vacuum conditions. How-

ever the results also show some limitations to this 'hydrodynamic' model in the sense that reduced heat fluxes were obtained as the heater tube wall thickness was reduced and also for heaters with contaminated surfaces. Neither of these effects are predicted by the Zuber model although the recent approach to this problem due to Ouwerkerk (13) could form a basis for taking account of the wall thickness effect.

The results of the vertical heater-annular geometry investigation reported in Part II of this thesis have been successfully correlated and compared with the predictions of the theoretical model developed. Both the results for saturated liquid entry and for subcooled liquid entry to the annulus have been found to be compatible with the theoretical model predictions.

CONTENTS

1. GENERAL INTRODUCTION

The research reported in this thesis is divided into two parts, Part I dealing with the critical heat flux phenomenon for horizontally mounted heater specimen under pool boiling conditions, and Part II dealing with the critical or limiting heat flux phenomenon for vertically mounted specimen under pool boiling and confined boiling conditions.

One of the objects of the investigation reported in Part I was to check that the rig and its associated instrumentation was working satisfactorily by confirming other experimenters results. However initial results from the rig, obtained at atmospheric pressure, did not agree with those reported by other workers. The author traced this disagreement ultimately to a combination of effects. These effects were due to the dependance of the critical heat flux for horizontal cylindrical stainless steel heaters upon (a) the heater diameter, (b) the heater wall thickness (c) the heater and rig cleanliness and (d) the rig water quality. Effects (a) and (b) led the author to the excellent papers of Benarth (1), Kutateladze et al (3), and Sun et al (9), all of whom dealt with the heater diameter effect and in the case of Benarth (1) also briefly with the effect of heater wall thickness. However the heater wall thickness effect on the critical heat flux is generally not well investigated or documented. Effects (c) and (d) generally gave rise to reduced and inconsistent critical heat flux values (see Part I Appendix). Effect (b) could give rise to reduced critical heat flux values relative to those due to solid cylinders. Therefore after allowing for effects (a) and (b) and eliminating effects (c) and (d) the author obtained results, at atmospheric pressure, which were consistent with the results of other investigators. Thus having proved the rig at atmospheric pressure, and developed suitable rig and specimen cleaning procedures and settled on the use of double distilled water (conductivity $< 1.5\mu$.mho) which was renewed after each specimen had been completely tested the author undertook the investigation the results of which are reported in Part I. In this investigation, heater diameter and heater

tube wall thickness effects upon the critical heat flux were investigated at atmospheric pressure and under vacuum conditions for both saturated and subcooled pool conditions. The heaters used were stainless steel and were mounted horizontally. The experimental results obtained confirmed the accuracy of the rig and its associated instrumentation when results obtained were directly comparable to those of other investigators. Further they confirmed the importance of rig and specimen cleanliness in obtaining reproducibility of results (see Part I - Appendix). The results of this test programme further substantially extended the range of experimental critical heat flux results available (i.e. under vacuum conditions with heater tube diameter and wall thickness variation) for comparison with the theory of Zuber and the Zuber based theory of Sun et al (9) and in general the comparison confirmed the validity of these theories over the extended range investigated. However it is pointed out that the observed effect of, tube wall thickness reduction and of heater surface contamination, causing reduced critical heat fluxes, is not predicted by either of these two theories. However the wall thickness effect could be taken as some evidence in support of the recent critical heat flux model due to Ouwerkerk (13) which does predict the heater tube wall thickness as a relevant parameter.

Now the critical heat flux is a very important parameter with self heated heaters in boiling systems because in such systems at the critical heat flux condition the local heat transfer coefficient is substantially reduced. Since for self heated heaters the local heat generation rate continues unabated, then the heater temperature must rise markedly to maintain heat removal. In most practical situations the heater temperature necessary is above the heater material melting temperature and thus heater failure ensues. Further, in the field of nuclear reactors, melting of an area of fuel would release highly toxic radioactive fission products into the coolant stream and possibly from there to the outer environment depending on the extent of the accident. So apart from

local element melting, there is this additional reason for ensuring that no fuel surface in a liquid cooled nuclear reactor should be allowed to operate at the critical heat flux. In boiling water reactors, boiling occurs in the reactor core under normal operating conditions. In other reactor types such as pressurized water reactors, water cooled research reactors, or liquid metal cooled reactors, under normal operation conditions, only single phase liquid heat transfer conditions apply. However, for such reactors, examination of the effects of possible accident conditions must be undertaken, for example, loss of pressure, coolant circulating pump failure, or a blocked coolant channel. Under these conditions boiling could occur in reactors that normally operate only with single phase liquid heat transfer. In order to design and operate liquid cooled nuclear reactors safely it is necessary to be able to predict the critical heat flux level within the reactor core and to know the parameters upon which the critical heat flux depends both for normal operation and for possible fault conditions. This normally entails prediction of the critical heat flux for forced and/or natural circulation (parallel or counter flow) two phase flow within reactor coolant channels of different sizes and geometries.

Now several theories predicting the critical heat flux for forced flow in channels are built on the critical heat flux predictions for pool boiling, (Ivey et.al (2)), that is the summation of a pool boiling term and a forced flow term. The results obtained in Part I therefore tend to confirm the applicability over an extended range of the models due to Zuber and due to Sun et.al and therefore to increase confidence in the correctness of their basic assumptions. However some of the experimental results obtained, namely those with (a) heater tube wall thickness variation, and (b) with heater surface contamination, tend to cast some doubt on whether an entirely hydrodynamic theory whose critical mechanism depends on conditions some distance away from the heater surface is sufficient for all practical situations. From a practical

point of view both effects (a) and (b) are important because they both produce reduced critical heat flux values. It is therefore particularly important with water cooled reactors to keep fuel elements free from contaminants. Particular care should therefore be taken with water cooled research reactors where the fuel elements are removed from and returned to the core at frequent intervals.

In Part II of this thesis the critical heat flux investigation is extended to pool and confined geometry boiling for vertically mounted heater specimen. For the confined boiling situation the vertically mounted cylindrical heater was surrounded by a glass tube that therefore formed an outer adiabatic surface of an annulus assembly. This annulus assembly was sealed at its base so that vapour formed in boiling left the annulus at its top inopposition to the replacement water - a countercurrent two phase flow system or open thermosyphon. Both the heater diameter and the annulus outer diameter were varied under atmospheric pressure and vacuum conditions for both subcooled and saturated liquid entry. Now as the annulus outer diameter is increased then an upper limit critical heat flux value will be attained which will be the pool boiling value for a vertically mounted heater specimen.

Now such an annulus geometry that is sealed at its base produces a physical situation which could be similar to that occurring when a liquid cooled nuclear reactor fuel element channel with upward coolant flow becomes blocked, by some foreign body, at its base. Under such circumstances a two phase countercurrent flow system could be set up and the channel critical heat flux could be significantly reduced below the "normal operation" value. Therefore for an annular geometry fuel channel the presented experimental results could give a measure of the expected critical heat flux value and how this value could vary with annulus geometry. Further the dimensionless parameters, developed from the theoretical model presented, and used successfully by the author in correlating the experimental results could be of use to future investigators in this field of work.

It is further possible that the results of this work could find some application in the field of closed thermo-syphons and possibly in the field of heat pipes although here the heat pipe wick is a complicating factor whose effect clearly requires extensive investigation. Now whereas in a thermo-syphon the liquid return force is due to gravity and therefore such devices must be gravity orientated to function, the heat pipe liquid return force is due to capilliary or surface tension forces and therefore such a device has the advantage of variable orientation in use. These relatively new devices that can be used for cooling electronic and other suitable heat generating devices can work internally under vacuum conditions when the heat transfer occurs at relatively low temperatures (below 100^{o}C when using water). Now with a thermo-syphon one of the modes of failure to transmit all the heat input while keeping the heat generating device at a safe operating temperature is the breakdown of the water film - a similar physical situation to that investigated both experimentally and theoretically in Part II of this thesis.

PART I

HORIZONTAL HEATER PLACEMENT UNDER POOL BOILING CONDITIONS

2.0.0.

N O M E N C L A T U R E

P A R T I

NOMENCLATURE - PART I

A dimensionless radius parameter, $(0.89 + 2.27 \exp(-3.44\sqrt{R^1}))$

C specific heat of liquid

g gravitational acceleration

h heat transfer coefficient

h_f heat transfer coeff,t. for film boiling

h_n heat transfer coeff,t. for nucleate boiling

h_{fg} enthalpy of vaporization

I induced convection scale parameter, $\left(\frac{\rho_f . \sigma . R}{\mu_f}\right)^{\frac{1}{2}}$

K thermal conductivity of liquid

K_g thermal conductivity of vapour

K_s thermal conductivity of solid

L heater characteristic length

L^1 heater dimensionless length, $L. \left(\frac{g(\rho_f - \rho_g)}{\sigma}\right)^{\frac{1}{2}}$

N induced convection buoyancy parameter $\frac{\rho_f . \sigma}{\mu^2_f}\left(\frac{\sigma}{g(\rho_f - \rho_g)}\right)$

N_B Biot modulus, $\frac{h.t}{K_s}$

p pressure

q critical heat flux

q^1 critical heat flux given by 1.123. A.q.

R radius of solid cylinder or outer radius of tube

R^1 dimensionless radius, $R\left(\frac{g.(\rho_f - \rho_g)}{\sigma}\right)^{\frac{1}{2}}$

S^*_f critical half length of dry area

t tube wall thickness or radius of solid cylinder

t_g boiling film thickness

T_c maximum surface temperature for liquid contact

T_o saturation temperature

ΔT_s pool subcooling

Z $\Delta T_s . p^{-0.638}$

Z^1 $\frac{C}{h_{fg}}\left(\rho_f / \rho_g\right)^{\frac{1}{4}} . \Delta T_s$

Greek Symbols

ρ density

σ surface tension

μ viscosity

θ_c surface bubble contact angle

Subscripts

f liquid

g vapour

∞ heater with $R^1 > 1.0$ (large surface) and zero pool subcooling

∞.s heater with $R^1 > 1.0$ (large surface) and with zero or finite pool subcooling

d heater with $R^1 > 0.13$ and zero pool subcooling

d.s heater with $R^1 > 0.13$ and zero or finite pool subcooling

l large flat surface heater (Zuber theory applies) and zero pool subcooling

l.s large flat surface heater (Zuber theory applies) and zero or finite pool subcooling

3.0.0.

INTRODUCTION AND LITERATURE SURVEY

INTRODUCTION AND LITERATURE SURVEY

The critical heat flux phenomenon under pool boiling conditions has been investigated by many researchers over the last two decades, the major driving force being the development of water cooled and liquid metal cooled nuclear reactors. Interest in boiling under vacuum conditions arises in fields such as water desalination and more recently in thermosyphons and heat pipes. The relative simplicity of the pool boiling experiment using electrically driven cylindrical heaters makes it an attractive system experimentally. However because of the complexity of the critical heat flux phenomenon a complete understanding of the mechanism has not yet been attained - however much progress has been made.

An early and significant paper was that due to Benarth (1), which reviewed all the information that was then available. He also 'pointed the way' to many subsequent research programmes, for example, the effect of test section parameters on the critical heat flux (2), the effect of heater orientation (3,4), and the effect of heater material (5). Some workers have carried out their experiments using tubular heaters (5,6), some have used solid rods (4,7) and some have used mixtures of both (2).

The effect of heater diameter on the saturated critical heat flux under atmospheric pool boiling conditions in water was recognised by McAdams et al (8). Further Benarth (1) modified the McAdams curve in light of further results. Benarth (1) also drew attention to the effect of heater tube wall thickness on the critical heat flux and to the similarity between the critical heat flux curves with heater diameter variation and with heater wall thickness variation at constant diameter.

Kutateladze et al (3) reported an investigation of the critical heat flux under saturated pool boiling conditions in which both horizontal and vertical heater placement were investigated with heater diameter variation. To the authors

knowledge these were the first investigators to report that for saturated pool boiling the ratio of the critical heat flux in vertical placement to that in horizontal placement was a function of heater diameter and that for heater diameters greater than 3 m.m. this ratio was unity. These authors also used the dimensionless correlating parameter called 'Webers Criterion'. Webers Criterion is, in fact, a heater dimensionless diameter and is twice the dimensionless radius (R^1) as used recently by Sun et al (9).

Kutateladze et al (10) reported an extensive investigation in which the heater diameter was varied for variables of working fluid, system pressure, and sub-cooling under pool boiling conditions. They used solid cylindrical heaters for all their tests with the exceptions of one tube and one flat strip heater. They successfully correlated their results with the aid of the heater dimensionless diameter (Webers Criterion). However to give absolute values to their results it is necessary to know the value of the saturated critical heat flux for 'large' heaters for the ranges they covered. No values are given explicitly in their paper.

Van Stralen et al (4) investigated the critical heat flux for pure liquids and mixtures under various conditions for pool boiling and clearly show that the slope of the critical heat flux-pool temperature characteristic is a function of the heater diameter. Further the heaters (Platinum Wires) were rotated from horizontal to vertical placement and critical heat flux measurements made at these extremes and at intermediate angles. The ratio of the saturated critical heat flux in vertical placement to that with the heater in horizontal placement is reported as 0.72 for the wire diameter range covered.

Ponter et al (6) reported critical heat flux values for saturated and subcooled pool boiling of water, at atmospheric and reduced pressures for a stainless steel tubular heater (5.85 m.m. O.D. by 0.38 m.m. wall thickness) in horizontal

placement. Their saturated boiling results under vacuum agreed with the 'Zuber' critical heat flux model but their subcooled results differed from the 'Zuber' model predictions by up to 20% at 100 torr. pressure. They successfully correlated all their results with the following equation:

$$q_{\infty.s} / q_l = 1.06 + 1.015.\Delta T_s.p^{-0.474} \qquad 1$$

where p is in torr. and ΔT_s is in ^{o}C

Sun et al (9) recently reported critical heat fluxes for a range of, cylindrical heaters, gravities, pressures, and liquids for pool boiling conditions and horizontal heater placement. They also used a modified 'Zuber' approach together with an experimental determination of the vapour blanket thickness around the heater to produce a critical heat flux model for saturated pool boiling in horizontal placement. This model correlated experimental critical heat flux values to about $\pm$ 20% for a heater dimensionless radius (R^1) greater than 0.15.

Borishanski (11) and more recently Lienhard et al (12) investigated the effect on the critical heat flux for flat plate heaters of induced secondary flows due to liquid viscosity effects. To account for this effect which was small in Borishanski's case, Borishanski introduced the parameter 'N' which Lienhard et al (12) later called the 'induced-convection buoyancy parameter'. Lienhard et al (12) also introduced the induced-convection scale parameter', 'I', as an alternative to 'N'. 'I' has the advantage, when investigating systems in which the heater size is important, because it contains a heater characteristic length.

Recently Ouwerkerk (13), based partly on the earlier work of Semaria et al (14) on calefaction spots on heater walls, proposed a new mechanism to explain the critical heat flux phenomenon. This mechanism depends on the instability of dry spot formation on a heater surface, and thus, unlike the

Zuber model, depends on the heater material properties.

4.0.0.

MODELS OF CRITICAL CONDITION

MODELS OF CRITICAL CONDITION

Descriptions of the physical mechanism that causes the critical heat flux phenomenon have been offered by (13), (15), (16) and (17, 18).

Rohsenow et al (15) imagined the critical condition being caused by the heater surface bubble population becoming so large that adjacent bubbles touched each other thus causing film boiling to occur.

Deissler (16) imagined the critical condition to be caused by bubbles from a nucleation site running into each other this mutual interference retarding the motion of the departing bubbles and thus causing film boiling to occur.

Zuber et al (17,18) imagined the critical condition to be due to vapour columns that rise from the heater surface near to the critical heat flux condition causing a retardation of the incoming liquid. This effect becomes worse with heat flux increase until finally the system becomes hydrodynamically unstable, the heater is starved of liquid and the boiling regime changes to film boiling. This is, in effect, a 'flooding' model and is the most widely developed of all the models described. The mathematical development of this model to large flat surfaces for both saturated and subcooled pool conditions is given in (19). The following equations 2 and 3 are obtained directly or indirectly from (19). For saturated conditions the critical heat flux is given by

$$q_l = 0.131 . h_{fg} . \rho_g \left(\frac{\sigma . g . (\rho_f - \rho_g)}{\rho_g^2} \right)^{\frac{1}{4}} \qquad 2$$

For subcooled pool conditions, the critical heat flux is given by the following equation obtained by combining equations (25) and (27) of (19).

$$q_{ls}/q_l = 1.0 + \frac{5.32}{\rho_g . h_{fg}} (\rho_f . C . K.)^{\frac{1}{2}} \left(\frac{g(\rho_f - \rho_g)}{\sigma} \right)^{\frac{1}{4}} \left(\frac{\rho_g^2}{\sigma . g (\rho_f - \rho_g)} \right)^{\frac{1}{8}} . \Delta T_s \qquad 3$$

Now we can rearrange equation 3 and express it in the

following form:

$$\left(q_{ls}/q_l - 1\right).\Delta T_s^{-1} = f(p) \qquad 4$$

We can therefore considerably simplify equation 3 for the present experimental situation by inserting the fluid properties for water over the pressure range of interest (760 torr. to 150 torr.) and performing a log-log plot of:

$$\left(q_{ls}/q_l - 1\right).\Delta T_s^{-1} \text{ against } p$$

Such a plot gives us $f(p) = 3.59.\ p^{-0.638}$

The much simplified form of the Zuber equation, equation 3, therefore becomes

$$q_{l.s}/q_l = 1 + \frac{3.59.\Delta T_s}{p^{0.638}} \qquad 5$$

with p expressed in torr
and ΔT_s expressed in ^oC

Equation 5 is similar in form to equation 1 as developed by Ponter et al (6).

Equations 2, 3 or 5 apply to large flat plate heaters. Recently Sun et al (9) extended the 'Zuber' model to horizontal cylindrical heaters under saturated pool boiling conditions. The resulting equation (which depended on the experimental determination of the heater vapour blanket thickness) gave the saturated critical heat flux in terms of the Zuber flat plate value and the heater dimensionless radius (R^1) as follows:

$$q_d/q_l = 0.89 + 2.27 \exp\left(-3.44\sqrt{R^1}\right) \qquad 6$$

Equation 6 is applicable for values of R^1 greater than 0.15.

Ouwerkerk (13) recently proposed a critical heat flux model based on the instability of dry patches which were ob-

served to occur on a heated surface before the critical heat flux was attained. He observed that these dry areas formed and collapsed on the heater surface until at the critical heat flux condition one such dry area suddenly grew to cover the entire heating surface. This different 'dry patch' behaviour was explained by considering the conduction of heat along the heater. Ouwerkerk (13) showed that for such a dry patch to be in equilibrium on a heater wire at a given heat flux then it must have a critical length of $2.S_f^*$. The critical heat flux, q, and the critical length, $2.S_f^*$, were shown to be related by

$$\frac{h_f^{\frac{1}{2}}\,(T_c - T_o - q/h_f)}{h_n^{\frac{1}{2}}\,(T_c - T_o - q/h_n)} = -\left[\tanh\left\{\left(\frac{2.h_f}{K_s.R}\right)^{\frac{1}{2}}.S_f^*\right\}\right]^{-1} \qquad 7$$

It was pointed out that this equilibrium was unstable - a dry region larger than $2.S_f^*$ would grow, a smaller region would disappear. Reference to 7 shows that the critical heat flux is a function of the heater wire radius, R, and the heater wire thermal conductivity, K_s. If the original differential equations presented by (13) are solved for the case of a tubular heater then the result is the same as equation 7 except that R is replaced by $t.(2 - {}^{t}/R)$ where t is the tube wall thickness and R the tube outside radius. It is therefore seen that for a set of tubes of differing wall thickness, but all of the same outside radius and the same material that the critical heat flux q, will be a function of the tube wall thickness, t, i.e.

$$q = f(t) \qquad 8$$

Thus this critical heat flux model is able to predict the critical heat flux as a function of tube wall thickness for a series of tubes of the same outside radius and material - as was found experimentally by the author and reported in Figs. 12, 14 and 15. The 'Zuber' model does not predict such a dependence.

5.0.0.
DIMENSIONAL ANALYSIS APPLIED TO CRITICAL SITUATION

DIMENSIONAL ANALYSIS APPLIED TO CRITICAL SITUATION

Lienhard et al (20) applied dimensional analysis to the problem of saturated pool boiling from horizontal ribbon heaters. They made the initial assumption that

$$q = f(\rho_f, \rho_g, h_{f.g}, \sigma, L, g, \mu_f) \qquad 9$$

and by applying the Pi theorem they reduced these initial eight variables to four independent dimensionless groups to obtain

$$q/q_1 = f\left(L^1, I, \sqrt{1 + \rho_g/\rho_f}\right) \qquad 10$$

Further Sun et al (9) extended 10 by including the surface bubble contact angle, θ_c, and applied the relationship to cylindrical heaters by changing the characteristic dimension from L, the heater strip width, to R, the cylindrical radius as follows

$$q_d/q_\infty = f\left(R^1, I, \sqrt{1 + \rho_g/\rho_f}, \theta_c\right) \qquad 11$$

The addition of the bubble contact angle θ_c as a possible dimensionless variable is a recognition of the fact that under certain circumstances the critical heat flux may be dependent upon heater surface properties.

Apart from possible heater surface effects on the critical heat flux there is the possibility of heater material effects. For instance Benarth (1) drew attention to the effect of heater tube wall thickness on the critical heat flux. He suggested that the critical heat flux would start to fall below the 'thick' wall heater value when the Biot Modulus ($N_B = \frac{h.t}{K_s}$) fell below a certain value. It is seen that based on this suggestion the critical heat flux would be dependent on the thermal conductivity of the heater material. As noted by Benarth by interpreting the heat transfer coefficient h, as Kg/t_g, then for a given heater material - fluid combination, the Biot Modulus can be interpreted as the ratio of the heater tube wall thickness to the boiling film thickness.

It follows that when the boiling film thickness is small compared with the heater wall thickness (large N_B) then fluctuations in the boiling film thickness will produce only minor fluctuations in the heater conditions (temperature and heat flux output). However when the situation is reversed (small N_B) the fluctuations produced in the heater conditions will be much larger.

As noted earlier Ouwerkerk (13) has proposed a critical heat flux model in which the critical heat flux is dependent upon a Biot Modulus of the following form:

$$\frac{2.h_f}{K_s.R}\ (S_f^*)^2 \qquad 12$$

This is the first model that predicts a critical heat flux dependence upon heater material.

It will therefore be assumed that for horizontally mounted cylindrical type heaters that the ratio of the critical heat flux to that predicted by the 'Zuber' model for large flat plates is at least a function of the following

$$q_{d.s}/q_{l.s} = f\left(R^1,\ I,\ \sqrt{1 + \rho_g/\rho_f},\ \theta_c,\ \frac{h_f(S_f^*)^2}{K_s t(2-t/R)}\right) \qquad 13$$

Referring to equation 13

(a) $\sqrt{1 + \rho_g/\rho_f}$ is negligible for most practical situations since $\rho_f >> \rho_g$.

(b) the induced convection scale parameter, I, which depends on liquid viscosity effects has not been found to be a relevant parameter for small cylindrical type heater assemblies by previous investigators, except perhaps in the saturation boiling region. This parameter will therefore be omitted.

(c) for experiments in which the heater material is unchanged for all heater cylinders tested and in which the heat transfer surface is treated and cleaned in a similar manner for all specimen then material thermal conductivity, K_s, and the contact angle θ_c, can be omitted.

Therefore modifying equation 13 according to (a), (b) and (c) above, which is equivalent to the present experimental situation then it follows that

$$q_{d.s}/q_{l.s} = f(R^1, t) \qquad 14$$

provided that all heater outer radius effects can be absorbed in R^1. Equation 14 forms the basis of the correlating schemes used later (see section 7).

6.0.0.

D E S C R I P T I O N O F E X P E R I M E N T

DESCRIPTION OF EXPERIMENT

6.1.0 Experimental Rig

The critical heat flux rig is shown diagramatically in Fig. 1 and photographically in Fig. 2. It consists of a spherically bottomed glass boiling cell 30 cm. in diameter and 37 cm. high which contains the distilled water (conductivity $< 2.5\ \mu$.mho), the heater specimen, aluminium conductors, aluminium cooling and condenser coils, a stirrer, a separate stainless steel heater coil, and stainless steel sheathed, MO_2 insulated, Ch.-Al. thermocouples. All these items were mounted (Figs. 3 and 4) via a stainless steel, teflon lined, tufnol top which formed the vacuum seal to the boiling cell. There were also connections to the vacuum system pumping unit and a Mercury manometer.

The electrical power supply to the specimen was obtained from an autotransformer-rectifier set which was capable of delivering up to 2000 amp. D.C. at 12 volts. The power variation was continuous, was controlled remotely at the experiment and could be tripped by a hand operated trip switch mounted at the experiment. To determine the power dissipated in the specimen the current and specimen voltage drop were measured, using a variable scale dual channel pen recorder. To determine the specimen current, the voltage drop across an accurately calibrated shunt was used to drive one channel of the pen recorder. The specimen voltage drop was taken from tappings at either end of the specimen and recorded on the second channel of the pen recorder. The ability to change scales on the pen recorders allowed heater specimen of largely differing cross sections to be easily accommodated.

Vacuum was produced in the boiling cell by means of two water jet pumps working in parallel and driven by a centrifugal pump. This system eliminated the possibility of contaminants entering the boiling cell from the vacuum system. Rig vacuum was measured by Mercury manometer inconjunction with a Barometer.

The pool temperature was determined by two Ch.-Al. thermo-

couples (using an ice point cold junction) mounted 2 cm, above the specimen and 7.5 cm to each side of the specimen. The outputs from these thermocouples were taken through a rotary switch to a digital voltmeter capable of resolving signals down to one microvolt.

The electrical supply to the separate one kilowatt stainless steel water heater was taken from the normal 230 volt A.C. supply via an autotransformer that reduced the voltage to 120 volts.

6.2.0 Heater Specimen

The heater specimen were made of stainless steel and were either tubes or solid rods. The complete range of sizes used is given in Fig. 5.

Two different types of heater specimen end connections were used in this series of tests. In the first method (Fig. 6 - Method A, Fig. 7) the stainless steel specimen was brazed via brass couplings into stainless steel end pieces to which the voltage tappings were attached. The brass couplings were designed so that reduced heating occurred over 6.35 m.m. of the specimen at each end (Fig. 8). This prevented premature 'burn-out' occuring close to the specimen ends due to modified flow pattern effects. Specimen working lengths were generally in the region of 12.5 cm. although shorter lengths were occasionally used.

The second type of heater specimen end connection used (Fig. 6 - Method B, Fig. 9) which was only applicable to low power solid specimen was to tightly clamp the specimen at each end between aluminium clamping plates. Provided special care was taken over the clamping procedure, end effects were eliminated, and thus 'burn-out' positions were random along the specimen length. Voltage taps were taken either from the clamping nut nearest to the specimen or from aluminium wire clamped between the clamping plates.

In all cases the error in the voltage measurements, caused by not having the voltage taps exactly at each end of the spec-

imen, was determined by separate heater calibration tests. In these tests a monitored current was passed through the specimen and voltage drop measurements made, using a digital voltmeter, across the voltage tappings and then across the specimen working length. From these readings the voltage difference was determined and was never found to be greater than 4% and in the majority of cases it was less than 1.5%. Correction factors were applied to all measurements on this basis.

The heat transfer area was then calculated for the specimen and combined with the voltage correction factor to enable the critical heat flux to be determined directly from the current and voltage measurements made during actual testing.

6.3.0 Boiling Cell Assembly

Before the heater specimen was bolted across the rig input conductors it was rubbed clean in a random manner with a fine emery cloth and then thoroughly washed in acetone. The wettability of the heater surface was tested by running water from a tap along its surface. With experience it was possible, by this technique, to confirm that the heater surface was completely wettable. The heater was then rinsed in acetone, dried and assembled between the rig electrical conductors.

The glass vessel was filled with distilled water, whose conductivity was normally less than 1.5 μmho and never greater than 2.5 μmho and the specimen assembly lowered into position. Electrical power, cooling water supply, vacuum, thermocouple and instrument connections were then made to complete the assembly. For saturated boiling critical heat flux runs under vacuum the water level was approximately 7.6 cm. above the specimen. For subcooled boiling critical heat flux runs the water level was approximately 19 cm. above the specimen.

6.4.0 Experimental Technique

Initially the specimen, and the rig services were checked out by boiling the specimen for approximately five minutes. The thermocouples were checked for consistency by comparing their readings - these were always identical. At intervals during the research programme the current shunts were checked for accuracy and were always found to be correct. Rig instrumentation was regularly checked for accuracy.

A typical test run for saturated boiling conditions under vacuum will now be described. The pool water temperature was raised initially to boiling point at atmospheric pressure and some check critical heat flux values obtained at atmospheric pressure. The water was then cooled to the required temperature and power applied to the specimen until it was boiling with a heat flux of approximately 80% of its anticipated critical value. The vacuum system was then brought onto line and the system brought to saturation conditions. This vacuum was noted and the pool water temperature indicated on the digital voltmeter was checked against the pool saturation temperature corresponding to the operating pressure. The difference between these temperatures was always very small. The power to the specimen was then increased in small steps until finally the critical condition was attained, indicated by the specimen becoming red hot locally. At this point, the system vacuum was noted, the power supply tripped to prevent specimen destruction and the pool temperature recorded. Specimen current and voltage drop values were noted from their respective channel of the dual channel pen recorder. Normally the specimen was undamaged apart from a local discolouration (Fig. 10). Subsequent excursions into the film boiling region still occurred at different random positions on the heater surface. The pool water was then further cooled and the above procedure repeated until the range of the vacuum system was covered. Check points were then obtained with the pool temperature increasing and then again with the pool temperature decreasing.

For subcooled critical heat flux determination under

vacuum, the required system vacuum was preset by means of an adjustable leak into the vacuum exit line, and the pool temperature adjusted to the required value by the heater/cooler system. The power to the heater was then set at approximately 80% of the anticipated critical value and the system allowed to reach steady conditions. Before increasing the power level in step increments the pool was agitated to bring the whole pool to a uniform temperature. The heater power level was then increased in small increments until the critical condition was attained, indicated by the heater glowing red hot locally. At this point the system vacuum was noted, the power supply tripped and the pool temperature noted. The heater current and voltage drop were taken off the dual channel pen recorder. Runs at atmospheric pressure were as described above except, of course, that the vacuum system was not used. Most experimental runs were made starting with a low pool temperature and ending at approximately 100°C apart from check points taken while the pool was being recooled.

For the specimen tested under vacuum, as well as at atmospheric pressure, runs were made at system pressures of 150 torr. and 350 torr. These system pressures corresponded to pressures at the specimen level of 165 torr. and 365 torr. When heater specimen were such that they required large electrical power, water was passed through the cooling coils to hold down the consequential rise in pool temperature.

Many of the test results reported have been repeated with recleaned specimen and new water charges. When a specimen was irreparably damaged and a replacement made the previous results were always reproducible. However this repeatability was only attained after tightly controlling the cleaness of the specimen and the boiling system together with the distilled water quality. The distilled water quality was maintained by replacing the vessel water after each specimen had been completely tested. Normally the conductivity of the distilled water used was less than 1.5 μ.mho.

7.0.0.

C O R R E L A T I O N S C H E M E

CORRELATION SCHEME

Kutateladze et al (10) correlated all their saturated and subcooled critical heat flux results for atmospheric and higher pressures, for the range of R^1 covered approximately by the present set of experiments by using a relationship (see Fig. 19) of the following form

$$q_{d.s}/q_{l.s} = f_1(R^1) \qquad 15$$

Both $q_{d.s}$ and $q_{l.s}$ are to be taken at the same pool subcooling.

Sun et al (9) correlated their saturated only critical heat flux results for a similar range ($0.15 \leq R^1$) to about $\pm$ 20% by a less general but similar relationship (see Fig. 19).

$$q_d/q_l = f_2(R^1) \qquad 16$$

They determined $f_2(R^1)$ by a semitheoretical approach as

$$f_2(R^1) = 0.89 + 2.27 \exp(-3.44\sqrt{R^1}) = A \qquad 17$$

Now equation 15 is much more general than equation 16 in that it contains all the subcooled results as well as the saturated boiling results. It is therefore of interest to express the graphical correlation of (10) over the range of R^1 of interest in a mathematical form equivalent to 17. A good fit to the results of (10) over an approximately equivalent range of R^1 is given by

$$f_1(R^1) = 1.0 + 2.27 \exp(-3.44\sqrt{R^1}) \qquad 18$$

Implied in this relationship is that the critical heat flux for large surfaces ($q_{*\infty}$ of (10)) is the same as $q_{l.s}$, the 'Zuber' critical heat flux for large flat surfaces. That this is so tends to be substantiated by the water results quoted in Fig. 2 of (10).

Now returning to equation 14 and applying it to solid cylindrical heaters and 'thick' walled tubular heaters only, so that the dependence on wall thickness 't' vanishes then

$$q_{d.s}/q_{l.s} = f(R^1) \qquad 19$$

Equation 19 is the same form as used by Kutateladze et al (10) i.e. equation 15.

From equation 5

$$q_{l.s} = q_l (1 + 3.59.Z) \quad 20$$

where $Z = \Delta T_s.p^{-0.638}$ 21

∴ combining 19 and 20 and rearranging

$$q_{d.s}/q_l.f(R^1) = 1 + 3.59.Z \quad 22$$

The author found that the vast majority of the present experimental results could be correlated by taking

$$f(R^1) = 1.123.A \quad 23$$

Defining $q_l^1 = q_l . 1.123.A$ 24

Now combining 22, 23 and 24 then

$$q_{d.s}/q_l^1 = 1 + 3.59.Z \quad 25$$

Equation 25 is shown drawn through the present experimental results (thin walled and 'thick' walled heaters) on Fig. 17. It is seen that the vast majority of these results are predicted by equation 25 to within ± 20%.

Equation 19 can be further simplified when the heater cylindrical radius is such that $R^1 > 1.0$ approximately. For this situation the heater can be considered equivalent to a 'large' surface to which the 'Zuber' model should apply.

∴ equation 19 becomes

$$q_{\infty.s}/q_{l.s} = Const = 1.0 \quad 26$$

if Zuber model applies

∴ combining 20 and 26 then

$$q_{\infty.s}/q_l = 1 + 3.59.Z \quad 27$$

Equation 27 is shown drawn through the present 'large' surface heater results (thin walled and 'thick' walled heaters) on Fig. 16.

For a set of tubular heaters with the same outside diameter ($R^1 \sim$ constant) but differing wall thickness then

equation 14 reduces to

$$q_{d.s}/_{q_{l.s}} = f(t) \qquad 28$$

When $R^1 \geq 1.0$, that is, the heater constitutes a large surface, and for saturation boiling conditions when the deviation from the solid cylinder results was found to be most significant then equation 28 reduces to

$$q_{\infty}/_{q_l} = f(t) \qquad 29$$

Fig. 14 shows the present experimental results plotted as 'q_{∞}' against 't' for constant heater radius ($R^1 \sim$ constant and $R^1 > 1.0$) together with the results of Ponter et al (6). Fig. 15 shows the results of Fig. 14 plotted in the form '$q_{\infty}/_{q_l}$' against 't'.

8.0.0.

RESULTS AND COMMENTS

RESULTS AND COMMENTS

8.1.0. General

Because a large number of graphs would be needed to present all the raw data used the author has elected to present data in tabular form - Fig. 5.

Fig. 11 shows a typical set of critical heat flux results for one heater specimen (6.35 m.m. O.D. by 0.56 m.m. wall thickness) over the complete vacuum range for saturated and subcooled pool conditions. The saturated boiling results were obtained with a specimen immersion of approximately 7.6 cm and the subcooled results with a specimen immersion of approximately 19 cm. Generally saturated boiling results have been obtained for a range of specimen (Fig. 5) over a system pressure range of atmospheric to approximately 150 torr. Subcooled results have been obtained over a maximum subcooled range of 60°C (at atmospheric pressure) and for system pressures of atmospheric, 350 torr. and 150 torr. Not all specimen were tested under vacuum conditions.

8.2.0. Saturated Boiling Conditions

Fig. 12 shows the critical heat flux results obtained under saturated boiling conditions for a pressure range of atmospheric to 150 torr. for 'large' surface heaters ($R^1 > 1.0$) all with an outside diameter of 6.35 m.m. These heaters consisted of a solid rod, and three tubes each with a different wall thickness. As the outside diameter of all these heaters was constant, and only the wall thickness varied it follows that the wall thickness has an effect upon the saturated critical heat flux and that this effect extends into the low pressure region.

Fig. 13 shows the critical heat flux results obtained under saturated boiling conditions for a pressure range of atmospheric to 150 torr. for 'smaller' surface heaters ($R^1 < 1.0$). It is seen that the critical heat flux varies with heater diameter and that this effect also extends into the low pressure region.

Fig. 14 presents, for three pressures, atmospheric, 365 torr. and 165 torr. the results presented in Fig. 12 cross

plotted to show how the critical heat flux varies with heater wall thickness. Also shown are the critical heat flux values predicted by the 'Zuber' model (equation 2) together with the experimental results of Ponter et al (6) for a stainless steel tubular heater 5.85 m.m. O.D. by 0.38 m.m. wall thickness operating under similar experimental conditions.

Fig. 15 attempts to consolidate the three independent curves plotted on Fig. 14 into a single curve by plotting the critical heat flux ratio q_{∞}/q_1 against the heater tube wall thickness 't'. Also shown on this curve are the experimental results due to Ponter et al (6). The equation of the mean line drawn through the points, which has the same form as that given in equation 29, is

$$q_{\infty}/q_1 = 1.36 - 0.55 \exp(-1.42.t) \qquad 30$$

t is in millimetres

8.3.0 Subcooled Boiling Conditions

8.3.1 $R^1 > 1.0$

Fig. 16 is a plot of the mean experimental saturated and subcooled critical heat flux results, under atmospheric and vacuum conditions, for 'large' surface heaters ($R^1 > 1.0$) against the 'Zuber' parameter 'Z'. Both thin walled and thick walled heater results are included. The form of the plot is $q_{\infty.s}/q_1$ against Z and drawn through the points is equation 27 which is the critical heat flux equation (due to Zuber) applicable to large flat surfaces. Only a selection of values are plotted, not to overload the diagram, however, the author has included the values that diverge furthest from the line defined by equation 27. It is seen that the agreement with equation 27 is quite good except in the saturated boiling region where the maximum divergence is 50% for a solid specimen boiling at a pressure of 165 torr.

8.3.2 $0.13 < R^1 < 1.3$

Fig. 17 is a plot of the mean experimental critical heat flux results for saturated boiling conditions and for 10°C

increments of subcooling (i.e. all the results tabulated in Fig. 18). Values which were co-incident with previously plotted values were omitted.

This graph contains essentially results from the whole range of variables tested as follows:

(1) $0.13 < R^1 < 1.3$

(2) Heater tube wall thickness variation

(3) System pressure variation

(4) Variation of the pool subcooling

Drawn through the points is the full line defined by equation 25, that is

$$q_{d.s}/q_l = 1 + 3.59.Z$$

The dotted lines give the ± 20% range about equation 25. It is seen that the vast majority of the points are contained within this ± 20% band.

8.4.0 Graphical Comparison

A graphical comparison of the authors final correlation as contained in Fig. 17 is given in Fig. 19 with the correlations due to Kutateladze et al (10) and Sun et al (9).

This comparison is made as a plot of $q_{d.s}/q_{l.s}$ against R^1 which is the form given in equation 19 and is the form adopted by both Kutateladze et al, and Sun et al in presenting their final correlations.

Kutateladze et al experimented with stainless steel cylindrical heaters and varied (1) the heater diameter, (2) the working fluid (3) the pool subcooling and (4) the working pressure - above atmospheric pressure.

Sun et al experimented with Nichrome cylindrical heaters and varied (1) the heater diameter (2) the working fluid (3) the system gravity (4) the system pressure. However all these critical heat flux values were obtained for saturated pool boiling conditions only.

In the present series of tests stainless steel cylindrical heaters were used (both solid and tubular). The variables were (1) the heater diameter (2) the heater wall thickness (3)

the pool subcooling (4) the system pressure - below atmospheric.

It is worthwhile noting here that the spread about the line due to Riley and about that due to Sun et al is $\pm$ 20%. The estimated spread about the line due to Kutateladze et al is no more than $\pm$ 15%.

9.0.0.

D I S C U S S I O N

DISCUSSION

Previous comparable work under vacuum to that reported was carried out by Ponter et al (6), but they used only one specimen size ($R^1 > 1.0$). Comparison of Fig. 11 of this thesis with Fig. 10 of (6) shows the general similarity of results, however it is worthwhile noting that the heater dimensions are slightly different in the two cases. A comparison of the saturated critical heat flux values due to Ponter et al (6) with the present results is given in Figs. 14 and 15. The agreement is seen to be good. In the subcooled range the agreement is not so good at the first examination, the authors 'large' surface ($R^1 > 1.0$) results, Fig. 16, substantiating the Zuber model (equation 3 or alternatively equation 5) while (6) quote their results (equation 1 of this thesis) as being up to 20% below the Zuber predictions at 100 torr. pressure. Now the present results were correlated using the vacuum that existed at the level of the heater, that is allowing for the positive pressure head due to water depth. It is not clear in (6) whether their results are correlated using the 'system' pressure or using the pressure at the specimen depth of immersion. This pressure difference would be significant and equivalent to either 45 torr. or 29 torr. depending on whether the water depth of 61 cm quoted in their paper is a specimen depth of immersion or a total water depth. This is a possible explanation that could explain some of the difference in the two sets of results. Another possible reason is that the present author did not take the same extensive precautions over degassing the water charge before testing. However during a complete specimen test the check points taken near completion of testing when no gas bubbles were visible always repeated the early test results when small gas bubbles were in evidence. Unfortunately there are no other sets of subcooled results under vacuum against which the present results and those due to Ponter et al (6) can be compared.

The authors results for 'large' heater surfaces (defined by $R^1 > 1.0$, (10)) are presented for saturated conditions in Fig. 12 and for subcooled and saturated conditions in Fig. 16.

As all the results presented in Fig. 12 are for the same heater outside diameter then it is seen that the tube wall thickness affects the saturated critical heat flux and that this effect extends into the vacuum region. Benarth (1) refers to this effect under atmospheric conditions. Fig. 14 is a cross plot of the results presented in Fig. 12 and shows directly the saturated critical heat flux dependence on the heater wall thickness. Shown also are the results of Ponter et al (6) and the calculated values using the Zuber analysis (equation 2). The results given in Fig. 14 have been further rationalised and are represented in Fig. 15 by a single curve. This has been achieved by plotting the actual saturated critical heat flux relative to its corresponding 'Zuber' predicted value, against the heater wall thickness - the results, including those due to Ponter et al (6), then correlate reasonably well. The equation of the correlating line is given on Fig. 15 and this line correlates the results to about $\pm$ 15%. It therefore appears that to predict critical heat fluxes in the saturated region accurately the effect of the heater wall thickness should be considered. In this region with $R^1 > 1.0$ with water as the working fluid and with normal gravity, solid rod heaters give saturated critical heat fluxes that are approximately 40% larger than those predicted by Zuber theory. Tubular heaters with a wall thickness of approximately 0.3 m.m. have a critical heat flux value that is very similar to the Zuber predicted value. The previous remarks apply, of course, to stainless steel heaters. Although this tube wall effect is still present in the subcooled region (see Fig. 16, $Z > 0.3$) its effect is much smaller. Until the recent paper due to Van Ouwerkerk (13) no critical heat flux theory, to the authors knowledge, included or considered the effects of heat conduction within the heater material and thus by implication a tube wall thickness effect. As already mentioned Benarth had however introduced the Biot modulus as a possible means of allowing for this effect of material and heater wall thickness.

For smaller surfaces ($R^1 < 1.0$) and for saturated pool conditions, Fig. 13 shows the authors results obtained for

heater operation under vacuum. The further results obtained in this range but for heater operation at atmospheric pressure only are tabulated in Fig. 5. Reference to Fig. 13 indicates that in this range the saturated critical heat flux is dependent on the outside diameter of the heater (comparison of solid cylindrical heater results, Fig. 13) and that this effect extends into the vacuum region.

Finally the author has correlated his results (Fig. 17) over the whole range of parameter variation by plotting with the ordinates given by equation 25. Equation 25 is drawn on Fig. 17 as the full line and it is seen that it represents a good average line with the vast majority of the points plotted contained within a $\pm$ 20% band about the line of equation 25. To avoid overloading this figure only mean critical heat flux values (all tabulated on Fig. 18) have been plotted for saturated conditions and for $10^{o}C$ increments of subcooling at pressures (at the specimen level) of 760 torr., 365 torr., and 165 torr. The only significant exceptions to the correlation are in the saturated boiling region and there are only a few such values. The parameter ranges contained within this correlation are; stainless steel horizontal tubular and solid rod heaters ($0.13 < R^{1} < 1.3$ and 0.25 m.m. $< t <$ 3.18 m.m.), saturated and subcooled pool conditions (subcooling up to $60^{o}C$ at atmospheric pressure), and a pressure range of 760 torr. down to a vacuum of 160 torr.

Now Fig. 19 enables a comparison to be made of the mean lines due to Kutateladze et al (10), Sun et al (9) and the present author. It is seen that the general shapes of the lines are similar and that they lie fairly close together with the line due to (9) for saturated pool conditions only being below those due to (10) and to the present author whose lines apply to both saturated and subcooled pool conditions. The curve due to (10) divides at about R^{1} of 0.28 according to the value of Z^{1}. The curve due to (9) correlates results to $R^{1} \sim 0.15$ and that due to the present author to $R^{1} \sim 0.13$. However for the ranges covered by (9) and by the present author it would be difficult to detect the split obtained by (10) at

$R^1 \sim 0.28$. It is worthwhile noting here that the spread about the curve of Sun et al (9) and about the curve due to the present author is $\pm$ 20%, and that about the curve due to Kutateladze et al (10) about $\pm$ 15%. All the mean lines are therefore contained within the experimental spread of any of the other mean lines.

The authors results therefore tend to confirm the correlations due to (9,10) and to show that they apply to operation within the vacuum region (down to 165 torr.) as well.

It should be noted that the variation in the saturated critical heat flux with heater diameter indicated by the solid rod heater results shown on FIG 13 is in apparent contradication to the trend indicated by the final correlation given graphically on FIG 19. This result probably occurs because the 0.71 m.m. O.Dia. heater is at the lower extremity of the range investigated. In this region Kutateladze et al (10) found their results for saturated boiling conditions following just such a trend (see Fig 19). It is therefore probable that this is the effect that has been observed and recorded by the author on FIG 13.

Measurement of the wall thickness of samples of the 3.18 m.m. O.Dia. tubes used in the test series to investigate the heater tube wall thickness effect on the critical heat flux indicates a maximum variation from average of 6% and this occurs with the smallest tube wall thickness employed. This result implies a maximum error in this test series of 6% due to variation of the electrical resistance caused by this wall thickness variation. In reality such resistance variations would cause temperature variations within the heater which would tend to reduce any heat flux variations caused by such resistance variation effects. Thus in reality this maximum variation in the critical heat flux from the measured average value, due to this effect, will be less than 6%.

10.0.0.

C O N C L U S I O N S

CONCLUSIONS

1. Experimental critical heat flux results have been obtained at atmospheric pressure and under vacuum conditons for saturated and subcooled pool boiling of water using stainless steel tubular and solid rod heaters in horizontal placement.

2. It has been shown Figs. 12, 14 and 15 that the heater wall thickness has an effect on the saturated critical heat flux at atmospheric pressure and under vacuum conditions. This effect has been correlated reasonably well for the present results ($R^1 > 1.0$ - large surfaces) including the results of Ponter et al (6) and the result is shown on Fig. 15.

3. Reference to Fig. 16 indicates, for large heater surfaces ($R^1 > 1.0$) that the critical heat flux for values of $Z > 0.3$ is well predicted by the Zuber analysis (equation 3 or 5) for both the solid and tubular heaters working under atmospheric and vacuum conditions.

4. All the present results, (with the exception of a few values in the saturation boiling region), for solid rod and tubular heaters under atmospheric and vacuum conditions and for pool subcoolings up to 60°C are correlated to within about ± 20% (see Fig. 17) by the following relationship:

$$\frac{q_{d.s}}{q_{l.s}} = 1.123 \cdot \left[0.89 + 2.27 . \exp(-3.44 \sqrt{R^1}) \right]$$

$q_{l.s}$ represents the 'Zuber' critical heat flux corresponding to the pool subcooling for which $q_{d.s}$ is being evaluated. The range of R^1 is $0.13 < R^1 < 1.3$.

5. Reference to Fig. 19 shows that the present correlating equation quoted above, which includes results obtained under vacuum, agrees fairly well, over similar ranges of R^1, with the results of Kutateladze et al (10) and Sun et al (9).

11.0.0.

A P P E N D I X

HEATER SURFACE WETTABILITY EFFECTS

11.1.0 Introduction

During the commissioning period of the critical heat flux rig previously described one of the troubles experienced was that of the stainless steel heater surface becoming contaminated during operation and the system producing reduced values for the critical heat flux. This problem was finally overcome by producing the very clean and tightly controlled experimental conditions previously described and by using double distilled water that was replaced at the start of testing of each new heater specimen. Reference to the literature indicates that other experimenters in this field have faced similar problems for instance from Sun et al (9) "for different runs the wires and liquid were replaced by new ones to avoid effects of contamination of the liquid or carbon deposits on the wire surface". It is reasonable to say therefore that the majority of the critical heat flux results reported in the literature and compared with critical heat flux theories such as that due to Zuber (19) have been obtained from extremely clean and tightly controlled systems.

11.2.0 Investigation and Results

For a horizontal stainless steel heater tube (4.83 m.m. O.D. by 0.254 m.m. wall thickness) operating in distilled water at atmospheric pressure and under pool boiling conditions Fig. 20 shows the band of reproducible results, curve 1, for a clean wettable surface. These results compare well with other comparable results published in the literature e.g. Ponter et al (6). However when first subjecting the rig boiling cell to vacuum conditions a contamination agent (unknown) was pulled into the system and contaminated the heater surface. The effect of this unknown contaminant was to produce the reduced critical heat flux characteristic shown as curve 2 on Fig. 20.

A very brief investigation of this effect was then made as follows; An experiment was set up using a horizontal stainless steel tubular heater (4.83 m.m. O.D. by 0.56 m.m. wall thickness) again in distilled water, at atmospheric pressure,

and under pool boiling conditions with the heater surface prepared and thoroughly cleaned. The critical heat flux results obtained were found to lie within the band about curve 3 of Fig. 21 - again these results compare well with comparable results in the literature. The experiment was then repeated, but with the middle half of the heater surface lightly contaminated with Silicone Grease, and the much reduced critical heat fluxes obtained as shown by curve 4 of Fig. 21. All the critical heat flux positions occurred within the heater area that was contaminated with the Silicone Grease. It was also apparent by observation of the originally uncontaminated area of the heater surface that this area was slowly becoming contaminated also. Shown also on curve 4 of Fig. 21 are two results (discovered later) due to Torikai et al (21) which tend to confirm the results presented.

11.3.0 Comments

The previous results tend to indicate that heater surface wettability can be an important factor in determining the magnitude of the critical heat flux under pool boiling conditions. Now the bubble contact angle on the heater surface is a measure of the surface wettability. To the authors knowledge, none of the critical heat flux models (which generally assume that the critical heat flux phenomenon is controlled by hydrodynamic effects that occur some distance away from the heater surface) include this parameter or allow for the effects of wettability. Indeed wettability being partly a surface property is a very difficult parameter to define and handle in a practical sense and its use is to be avoided if possible. Also the published results which are compared with the hydrodynamic theories such as that due to Zuber (19) tend to be obtained in very clean and tightly controlled environments in which the contact angle or wettability should remain reproducibly constant. However there are some interesting results available for liquid Mercury critical heat fluxes under pool boiling conditions with various degrees of addition of the wetting agent Magnesium - see Tong (22). Reference to Fig. 2.16 of (22) shows how the

critical heat flux rises from a very low value (5×10^3 B.Th.U/hr.ft^2) for liquid Mercury alone (none wetting to the heater surface) to a value of approximately 140×10^3 B.Th.U/hr.ft^2 for the addition of 0.05% of the wetting agent, Magnesium.

11.4.0 Conclusions

Self heated heat transfer surfaces that transfer heat to liquids under boiling or possible boiling situations should be kept free of none wetting agents (such as greases).

12.0.0.

R E F E R E N C E S

REFERENCES

1. Benarth L. A theory of local boiling burnout and its application to existing data. Presented at the Third National Heat Transfer Conference A.S.M.E.-A.I.Ch.E. Storr Connecticut August 1959, Preprint 110.

2. Ivey and Morris. Effect of test section parameters on saturation pool boiling burn-out at atmospheric pressure. U.K.A.E.A. Report A.E.E.W.-R176 April 1962.

3. Kutateladze et al. The critical heat flux at the pool boiling of some binary mixtures - Paper no. 96 Third International Heat Transfer Conference, Chicago August 1966.

4. Van Stralen et al. Investigations on the critical heat flux of pure liquids and mixtures under various conditions. Int. J. Heat Mass Transfer, Vol. 12, 1969, pp 1353-1384.

5. Ivey and Morris. Critical heat flux of saturation and subcooled pool boiling in water at atmospheric pressure. Paper 94 Third Int. Heat Transfer Conference, Chicago August 1966.

6. Ponter and Haigh. The boiling crisis in saturated and subcooled pool boiling at reduced pressures. Int. J. Heat Mass Transfer, Vol. 12, 1969, pp 429-437.

7. Cumo et al. Some aspects of free convection boiling heat transfer. Paper no. 104 Third Int. Heat Transfer Conference, Chicago, August 1966.

8. McAdams et al. Heat transfer from single horizontal wires to boiling water. Chem. Eng. Progress 44 no. 8, 639, 1948.

9. Sun et al. The peak pool boiling heat flux on horizontal cylinders. Int. J. Heat Mass Transfer Vol. 13, 1970, pp 1425-1439.

10. Kutateladze et al. Effects of heater size on critical heat loads in the boiling of a liquid with free convection. High Temperature, Vol. 5, Part 5, 1967, pp 747-752.

11. Borishanski. An equation generalising experimental data on the cessation of bubble boiling in a large volume of liquid. Zhurnal Teknicheski Fiziki, Vol. 25, page 252 (1956).

12. Lienhard et al. An induced-convection effect upon the peak boiling heat flux. J. Heat Transfer, 92, 1, 1970.

13. Van Ouwerkerk. Burnout in pool boiling. The stability of boiling mechanisms. Int. J. Heat Mass Transfer, Vol. 15, no. 1, 1972, pp 25-34.

14. Semeria et al. Calefaction spots on a heating wall: temperature distribution and resorption. Sym. on Boiling Heat Transfer in Steam Generating Equipt. and Heat Exchangers, Manchester, 15-16 Sept. 1965 Paper 3.

15. Rohsenow et al. Correlation of maximum heat flux data for boiling of saturated liquids. A.I.Ch.E.-A.S.M.E. Heat Transfer Symposium, Kentucky, U.S.A. March 1955.

16. Deissler. Personal communication described by Cole. A.I. Chem. E. J. 6, Dec. 1960.

17. Zuber. Stability of boiling heat transfer. Trans. A.S.M.E. April 1958.

18. Zuber et al. Further remarks on the stability of boiling heat transfer. U.C.L.A. Report 58-5, Los Angeles Jan. 1958.

19. Zuber et al. The hydrodynamic crisis in pool boiling of saturated and subcooled liquids. Int. Heat Transfer Conference, Colorado, U.S.A., Part II Paper 27, 1961, pp 230-236.

20. Lienhard et al. On correlating the peak and minimum boiling heat fluxes with pressure and heater configuration. J. Heat Transfer 88, 94 (1966).

21. Torikai et al. Photographical study for boiling heat transfer mechanism. Proc. 3rd Int. Heat Transfer Conference, 1966, Illinois, A.I.Ch.E. Paper 105, Vol. III.

22. Tong. Boiling heat transfer and two phase flow. Pub. John Wiley and Sons Inc. Figure 2.16, Page 43.

13.0.0.

PART I - FIGURES

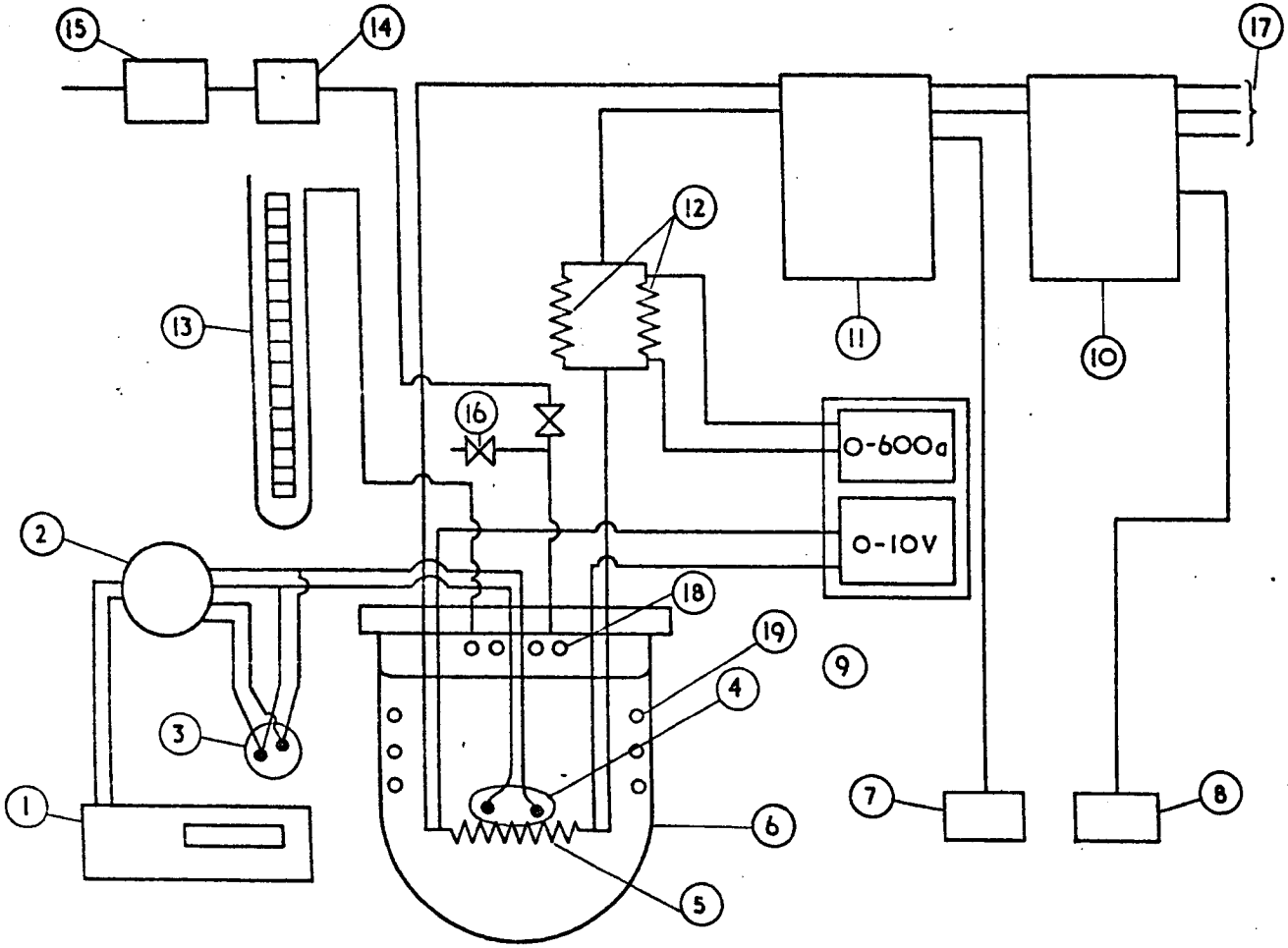

ITEM	Nº
DIGITAL VOLTMETER	1
ROTARY SWITCH	2
THERMOCOUPLE COLD JUNCTIONS	3
THERMOCOUPLE HOT JUNCTIONS	4
HEATER SPECIMEN	5
BOILING CELL	6
TRIP UNIT	7
REMOTE DRIVE UNIT	8
DUAL CHANNEL PEN RECORDER	9
AUTOTRANSFORMER	10
RECTIFIER	11
CALIBRATED SHUNTS	12
MERCURY MANOMETER	13
WATER TRAP	14
JET PUMP VACUUM UNIT	15
CONTROLLABLE AIR LEAK	16
THREE PHASE SUPPLY	17
CONDENSER COIL	18
COOLING COIL	19

FIG I SCHEMATIC LAYOUT OF CRITICAL HEAT FLUX RIG

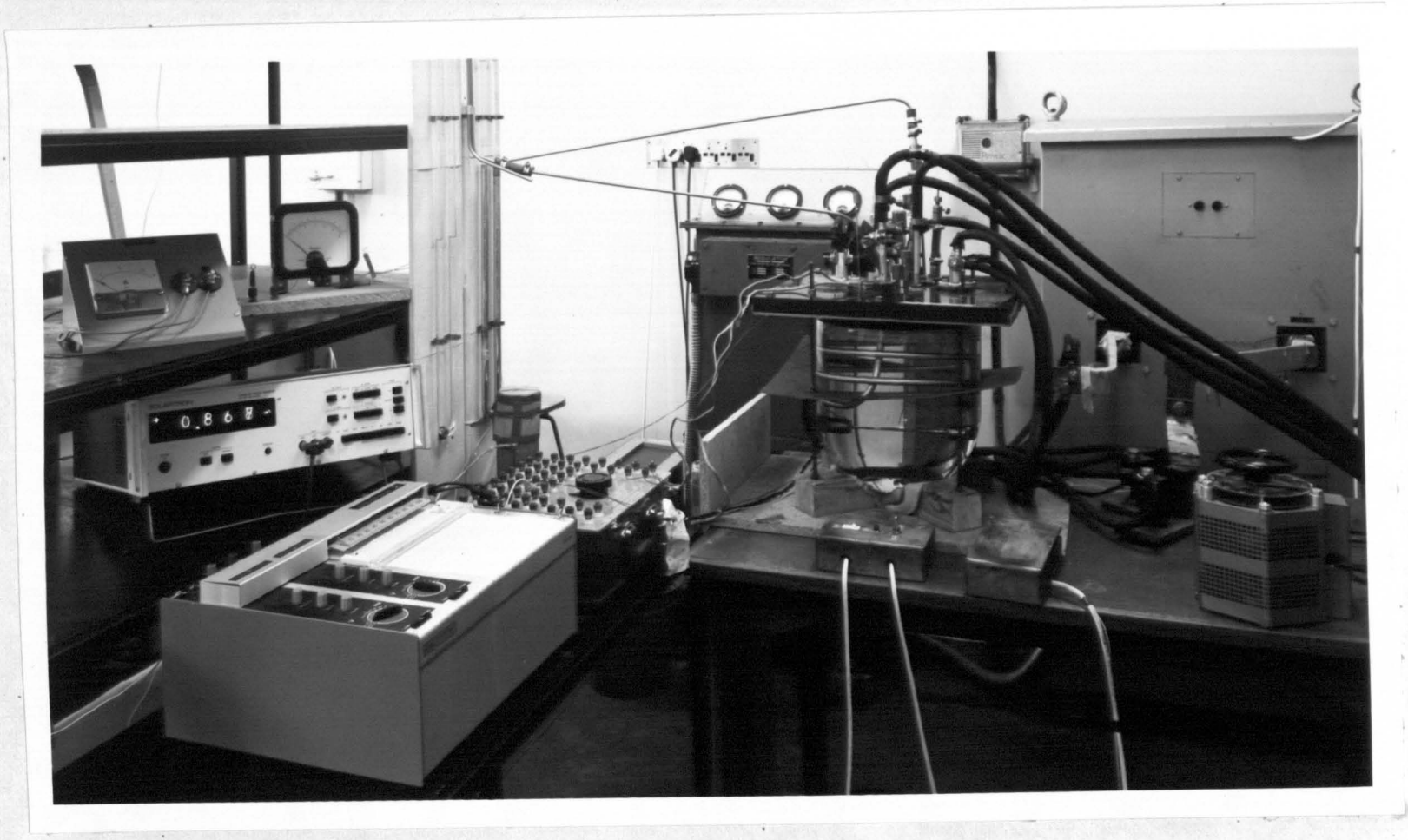

FIG. 2 CRITICAL HEAT FLUX RIG

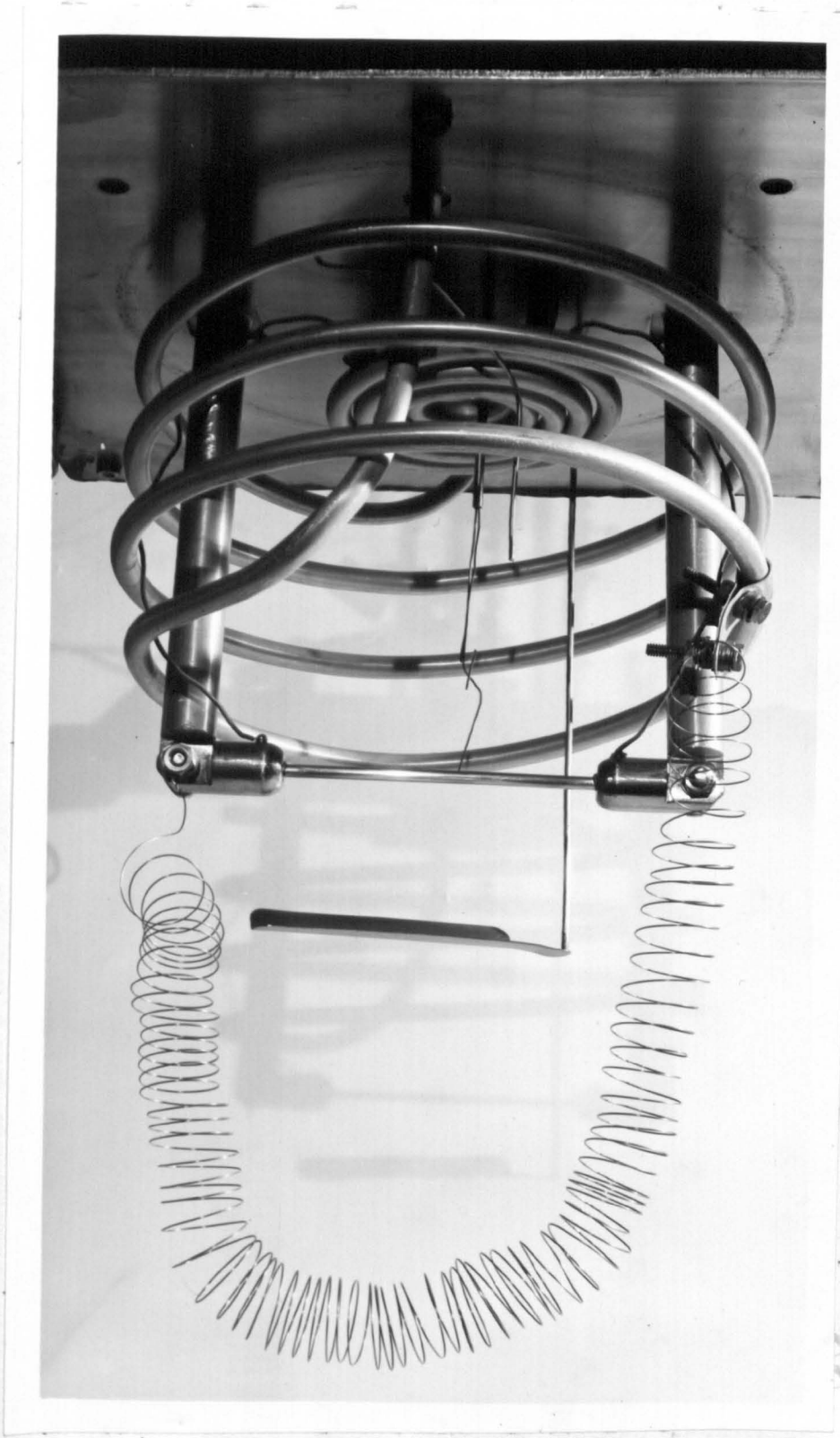

FIG. 3 INNER ASSEMBLY OF BOILING CELL

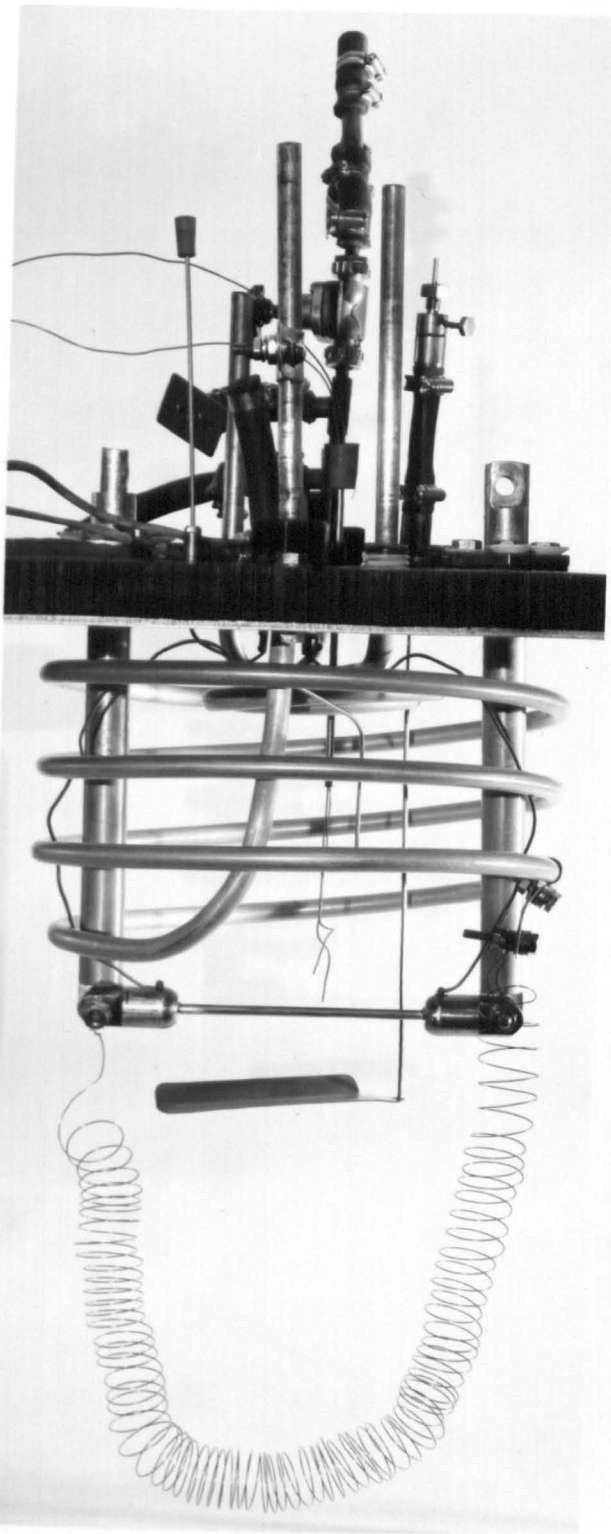

FIG. 4 UPPER SURFACE AND INNER ASSEMBLY OF BOILING CELL

R m.m.	t m.m.	$q_{d.s.}$ watt/cm² at 760 torr. Pool Subcooling °C							$q_{d.s.}$ watt/cm² at 365 torr. Pool Subcooling °C					$q_{d.s.}$ watt/cm² at 165 torr. Pool Subcooling °C				
		0	10	20	30	40	50	60	0	10	20	30	40	0	10	20	30	36
3·18	0·254	103	124	183	242	302			75	126	195	264		61	122	198	272	
	0·457	112	131	190	253	316	379	440		131	204	279	351		131	210	289	
	0·56	117	139	200	263	327	392	453	85	141	216	290	366	69	145	240	303	
	0·915	126	145	207	273	339	404		93	145	214	283	352	79	137	218	299	
	Solid	147	160	214	285	356	427		102	139	223	310	395	87	138	228	319	
2·41	0·254	105	128	183	250													
	0·56	124	143	198	262	330												
	0·788	132	147	201	272	343	414											
	Solid	147	163	226	306	388												
1·58	0·508	120	147	217	320	423												
	0·788	134	156	231	342	455			99	165	275	384	493	88	161	285	406	495
	Solid	143	173	254	360	470	570	670										
1·18	0·381	120	147	229	327	420												
	Solid	155	180	257	362	470	575											
0·812	Solid	171	190	278	403	530			123	204	330	458		105	215	358	500	
0·595	Solid	158	190	292	418	540												
0·457	Solid	150	210	313	420	528												
0·355	Solid	153	220	319	410	502			112					95				

FIG. 5. MEAN EXPERIMENTAL CRITICAL HEAT FLUX RESULTS FOR SATURATION AND 10 °C SUBCOOLING INCREMENTS (Spread about mean ~±10 watt/cm²)

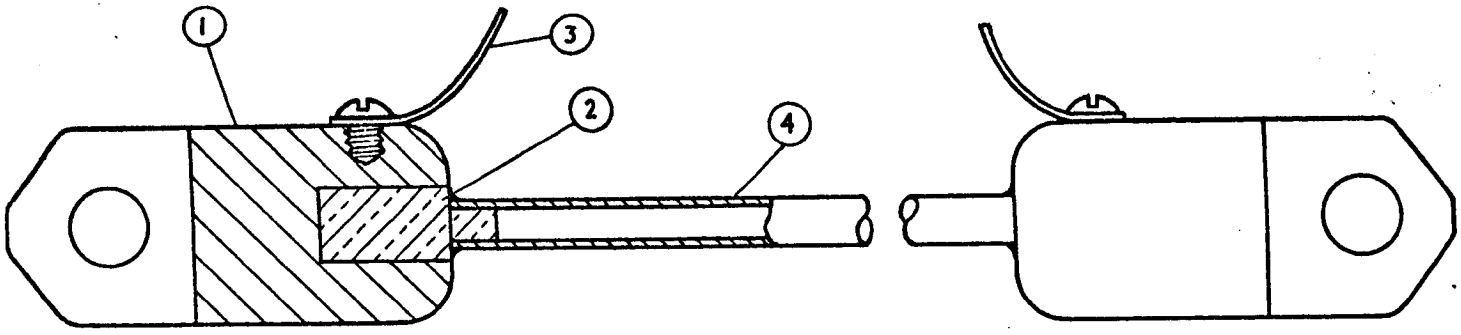

ITEM	№
S/S END PIECE	1
BRASS COUPLING	2
VOLTAGE TAP	3
S/S TUBULAR SPECIMEN	4
BACK CLAMPING PLATE	5
S/S ROD SPECIMEN	6
FRONT CLAMPING PLATE	7
CLAMPING NUTS	8

SPECIMEN ASSEMBLY WITH BRAZED ENDS - LEFT HAND END SHOWN SECTIONED - METHOD 'A'

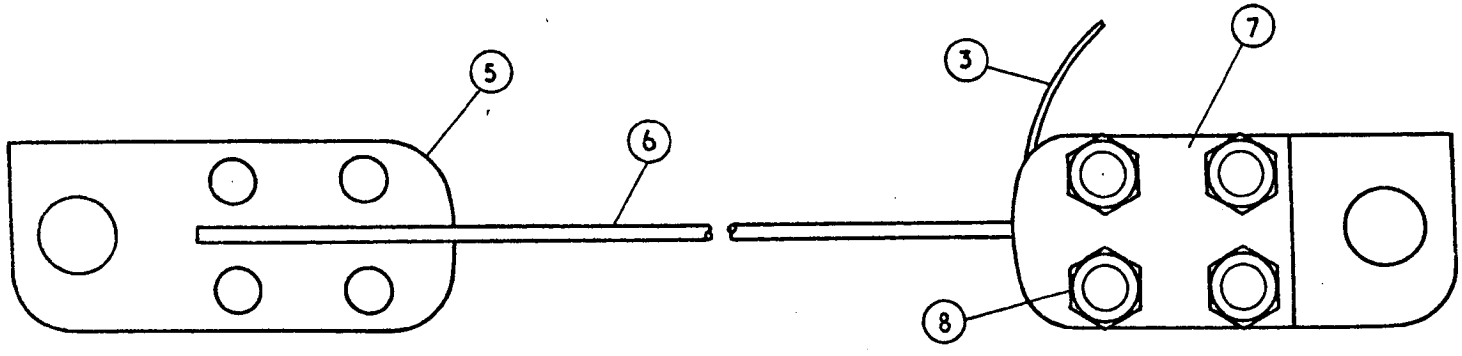

SPECIMEN ASSEMBLY WITH CLAMPED ENDS - FRONT CLAMPING PLATE OMITTED FROM L.H. END - METHOD 'B'

FIG. 6. HEATER SPECIMEN ASSEMBLIES

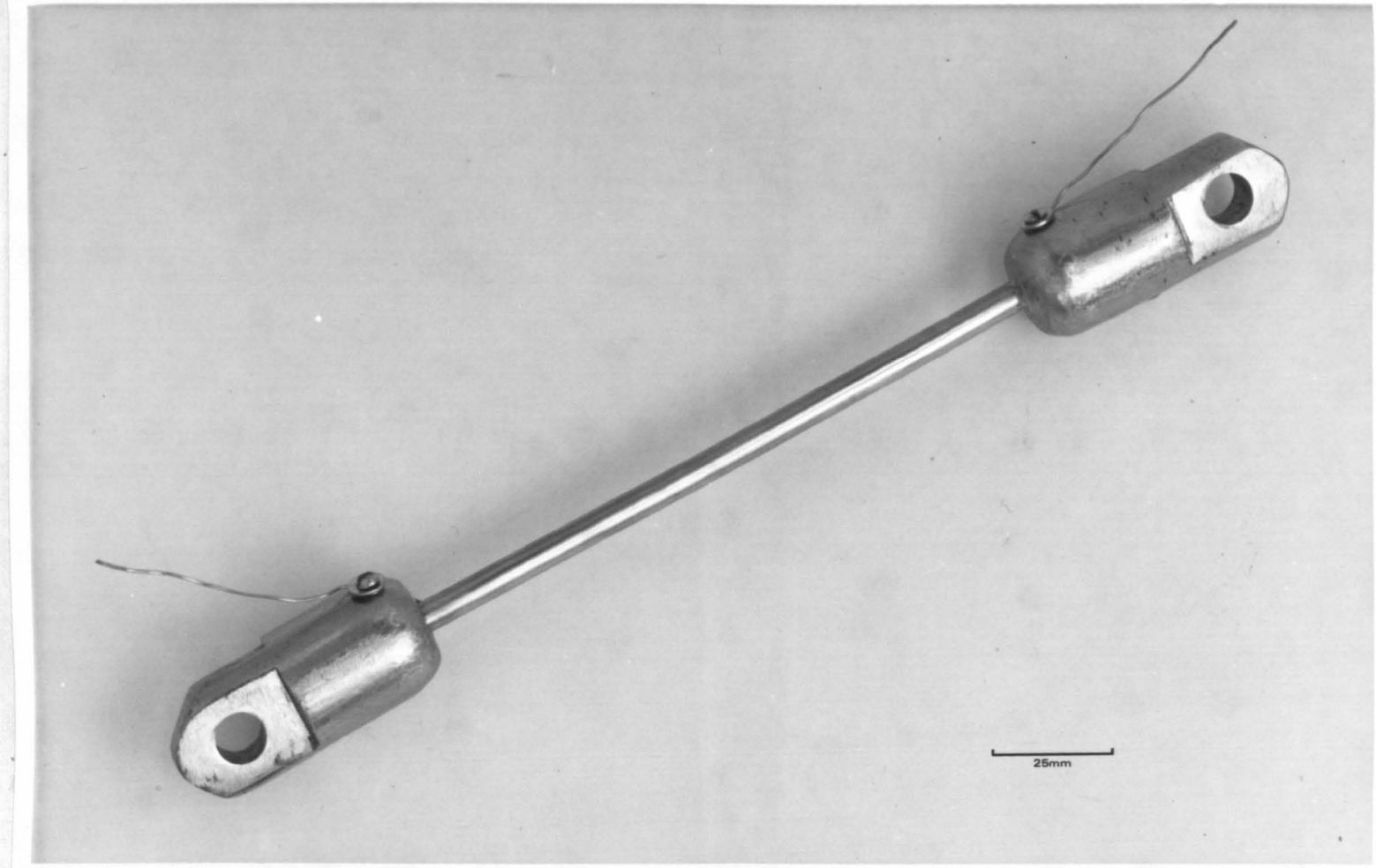

FIG. 7 SPECIMEN ASSEMBLY WITH BRAZED ENDS - METHOD 'A'

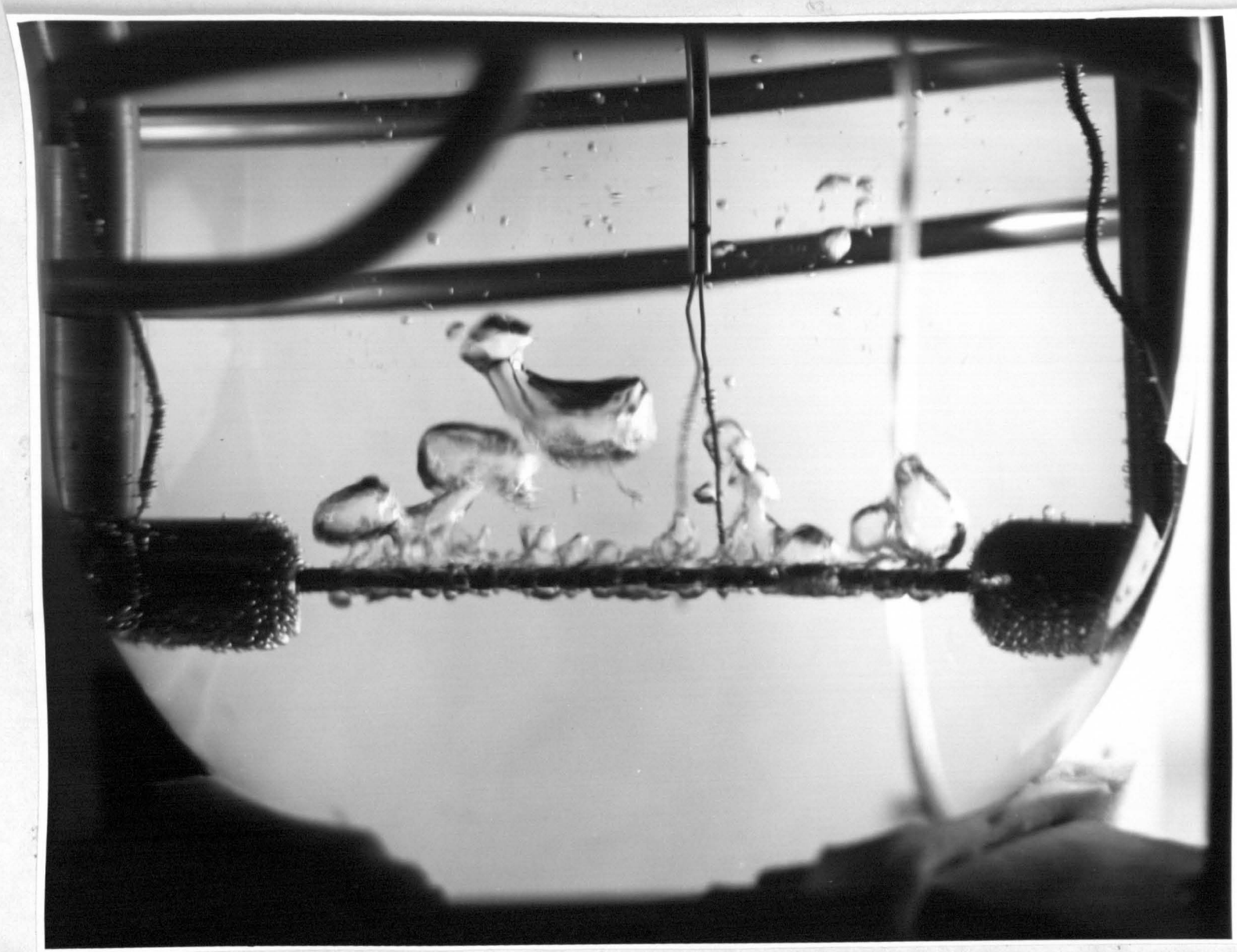

FIG. 8 BOILING FROM SPECIMEN - NOTE BOILING CEASES SHORT OF END PIECES

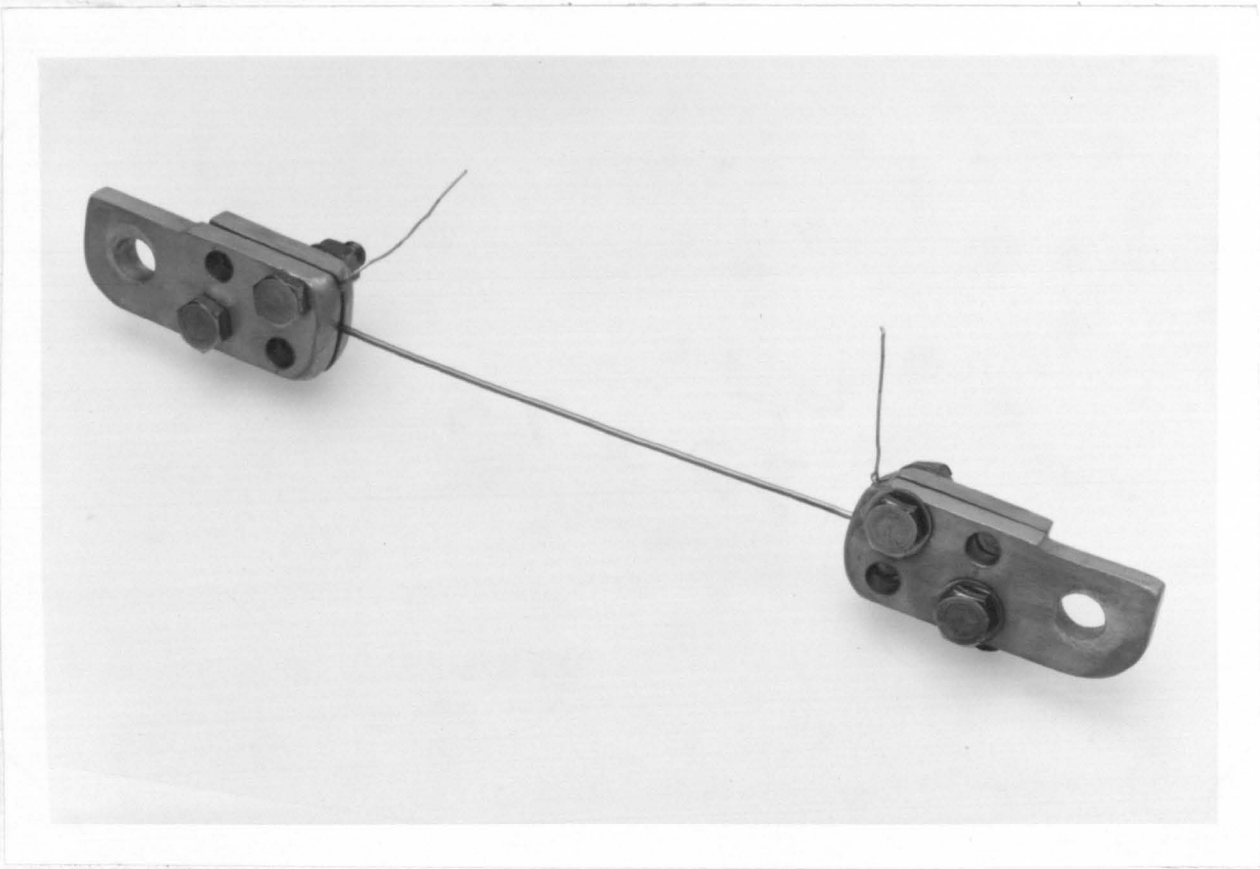

FIG. 9 SPECIMEN ASSEMBLY WITH CLAMPED ENDS - METHOD 'B'

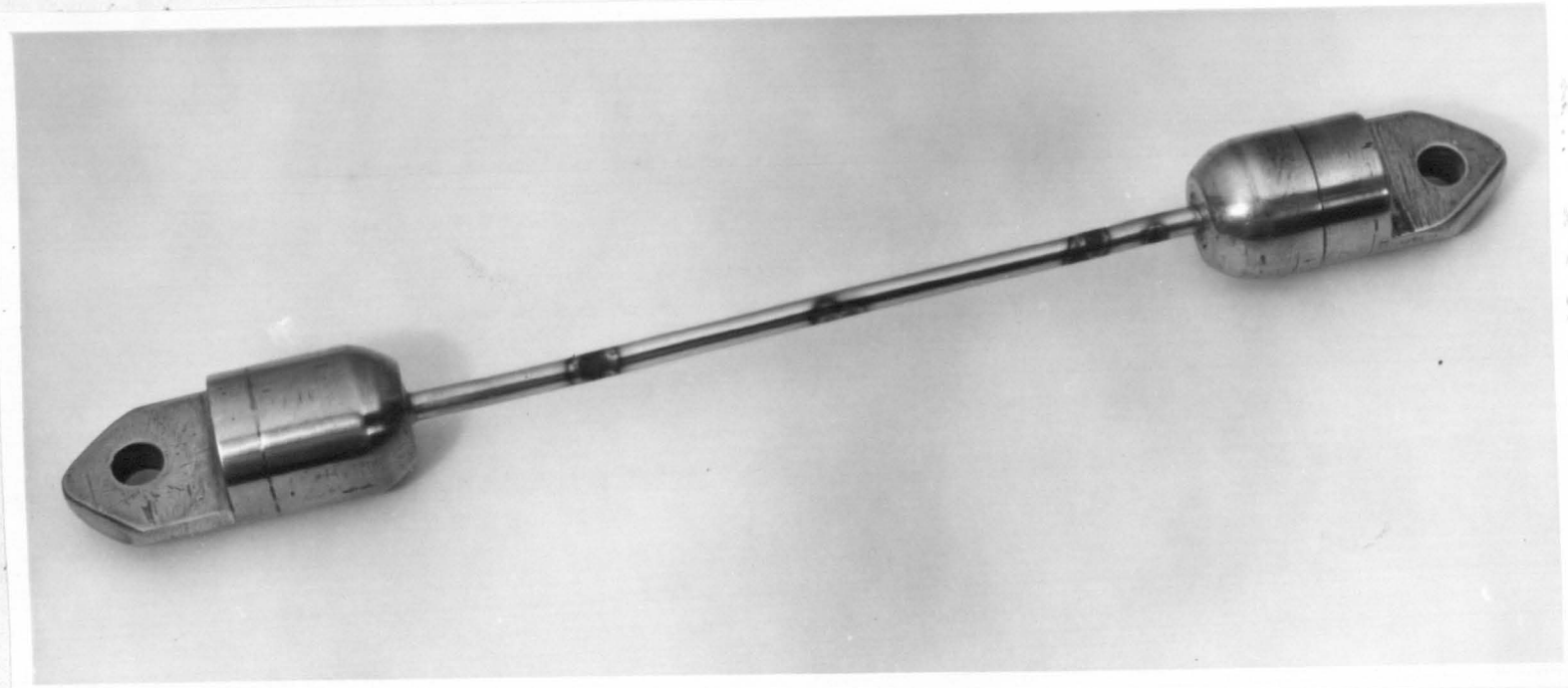

FIG. 10 HEATER SPECIMEN SHOWING CRITICAL HEAT FLUX POSITIONS

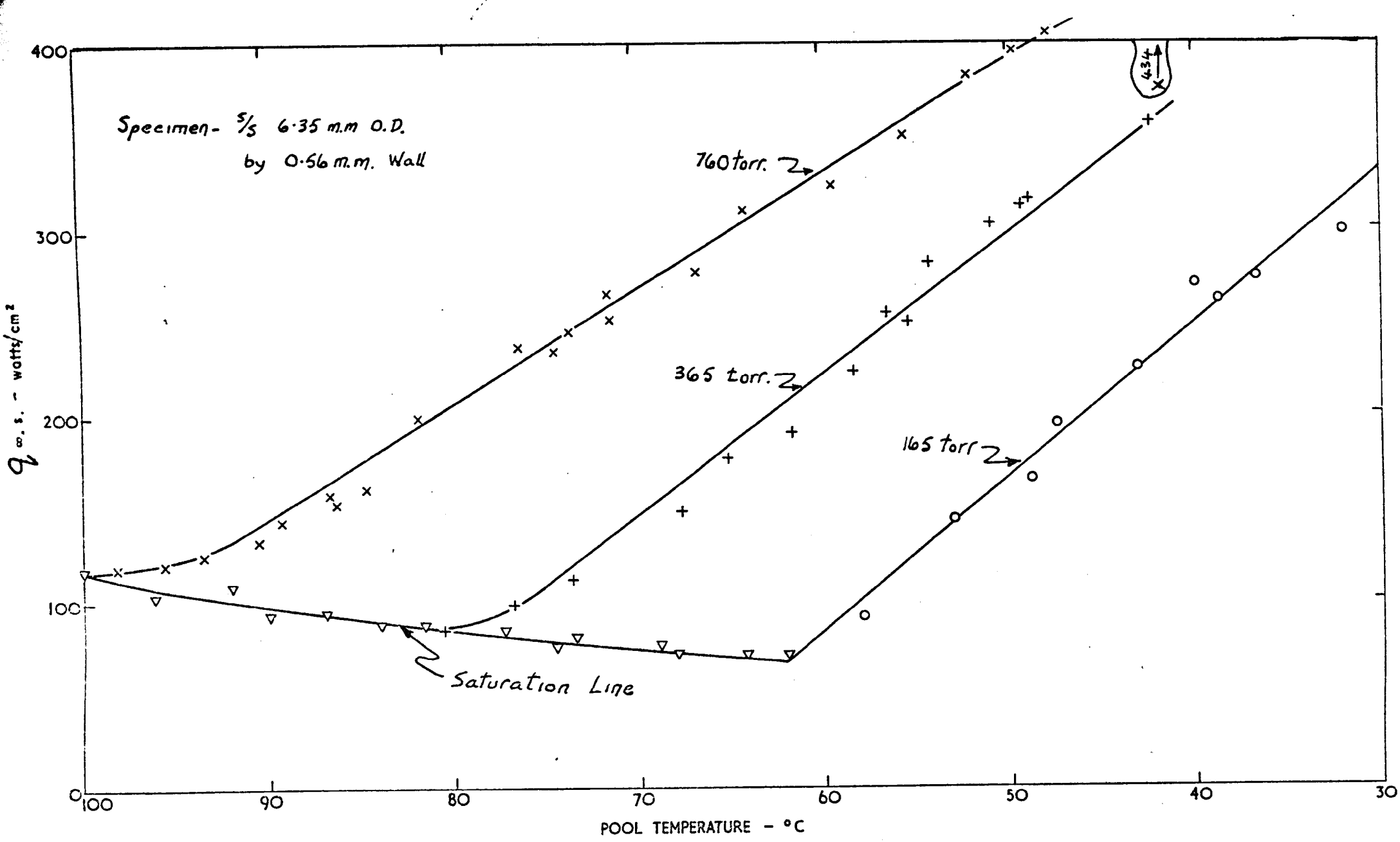

FIG.11. TYPICAL SET OF CRITICAL HEAT FLUX RESULTS UNDER ATMOSPHERIC AND VACUUM CONDITIONS

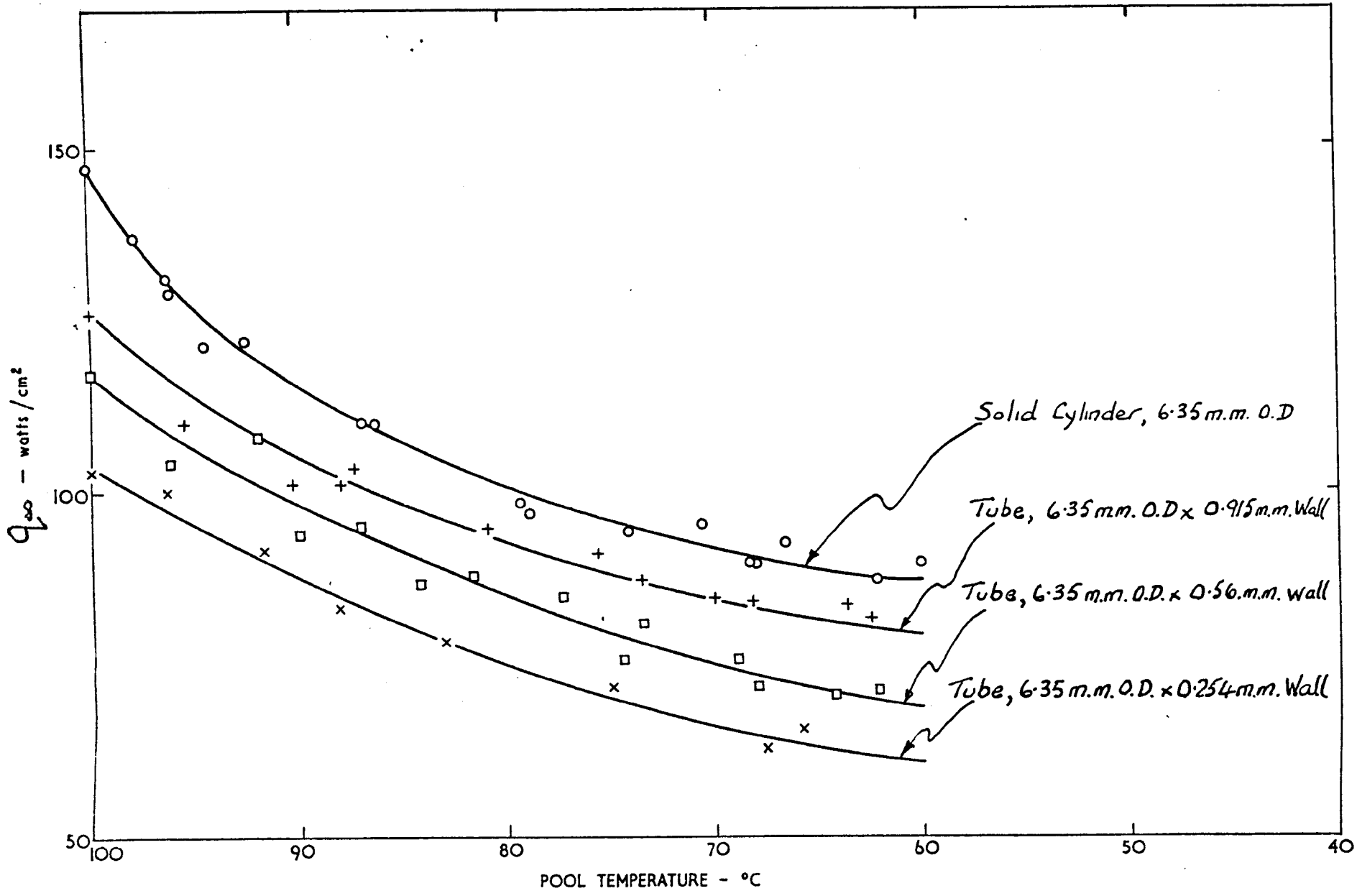

FIG. 12 CRITICAL HEAT FLUX RESULTS FOR SATURATED BOILING UNDER VACUUM ($R^1 > 1{\cdot}0$)
(HEATER WALL THICKNESS VARIED)

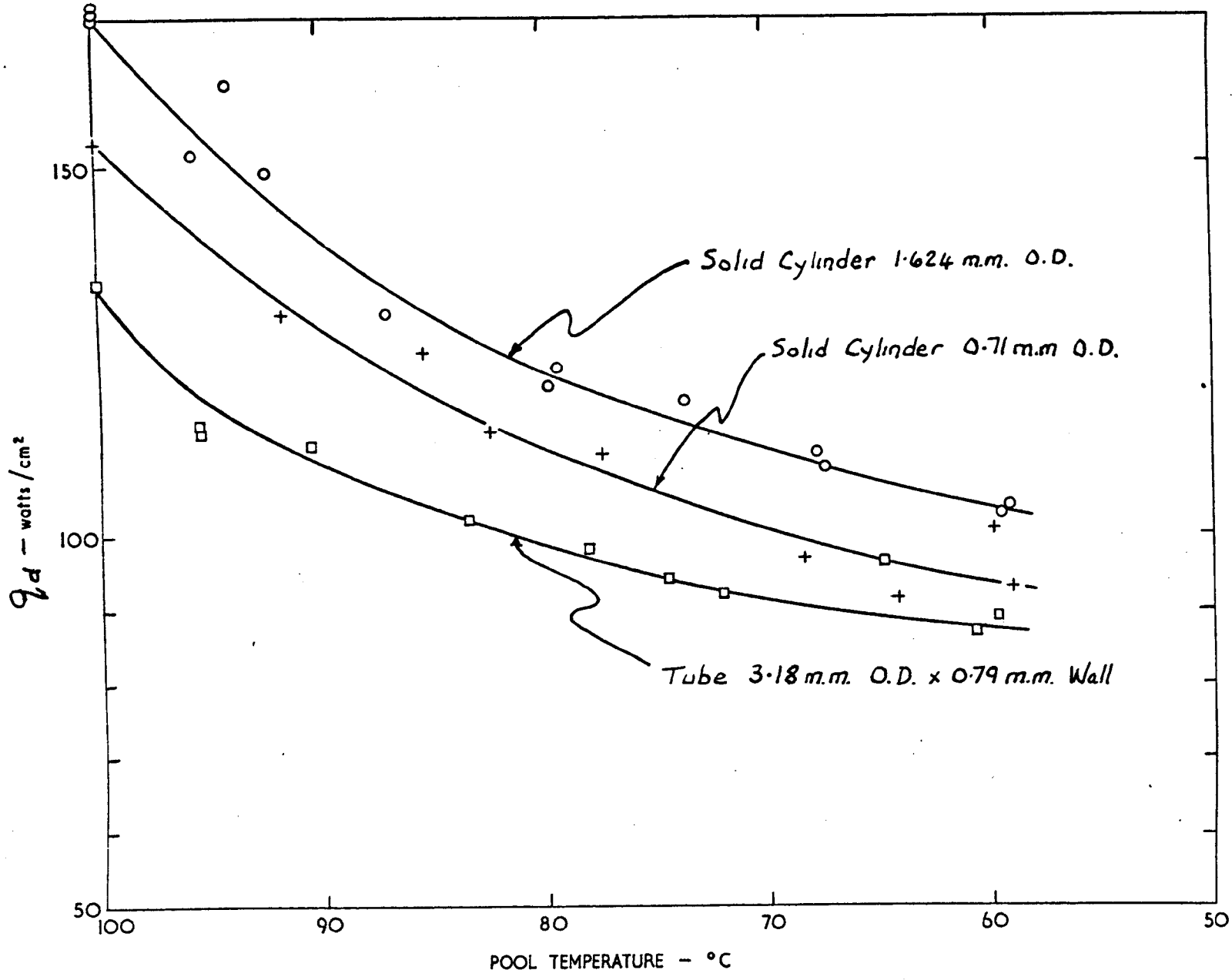

FIG.13. CRITICAL HEAT FLUX RESULTS FOR SATURATED BOILING UNDER VACUUM ($R^1 < 1{\cdot}0$)

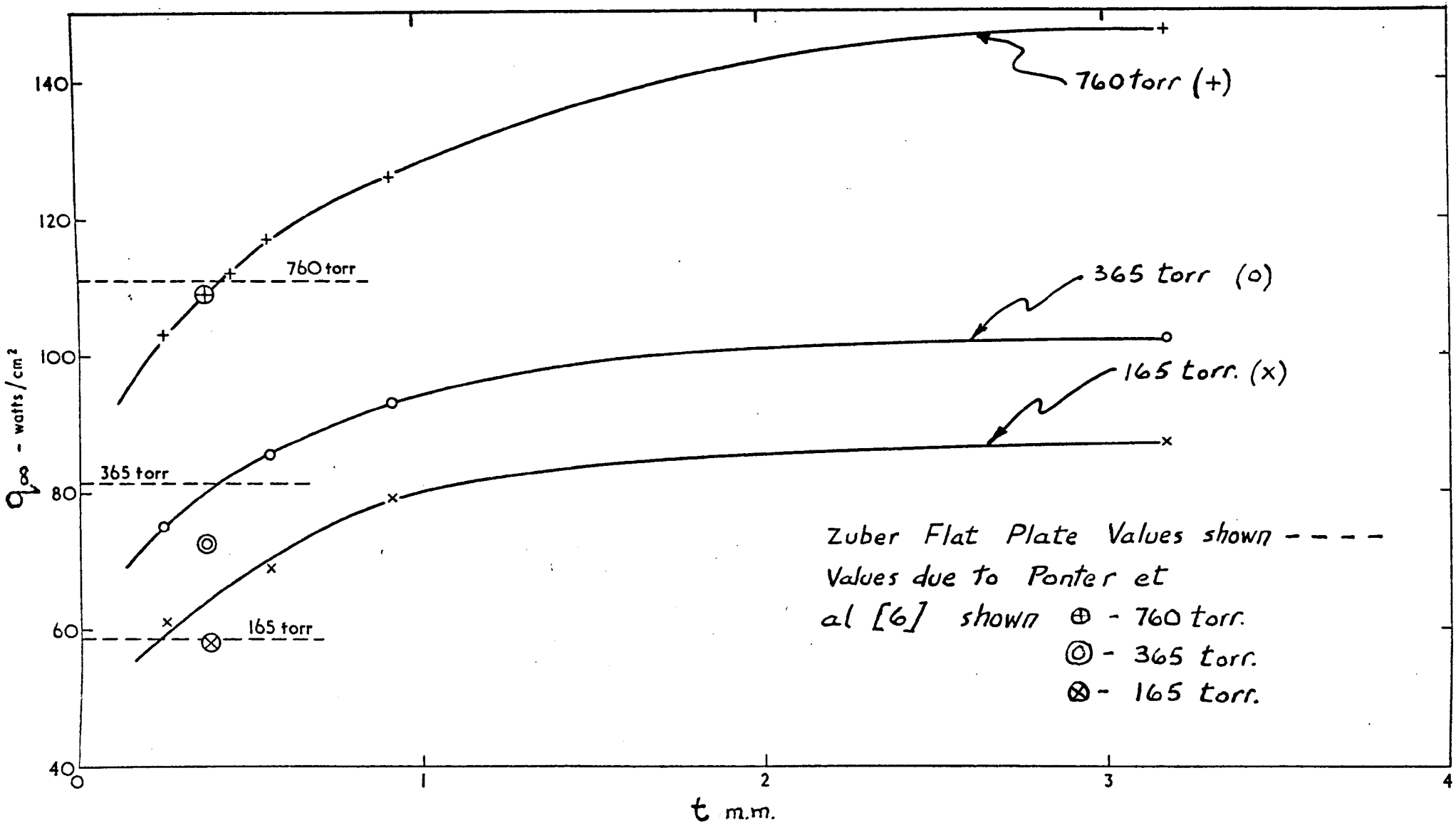

FIG. 14. CRITICAL HEAT FLUX VERSUS TUBE WALL THICKNESS / ROD RADIUS FOR SATURATED BOILING UNDER VACUUM ($R^1 > 1{\cdot}0$)

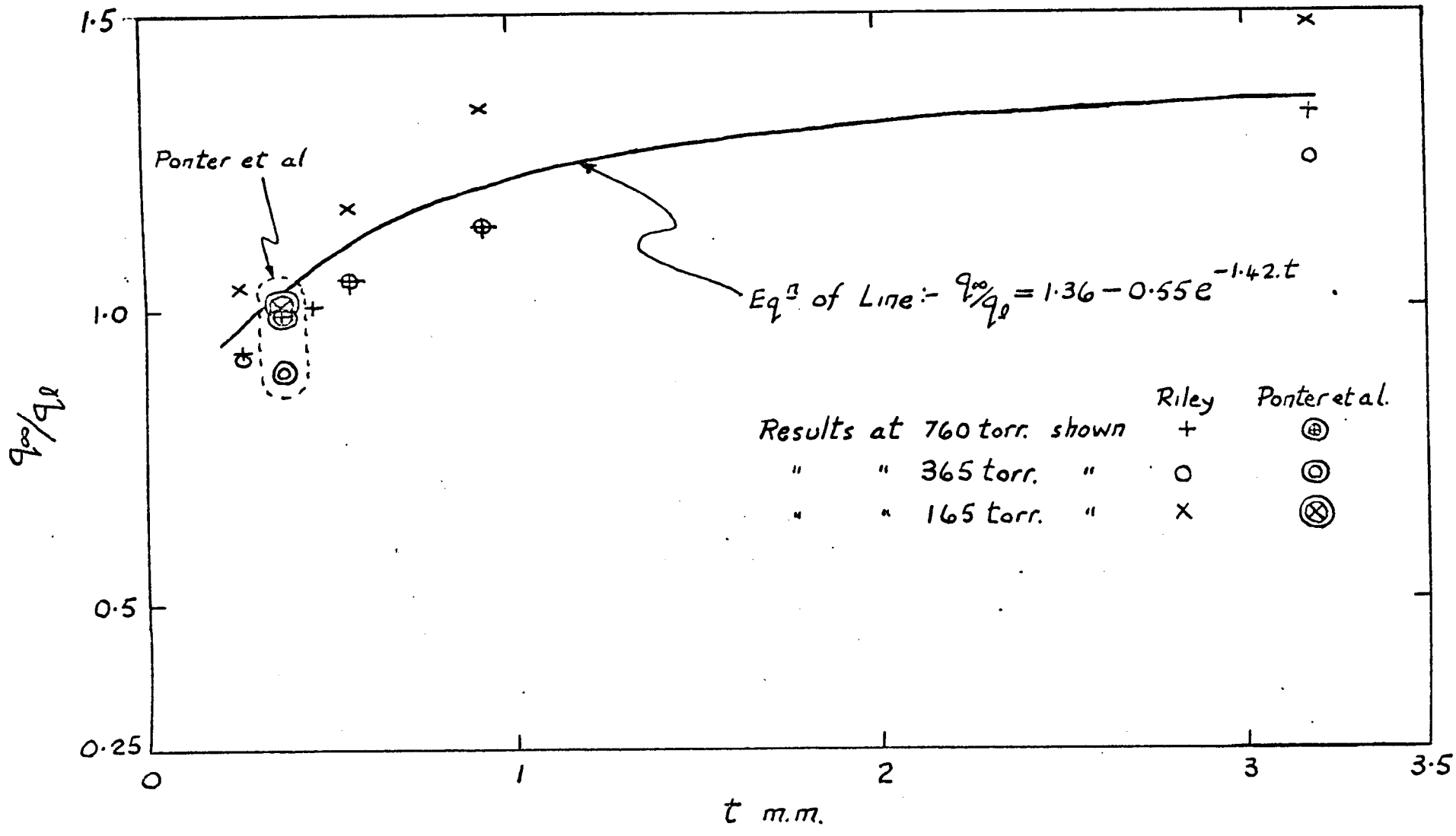

FIG. 15. DIMENSIONLESS CRITICAL HEAT FLUX VERSUS TUBE WALL THICKNESS - ROD RADIUS FOR SATURATED BOILING CONDITIONS ($R' > 1{\cdot}0$)

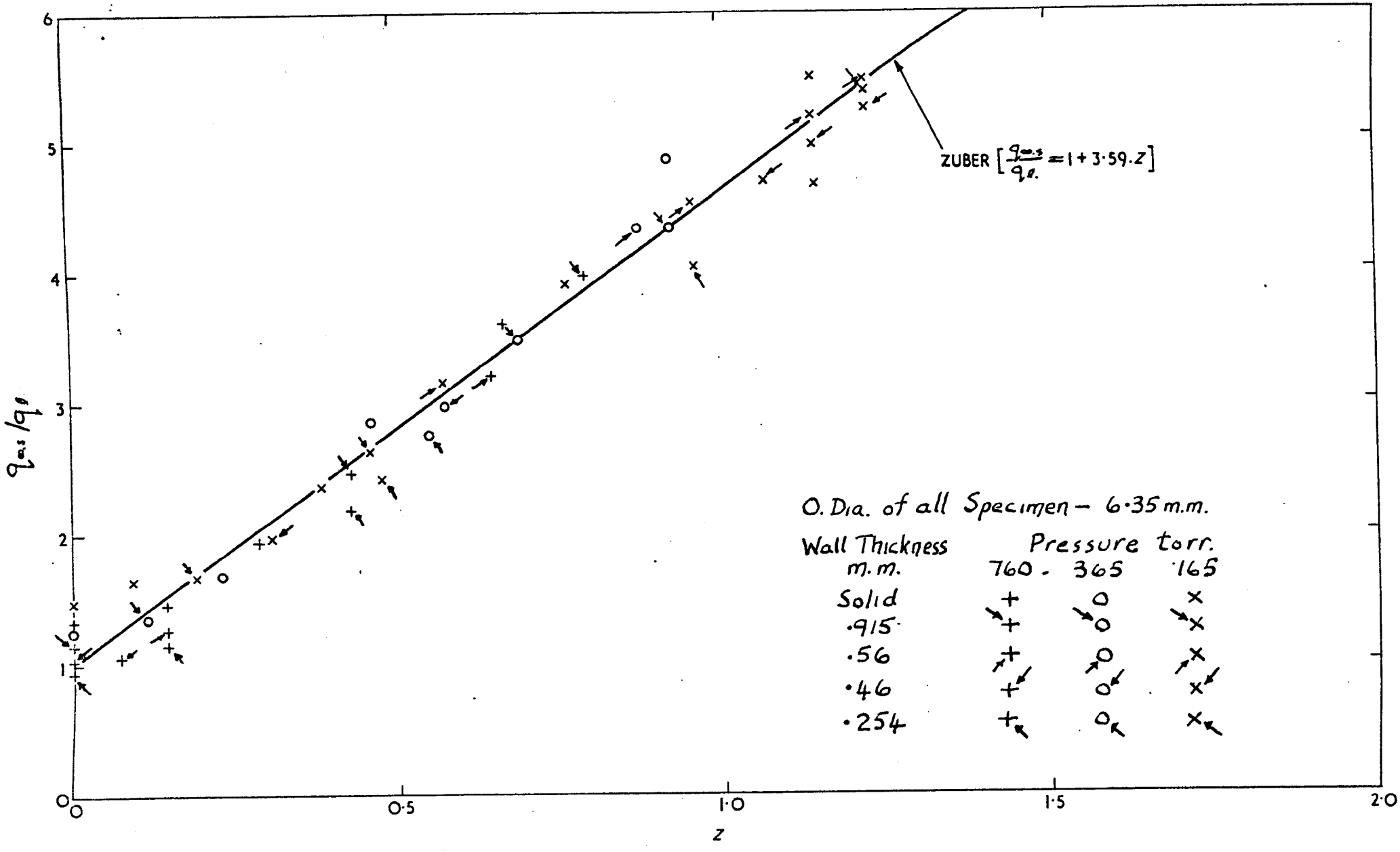

FIG. 16. COMPARISON OF MEAN EXPERIMENTAL CRITICAL HEAT FLUX VALUES ($P' > 1{\cdot}0$) FOR SATURATED AND SUBCOOLED CONDITIONS WITH THE 'ZUBER' PREDICTION

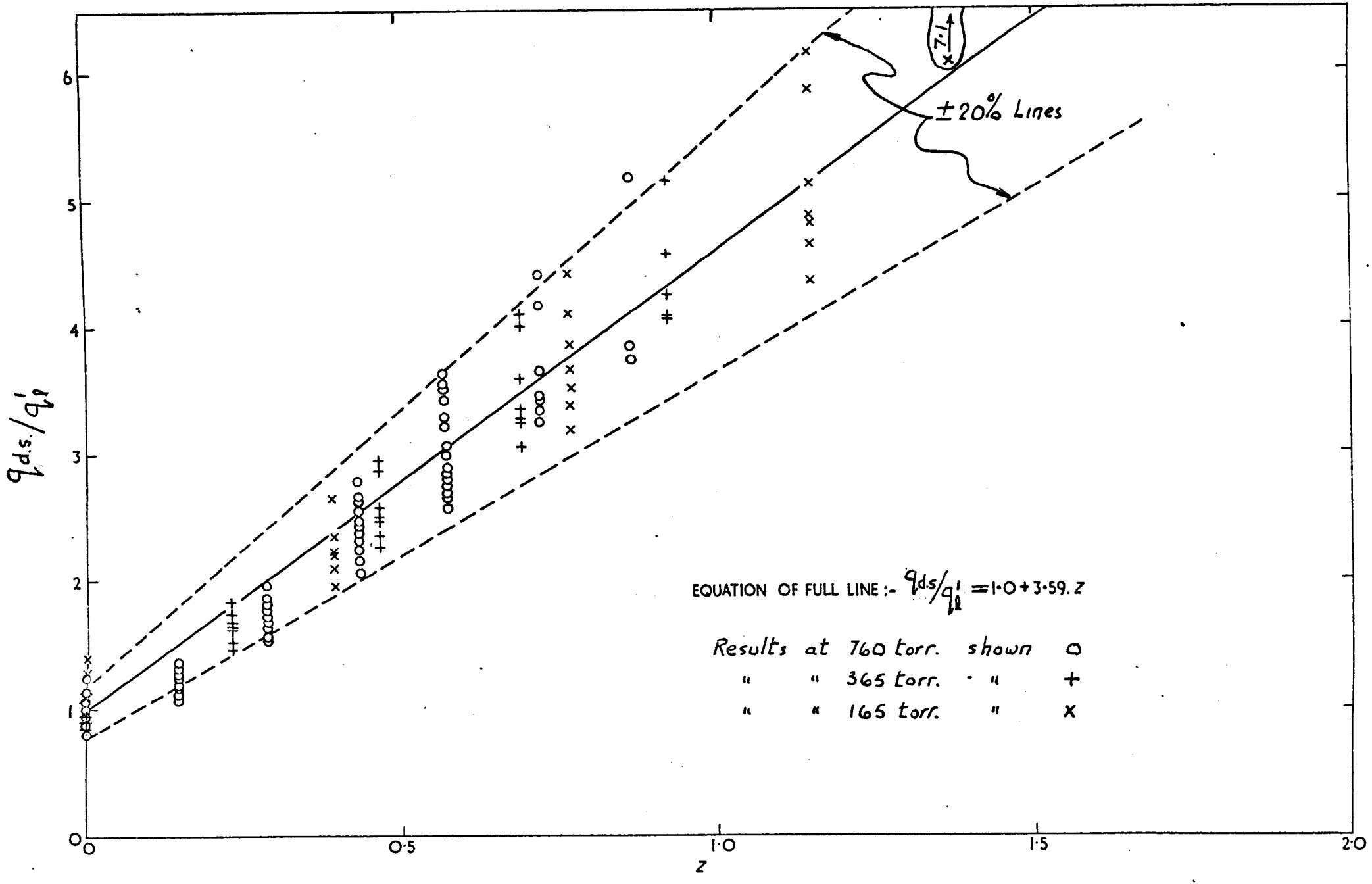

FIG.17. CORRELATION OF MEAN EXPERIMENTAL CRITICAL HEAT FLUX VALUES FOR ALL SPECIMENS TESTED ($R^1 > 0{\cdot}13$)

R m.m.	t m.m.	760 torr. R'	760 torr. A	$q_{d.s}/q'_{\ell}$ at 760 torr. Pool Subcooling °C 0	10	20	30	40	50	60	365 torr. R'	365 torr. A	$q_{d.s}/q'_{\ell}$ at 365 torr. Pool Subcooling °C 0	10	20	30	40	165 torr. R'	165 torr. A	$q_{d.s}/q'_{\ell}$ at 165 torr. Pool Subcooling °C 0	10	20	30	36
3·18	0·254	1·26	0·94	·88	1·06	1·56	2·07	2·58			1·21	0·942	·87	1·46	2·26	3·06		1·18	0·94	·98	1·96	3·19	4·33	
	0·457			·96	1·12	1·62	2·16	2·7	3·24	3·76				1·51	2·36	3·23	4·06				2·1	3·38	4·65	
	0·56			1·0	1·19	1·71	2·25	2·8	3·35	3·87			·99	1·63	2·5	3·36	4·24			1·11	2·33	3·86	4·88	
	0·915			1·08	1·24	1·77	2·33	2·9	3·45				1·08	1·68	2·48	3·28	4·07			1·27	2·2	3·51	4·82	
	Solid			1·26	1·37	1·83	2·44	3·04	3·65				1·18	1·61	2·58	3·59	4·58			1·40	2·22	3·67	5·13	
2·41	0·254	0·96	0·97	·87	1·06	1·52	2·07																	
	0·56			1·03	1·19	1·64	2·17	2·73																
	0·79			1·09	1·22	1·66	2·25	2·84	3·43															
	Solid			1·22	1·35	1·87	2·54	3·21																
1·58	0·51	0·63	1·04	·93	1·14	1·68	2·48	3·28			0·61	1·05						0·59	1·054					
	0·79			1·04	1·21	1·79	2·65	3·53					1·04	1·72	2·87	4·0	5·15			1·27	2·32	4·1	5·85	7·15
	Solid			1·11	1·34	1·97	2·79	3·64	4·5	5·29														
1·18	0·38	0·47	1·10	·87	1·07	1·67	2·38	3·05																
	Solid			1·13	1·31	1·87	2·63	3·42	4·18															
0·812	Solid	0·32	1·21	1·13	1·26	1·84	2·67	3·51			0·31	1·27	1·1	1·82	2·95	4·10		0·30	1·23	1·29	2·65	4·41	6·15	
0·595	Solid	0·24	1·31	·96	1·16	1·78	2·55	3·3																
0·457	Solid	0·18	1·42	·85	1·19	1·78	2·39	3·0																
0·355	Solid	0·14	1·515	·81	1·17	1·69	2·17	2·67			0·135	1·535	·87					0·13	1·54	·94				

FIG. 18. SATURATED AND SUBCOOLED CRITICAL HEAT FLUX RATIOS FOR PRESSURES OF 760, 365, AND 165 TORR.

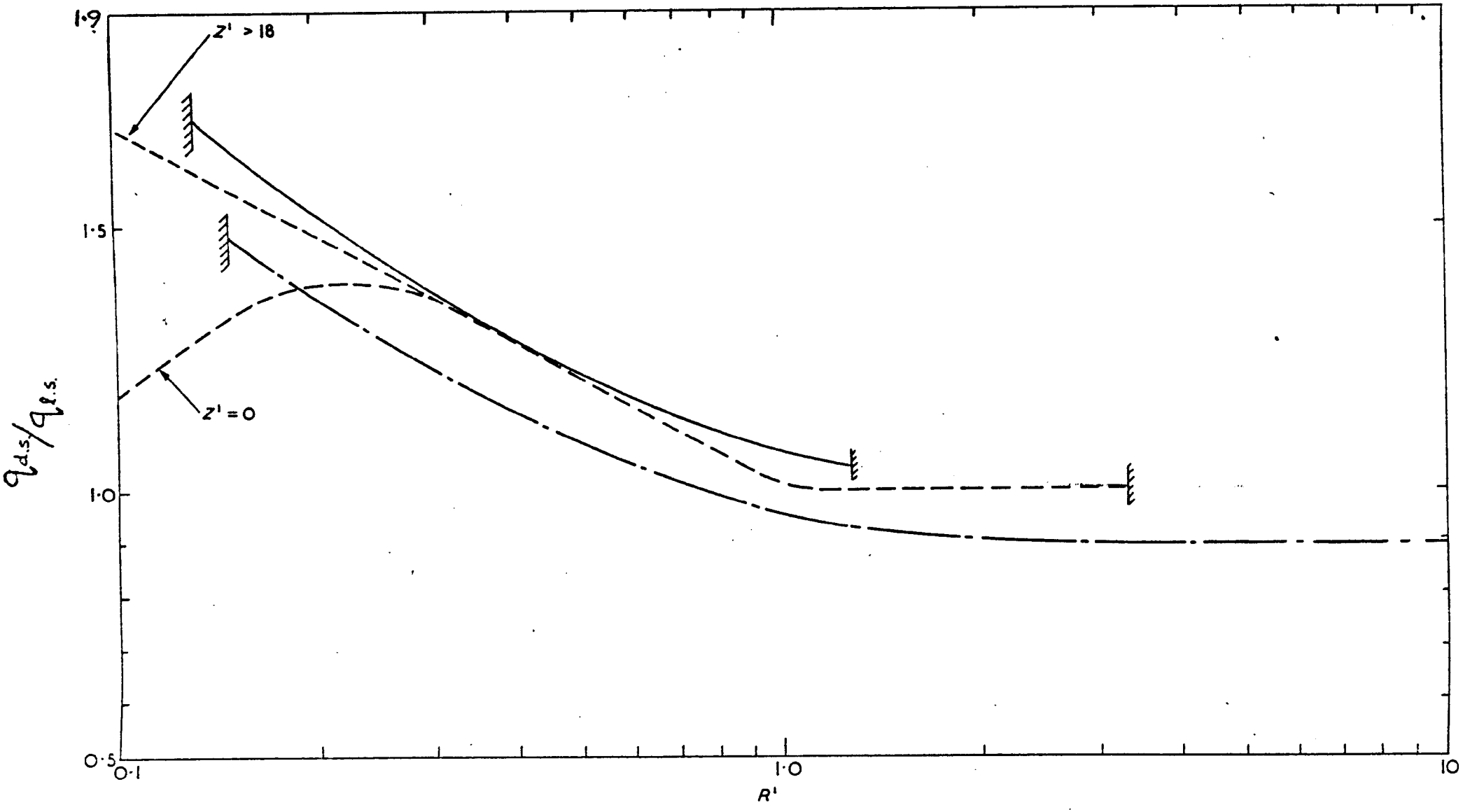

FIG.19. DIMENSIONLESS CRITICAL HEAT FLUX VERSUS SPECIMEN DIMENSIONLESS RADIUS. MEAN LINE DUE TO KUTATELADZE ET AL [10] SHOWN ----- MEAN LINE DUE TO SUN ET AL [9] SHOWN ——-—— MEAN LINE DUE TO RILEY SHOWN ————

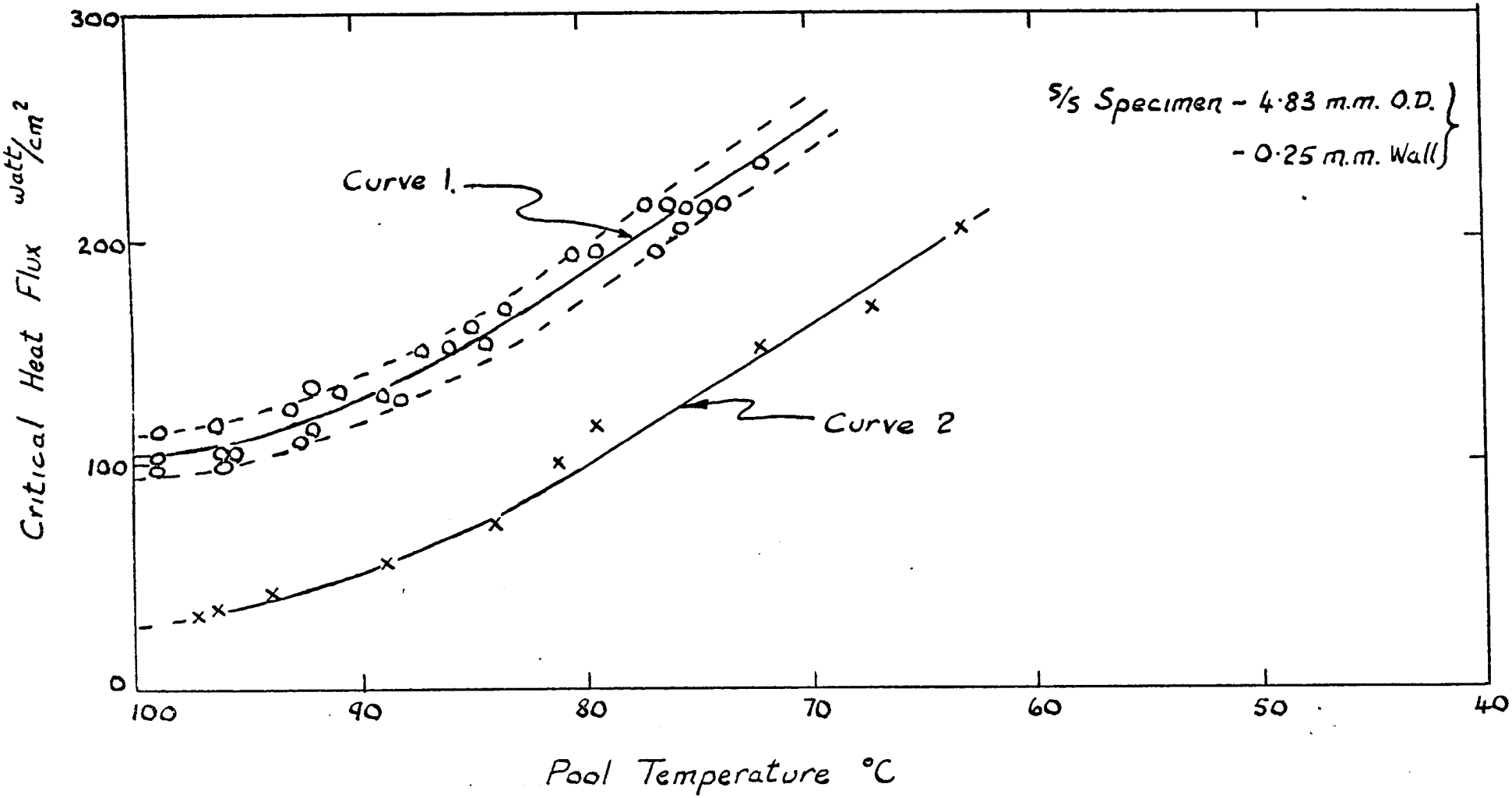

FIG. 20. CRITICAL HEAT FLUX VERSUS POOL TEMPERATURE FOR A HORIZONTAL HEATER AT ATMOSPHERIC PRESSURE

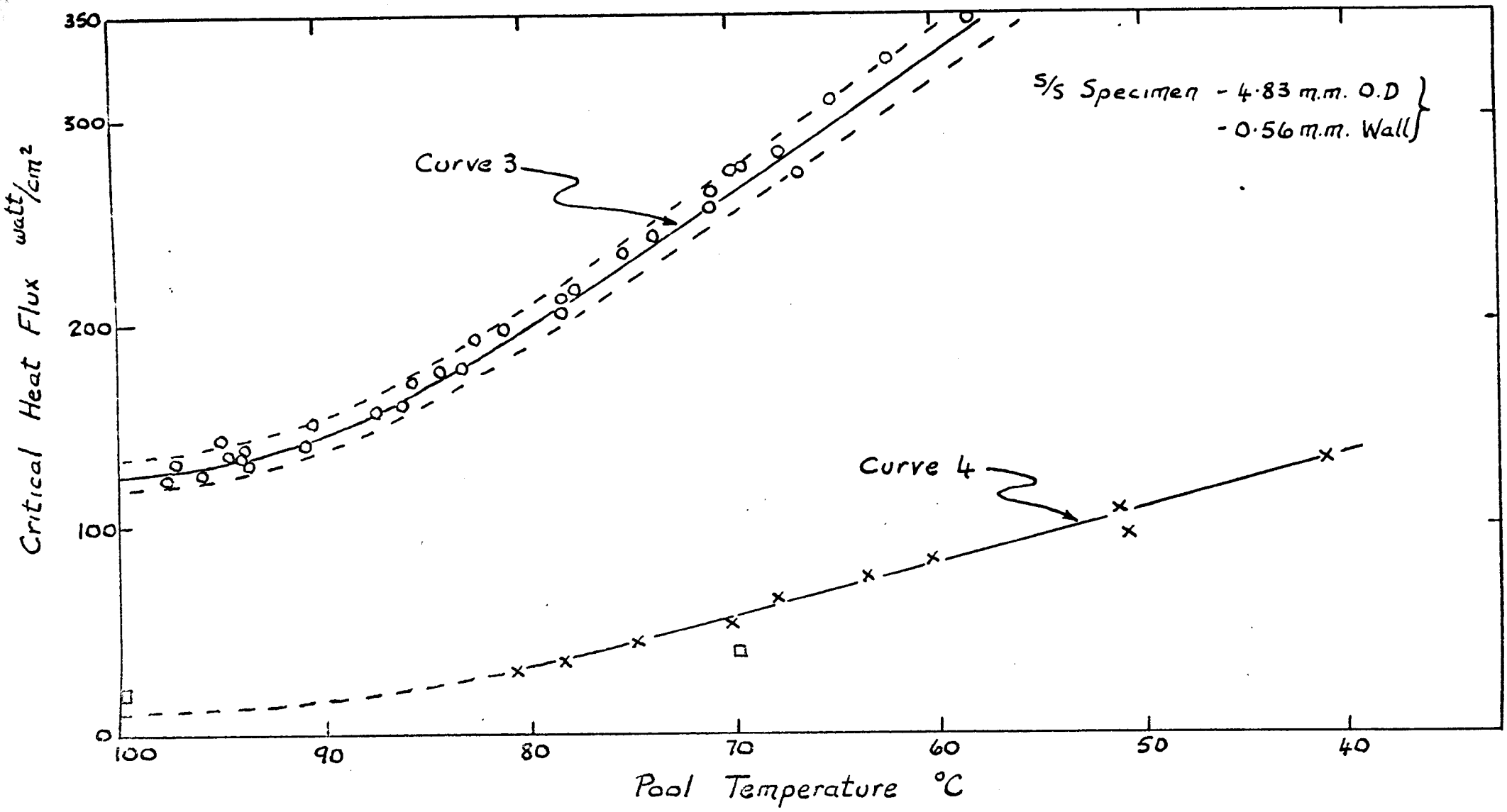

FIG. 21. CRITICAL HEAT FLUX VERSUS POOL TEMPERATURE FOR A HORIZONTAL HEATER AT ATMOSPHERIC PRESSURE

PART II

VERTICAL CONFINED BOILING AND VERTICAL POOL BOILING

14.0.0.

N O M E N C L A T U R E

P A R T II

NOMENCLATURE - PART II

A	parameter given by $\left[1 - \frac{1}{\rho_f \cdot g}\left(\frac{\tau_i+\tau_w}{\delta_i}\right)\right]_{A.M.}$
A_F	vapour flow area
B	parameter defined by $\frac{1}{\rho_f \cdot g}\left(\frac{\tau_i+\tau_w}{\delta_i}\right)$
C	parameter, variable with liquid viscosity
C_{pf}	specific heat of water
C_1	constant
dp/dx	axial pressure gradient
$dp/dx\|_R$	required axial pressure gradient
$dp/dx\|_A$	available axial pressure gradient
$dp/dx\|_{A.M.}$	maximum available axial pressure gradient
dv/dx	axial vapour velocity gradient
D	tube diameter
D_e	annulus hydraulic equivalent diameter, $(D_o - D_i)$
D_i	annulus inner or heated diameter
D_h	annulus heated equivalent diameter, $\frac{D_o^2 - D_i^2}{D_i}$
D_o	annulus outer diameter
D_p	parameter defined by $f_i\left(1 + \frac{\tau_o}{\tau_i}\frac{D_o}{D_i}\right)$
f_i	interfacial friction factor at inner surface
g	acceleration due to gravity
h_{fg}	enthalpy of vaporisation
H	effective height up annulus at which the water has reached its saturation temperature
j_g	volumetric vapour flux
j_f^*	dimensionless liquid velocity based on either D or D_h
j_g^*	modified dimensionless vapour velocity for saturated entry based on either D or D_h
J_g^*	dimensionless vapour velocity for saturated entry based on either D, or D_h

J^*_{gs}	modified dimensionless vapour velocity for subcooled entry based on either D or D_h
L	heated length
m	parameter, variable with liquid viscosity
m_f	water mass flow rate entering annulus
m_g	vapour mass flow rate leaving annulus
n	liquid recirculation parameter m_f/m_g
Na	annulus geometry number
Nc	capillarity number
Ne	thermal expansion number based on D or D_h
Nei	modified annulus thermal expansion number, i.e. Ne (based on D_h) x Na
N_f	liquid viscosity number, $Di^{3/2}.g^{\frac{1}{2}}.\vartheta_l^{-1}$
N_{fL}	liquid viscosity number, $L^{3/2}, g^{\frac{1}{2}}, \vartheta_l^{-1}$
N_s	shape number based on either D or D_h
p	pressure
q	heat flux or critical heat flux for saturated entry
q_s	heat flux or critical heat flux for subcooled entry
Re_g	superficial vapour Reynolds number
S	parameter defined by $(q_s/q - 1).\Delta T_s^{-1}$
T_p	pool water temperature
T_s	water saturation temperature
ΔT_s	pool water subcooling, $(T_s - T_p)$
U	circulation number
V, or V_g	vapour axial velocity
x	distance up annulus from start of heating
x^1	vapour dryness fraction
Y	parameter defined by $4.J^*_g.N_s^{-\frac{1}{2}}$
Y^*_g	parameter defined by $Y/4$
δ_i	water film thickness on heater surface
ρ_f	water density
ρ_g	vapour density
ϑ_f	specific volume of water
ϑ_g	specific volume of vapour
ϑ_l	Kinematic viscosity of water

σ	surface tension of water
τ_i	interfacial shear stress between water film and vapour core at annulus inner surface
τ_o	interfacial shear stress between water film and vapour core at annulus outer surface
τ_w	heater wall shear stress acting on water film

15.0.0.

INTRODUCTION AND LITERATURE SURVEY

INTRODUCTION AND LITERATURE SURVEY

The critical or limiting heat flux for heat transfer under two phase counter current flow conditions is of interest in the field of reactor technology because it is, in effect, a simulation of the blocked coolant channel accident condition. This accident condition can occur in water cooled nuclear reactors in which the core cooling water normally flows upwards through the fuel element cooling channels. If one of these cooling channels becomes blocked by some foreign body during normal reactor operation then the cooling water supply, which normally enters this channel at its base, would have to enter the channel at its top. Also since such water entry conditions would probably give rise to vapour production within the affected channel and since this vapour would leave the channel at its top then we have a two phase counter current flow situation established within a channel within the reactor core. Thus it is of interest to know the critical or limiting heat flux for reactor operation under such an accident condition and to gain an understanding of the mechanisms involved in such a situation.

The possible similarity between the mechanism that causes the limiting heat flux in a boiling blocked channel and that which causes flooding in a channel under two component counter current flow has been recognised for some time. Wallis (1) carried out early investigations into the flooding mechanism using air and water in tubes and successfully correlated his own and others results using a dimensionless relationship of the following form:

$$j_g^{*\frac{1}{2}} + m.\, j_f^{*\frac{1}{2}} = C \qquad 1$$

The parameters "m" and "C" are variable with liquid viscosity.

Much earlier Silver (2) when investigating circulation in water tube boilers derived and suggested the importance of the following dimensionless groups for boiling in tubes: the thermal expansion number N_e, the shape number N_s, the circulation function U, and the capillarity number N_C. He has more recently discussed their relevance and possible wider applicability (3,4).

An early paper that compared the critical vapour velocity for boiling in closed-end tubes to the flooding velocity in a counter current two component system was that presented by Griffith et al (5). These investigators concluded that "the order of magnitude of the burn-out heat flux for long closed end tubes can be calculated using the critical flooding velocity".

Gambill (6) has reported results for burnout of blocked vertical channels cooled internally by water. The channels used were mainly tubes although a few test results were reported for square sectioned channels. Results were obtained for both saturated and subcooled liquid entry. Wallis (7) using the results of Gambill and others showed that these results for blocked boiling channels were compatible with the two component flooding relationship (Equation 1). The actual comparison is given on Fig. 14.17 of (7).

Further work for the tube geometry has been reported by Frea (8) in which the system gravity was varied. This investigator postulated that in addition to the dimensionless gas flux, as used by Wallis, flooding in tubes also depended upon a modified gas Reynolds number, the liquid-gas Kinematic viscosity ratio, and the relative liquid layer thickness. However the final correlation presented by this author, using his own and others results, was in graphical log-log form (see ref. (8), Figs. 11 and 12) in which both the ordinate and the abscissa contained the modified gas Reynolds number in the numerator. A straight line of slope unity fits all the points presented almost as well as the curve offered by the author. For the ordinates used this implies very little, if any, dependance on the modified gas Reynolds number over the range reported.

The present study concerns the limiting heat flux for a centrally heated, bottom blocked annulus (see Fig. 5) for which the entry water temperature conditions vary from subcooled to saturation. As boiling occurs within the channel the problem is one of two phase counter current flow. For

the tests the heater length was essentially constant but the annulus outer and inner diameters have been varied at atmospheric pressure and under vacuum conditions.

The only other investigation using the annulus geometry and counter current flow of which the author is aware is that due to Shires et al (9). In this work a 366 cm long vertical test section was used, with a central heater rod of 1.59 cm outside diameter and an annulus outer wall diameter of 2.54 cm. The work was carried out at atmospheric pressure and annulus geometry variation was not investigated. To the authors knowledge therefore the work presented represents the first systematic investigation of annulus geometry variation at atmospheric pressure and under vacuum conditions for the present experimental situation.

16.0.0.

T H E O R Y

THEORY

16.1.0. Introduction

The authors initial approaches to correlating the two phase counter current flow critical heat flux results obtained in this section of the investigation went along two separate lines. One was an attempt to adapt the approach of Wallis (1), using his dimensionless gas velocity parameter, j_g^* to the present situation. In his investigations of two component annular counter current flow flooding in tubes Wallis successfully correlated his results in terms of two dimensionless parameters, j_g^* and j_f^*. The first, j_g^*, is a dimensionless gas velocity parameter, the second j_f^*, is a dimensionless liquid velocity parameter, and they are defined by the following relationships.

a) Dimensionless Gas Velocity, j_g^*

$$j_g^* = \frac{\rho_g^{\frac{1}{2}} \cdot j_g}{\left[g.D.(\rho_f - \rho_g)\right]^{\frac{1}{2}}} \qquad 2$$

b) Dimensionless Liquid Velocity, j_f^*

$$j_f^* = \frac{\rho_f^{\frac{1}{2}} \cdot j_f}{\left[g.D.(\rho_f - \rho_g)\right]^{\frac{1}{2}}} \qquad 3$$

No heat transfer or vaporisation of the liquid phase was involved in this initial development. However subsequently this approach was adapted to two phase counter current flow problems with heat transfer by employing, in place of the volumetric gas flux, the maximum volumetric vapour flux as calculated by a thermal balance. Now in the two component situation without heat transfer the gas component velocity would not vary with test section height. In the two phase situation with heat transfer the vapour phase velocity increases throughout the test section height (for saturated liquid entry). The critical situation is therefore likely to be controlled by local conditions where the vapour velocity is a maximum. Further in the development of j_g^* Wallis (15) only considered shear forces and buoyancy forces to be acting, which is, of course, correct in two component systems with no heat transfer.

However in annular two phase flow systems with heat transfer when vaporisation of the liquid phase is occurring then the vapour momentum is continuously increasing up the channel. Thus additional forces are necessary to produce this vapour momentum increase. There are thus three possible relevant forces - buoyancy forces, friction or shear forces, and vapour momentum forces. As shown in a later section this extra force leads to other possible relevant dimensionless groupings, apart from j_g^*.

The other approach taken by the author was to employ the dimensionless numbers as developed by Silver (2,3) for the tubular geometry, in his paper on the theory of circulation in water tube boilers. These numbers were developed for a situation in which liquid vaporisation was occurring. The dimensionless numbers are as follows:

a) Circulation Number, U

$$U = \left(\frac{\rho_f - \rho_g}{\rho_g}\right) . x^1 \qquad 4$$

b) Shape Number, N_s

$$N_s = L/D \qquad 5$$

c) Thermal Expansion Number, N_e

$$Ne = \frac{2.q^2.(v_g - v_f)^2}{g.h_{fg}^2.D} \qquad 6$$

$$= \frac{2.q^2.(\rho_f - \rho_g)^2}{(\rho_f.\rho_g)^2.g.h_{fg}^2.D} \qquad 7$$

d) Capillarity Number, Nc

$$N_c = \frac{\sigma^2.g}{q^2.D} \qquad 8$$

However it soon became clear to the author that the dimensionless gas velocity, j_g^*, as developed by Wallis, when applied to a two phase flow situation with heat transfer, could be expressed completely in terms of the dimensionless numbers due to Silver, (U, N_s and N_e). That this is so is shown by the

author in the next section.

16.2.0. Relationship between j_g^* and N_e, N_s and U for the tubular geometry with countercurrent annular flow

The adjacent diagram shows a tubular thermosyphon in which the heat flux passes to the annular liquid film from the tube wall. The bottom blocked heated tube is of length, L, and diameter, D. The water supply to the tube is at the saturation temperature corresponding to the system pressure.

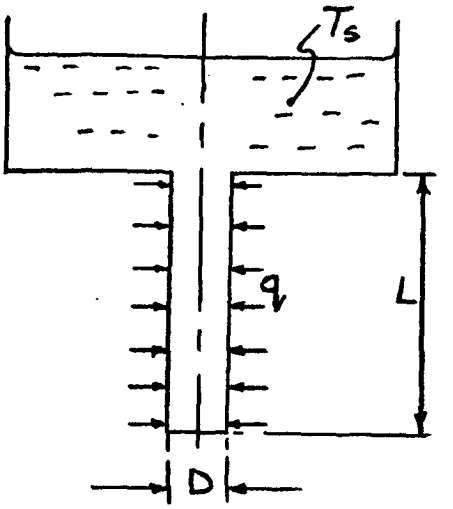

Bottom Blocked Tube

An energy balance applied to the system gives

$$q.\pi.D.L. = \rho_g.\, j_g.\frac{\pi}{4}.\, D^2.h_{fg}$$

where j_g is the maximum volumetric vapour flux for the tube

$$\therefore\ j_g = \frac{4.q.L}{\rho_g.h_{fg}.D} \qquad 9$$

Now equation 2 gives an expression for j_g^* in terms of j_g, therefore combining equations 2 and 9 we obtain

$$j_g^* = \frac{q}{\rho_g^{\frac{1}{2}}.h_{fg}} \cdot \frac{4.L}{D} \cdot \frac{1}{\left[g.D.(\rho_f-\rho_g)\right]^{\frac{1}{2}}} \qquad 10$$

Now by multiplying equation 7 by $\frac{\rho_f-\rho_g}{\rho_f-\rho_g}$ and taking the square root of both sides we obtain

$$\sqrt{\frac{N_e}{2}} = \frac{(\rho_f-\rho_g)^{3/2}.q}{\rho_f.\rho_g.h_{fg}\left[g.D.(\rho_f-\rho_g)\right]^{\frac{1}{2}}} \qquad 11$$

Combination of equations 10 and 11 enables us to obtain j_g^* in terms of N_e as follows

$$\sqrt{\frac{N_e}{2}} = j_g^* \cdot \frac{D}{4.L} \cdot \frac{\rho_g^{\frac{1}{2}}(\rho_f-\rho_g)^{3/2}}{\rho_f.\rho_g} \qquad 12$$

Equation 12 can be further rationalised by substituting for N_s from equation 5 and for U from equation 4 with the

dryness fraction x^1 equal to 1.0 as follows

$$\frac{4}{\sqrt{2}} \cdot \sqrt{N_e} = j_g^* \cdot \frac{U^{3/2}}{N_s} \cdot \frac{\rho_g}{\rho_f} \qquad 13$$

Now if we make the assumption that for most practical situations $\rho_f >> \rho_g$ and therefore $\rho_g/\rho_f \equiv \frac{1}{U}$ with $x^1 = 1.0$, then equation 13 becomes

$$\frac{j_g^*}{2\sqrt{2}} = \sqrt{\frac{N_e . N_s^2}{U}} \qquad 14$$

Now if we write $J_g^* = \sqrt{\frac{N_e . N_s^2}{U}}$ 15

then we obtain the final form of the required relationship as

$$J_g^* = \sqrt{\frac{N_e . N_s^2}{U}} = \frac{j_g^*}{2\sqrt{2}} \qquad 16$$

We can thus conclude, for counter current annular flow in tubes, that the parameter developed by Wallis to define the flooding condition, j_g^*, when written in terms of the maximum volumetric vapour flux can be expressed completely in terms of the dimensionless numbers, N_e, N_s and U, due to Silver.

16.3.0. Development of j_g^* due to Wallis

Now Wallis (15) developed the dimensionless gas parameter, j_g^*, for two component counter current annular flow in a tube (Dia. 'D') by assuming that the only important forces acting on the gas component at the flooding condition were shear forces and buoyancy forces. Therefore Wallis argued that a gas parameter derived from the ratio of these two forces over a given length of tube would be a relevant parameter. Thus, neglecting the volume occupied by the water films,

$$\frac{\text{Shear force}}{\text{Buoyancy force}} \propto \frac{f_i . \rho_g . V_g^2 . \pi . D . L}{(\rho_f - \rho_g) \frac{\pi}{4} . D^2 . L . g} \qquad 14.1$$

$$\therefore \frac{\text{Shear force}}{f_i . \text{Buoyancy force}} \propto \frac{\rho_g . V_g^2}{(\rho_f - \rho_g) . g . D .} = j_g^{*2} \qquad 15.1$$

It is seen, by reference to equation 15.1 that the parameter, j_g^{*2}, is proportional to the ratio of the shear force acting on the gas element of length 'L' divided by the product of the interfacial friction factor and the buoyancy force act-

ing on the same gas element.

16.4.0. Tubular Geometry with Evaporation

In a tubular annular two phase counter current flow system in which progressive evaporation occurs up the tube, the vapour velocity is continuously increasing up the tube (for saturated liquid entry) and therefore the maximum vapour velocity occurs at the tube top. Thus the interfacial shear force acting on the vapour will be a maximum at the tube outlet. Further because the vapour momentum is increasing up the tube, some of the driving buoyancy force is taken up in supplying this momentum increase. Since the momentum force depends on the product $V_g.dV_g$, then this force is also a maximum at the tube top. Therefore at the limiting heat flux situation if a significant proportion of the driving buoyancy force is taken in increasing the vapour momentum then the following force ratio could be of importance. Neglecting the volume occupied by the liquid films then we obtain

$$\frac{\text{Momentum Force}}{\text{Buoyancy Force}} \propto \frac{\rho_g.\frac{\pi}{4}.D^2.V_g.dV_g}{(\rho_f-\rho_g)\frac{\pi}{4}.D^2.g.dx} \qquad 16.1$$

Now a thermal balance on this tubular thermo-syphon system with a wall constant heat flux gives us for the vapour velocity at any height 'x' up the heated tube:

$$V_g = \frac{4.q.x}{\rho_g.h_{fg}.D} \qquad 17$$

and thus differentiating equation 17 w.r.t. x gives

$$dV_g = \frac{4.q.dx}{\rho_g.h_{fg}.D.} \qquad 18$$

therefore if we substitute equations 17 and 18 into equation 16.1 and put x = L to obtain the maximum value of this force ratio, we get

$$\left.\frac{\text{Momentum Force}}{\text{Buoyancy Force}}\right|_{x=L} \propto \frac{q^2.L}{\rho_g.h_{fg}^2(\rho_f-\rho_g).g.D^2} \qquad 19$$

Now we can rewrite equation 19 in terms of the dimensionless numbers due to Silver, provided we put the exit

vapour dryness fraction $x^1 = 1.0$ in 'U' and we make the assumption that $\rho_f >> \rho_g$ thus:

$$\left.\frac{\text{Momentum Force}}{\text{Buoyancy Force}}\right|_{x = L} \propto \frac{N_e . N_s}{U} \qquad 20$$

As equation 20 represents a new force ratio we can define a new dimensionless parameter as follows

$$Y^{*2}_g = \frac{N_e . N_s}{U} \qquad 21$$

Y^*_g will attain a significance in systems with evaporation when the vapour momentum increase force is significant.

Now we can combine equations 16 and 21 to obtain

$$\frac{J^{*2}_g}{Y^{*2}_g} = N_s \propto \left.\frac{\text{Shear Force}}{f_i . \text{ Momentum Force}}\right|_{x = L} \qquad 22$$

We can therefore conclude that for tubular systems in which buoyancy, momentum, and shear forces are important at the critical heat flux condition, that the critical heat flux results will, at least, be dependant on any two of the following three dimensionless parameters: J^*_g, Y^*_g, N_s and upon the interfacial friction factor, f_i.

16.5.0. ANNULAR GEOMETRY WITH EVAPORATION

16.5.1 Introduction

For the situation investigated experimentally the geometry is not a bottom blocked tube as discussed in the "theory" so far, but a bottom blocked annulus with its outer surface adiabatic and its inner surface heated - as indicated in the adjacent diagram.

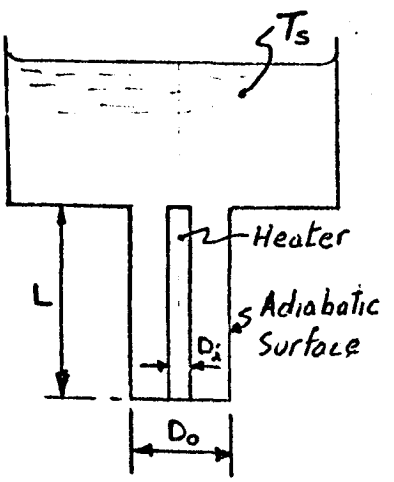

Bottom Blocked Annulus

We will now, using similar arguments to those employed previously for the tubular geometry develop dimensionless parameters from force ratio arguments applicable to the annulus geometry situation. If we assume for the annulus geometry that the critical heat flux is dependant upon, at least, the following three forces: buoyancy, shear, and vapour momentum increase, then we can look for dimensionless

parameters derived from these force ratios in a similar manner to that used by Wallis, and by the present author, for the tube geometry previously discussed.

16.5.2. J^*_g for Centrally Heated Annulus

Now for tubes J^*_g was derived from consideration of the shear force acting on the vapour core compared to the buoyancy force. For the annulus system considered the annular vapour core is subject to an interfacial shear force on both its inner and outer surface. Since in the present investigation heat transfer occurs only from the inner annulus surface and the critical situation occurs when the liquid film on this inner surface is destroyed, then the relevant shear force acting will be considered by the author to be that acting on the inner vapour surface. Therefore neglecting the volume occupied by the liquid films we will consider the force ratio for an element of vapour annulus, of length, dx, as follows:

$$\frac{\text{Inner Shear Force}}{\text{Buoyancy Force}} = \frac{\tau_i . \pi . D_i . dx}{(\rho_f - \rho_g) \frac{\pi}{4}(D_o^2 - D_i^2) . g . dx} \qquad 23$$

If we assume that we can write for the inner interfacial shear stress, τ_i, that

$$\tau_i \propto f_i . \rho_g . V_g^2 \qquad 24$$

where f_i represents the interfacial friction factor for the inner vapour-liquid interface at the critical situation and V_g represents the average vapour velocity at the annulus exit (for saturated liquid entry) then equation 23 becomes

$$\frac{\text{Inner Shear Force}}{f_i . \text{Buoyancy Force}} \propto \frac{\rho_g V_g^2}{(\rho_f - \rho_g) . g . D_h} \qquad 25$$

where D_h represents the annulus heated equivalent diameter:

$$D_h = \frac{D_o^2 - D_i^2}{D_i} \qquad 26$$

Now a thermal balance applied to this heated annulus system with an inner wall constant heat flux, q, gives us an express-

ion for the maximum vapour velocity which occurs at the annulus exit:

$$V_g = \frac{4.q.L}{\rho_g.h_{fg}.D_h} \qquad 27$$

Substitution of equation 27 into equation 25 gives the maximum value of the force ratio as

$$\frac{\text{Inner Shear Force}}{f_i.\text{Buoyancy Force}} \propto \frac{q^2}{\rho_g^2.h_{fg}^2.g.D_h} : \frac{L^2}{D_h^2} \cdot \frac{\rho_g}{(\rho_f-\rho_g)} \qquad 28$$

If we redefine N_s and N_e so that they are now based on the annulus heated equivalent diameter, D_h, and substitute these redefined dimensionless numbers into equation 28 inconjunction with U, with the assumption that the vapour dryness fraction at the annulus exit is unity and that $\rho_f >> \rho_g$ then we obtain

$$\frac{\text{Inner Shear Force}}{f_i.\text{Buoyancy Force}} \propto \frac{N_e.N_s^2}{U} \qquad 29$$

Now we can define the dimensionless parameter, J^*_g, for the annulus geometry as

$$J^{*2}_g = \frac{N_e.N_s^2}{U} \qquad 30$$

where, N_e, N_s and J^*_g are based on the annulus heated equivalent diameter, D_h.

IMPORTANT NOTE

It should be noted that from here on whenever J^*_g, N_e or N_s are used that they will be based on the annulus heated equivalent diameter, D_h, unless otherwise stated.

16.5.3 Y^*_g for Centrally Heated Annulus

For the tubular geometry, Y^*_g was derived by the author from a comparison of the vapour momentum force to the buoyancy force. We will now use a similar approach for the annular geometry. For the annular geometry, with its inner surface heated, subjected to countercurrent two phase annular flow with progressive evaporation, the vapour momentum is continuously increasing up the annulus. It therefore follows that some of the driving buoyancy force is absorbed in producing

the vapour momentum increase. Since the momentum force depends on the product $V_g.dV_g$ then this force will be a maximum at the annulus top where heating ceases. Therefore at the limiting heat flux situation, if a significant proportion of the driving buoyancy force is absorbed in increasing the vapour momentum then the following force ratio could be of importance. Neglecting the volume occupied by the liquid films we obtain

$$\frac{\text{Momentum Force}}{\text{Buoyancy Force}} \propto \frac{\rho_g \frac{\pi}{4}(D_o^2-D_i^2)\, V_g.dV_g}{(\rho_f-\rho_g)\frac{\pi}{4}(D_o^2-D_i^2).g.dx} \qquad 31$$

Now a thermal balance on this annular thermosyphon system with an inner wall constant heat flux gives us, for the vapour velocity at any height, 'x' up the annulus

$$V_g = \frac{4.q.x}{\rho_g.h_{fg}.D_h} \qquad 32$$

and thus, differentiating equation 32 w.r.t. 'x', gives

$$dV_g = \frac{4.q.dx}{\rho_g.h_{fg}.D_h} \qquad 33$$

Therefore if we substitute equations 32 and 33 into equation 31 and put x = L to obtain the maximum value of this force ratio, we obtain

$$\left.\frac{\text{Momentum Force}}{\text{Buoyancy Force}}\right|_{x=L} \propto \frac{q^2.L}{\rho_g.h_{fg}^2(\rho_f-\rho_g).g.D_h^2} \qquad 34$$

Now we can rewrite equation 34 in terms of the dimensionless numbers due to Silver, but based on D_h, provided we put the exit vapour dryness fraction, x^1, equal to unity in U, and we make the assumption that $\rho_f >> \rho_g$.

Thus:

$$\left.\frac{\text{Momentum Force}}{\text{Buoyancy Force}}\right|_{x=L} \propto \frac{N_e.N_s}{U} \qquad 35$$

As equation 35 represents a new force ratio for the annular geometry, we can define a new dimensionless parameter Y^*_g as follows

$$Y^{*2}_g = \frac{N_e.N_s}{U} \qquad 36$$

Y^*_g will attain a significance in annulus systems with evaporation when the vapour momentum increase force is significant.

Now we can combine equations 30 and 36 to obtain another significant dimensionless ratio as follows

$$\frac{J^{*2}_g}{Y^{*2}_g} = N_s \propto \left. \frac{\text{Inner Shear Force}}{f_i \cdot \text{Momentum Force}} \right|_{x = L} \qquad 37$$

We can therefore conclude that for annular systems in which buoyancy, momentum and shear forces are important at the critical heat flux condition, that the critical heat flux results will, at least, be dependant on any two of the following three dimensionless parameters: J^*_g, Y^*_g, N_s and upon the inner interfacial friction factor, f_i. J^*_g, Y^*_g and N_s are, of course, based on the annulus heated equivalent diameter, D_h.

16.6.0 SEPARATED FLOW MODEL APPLIED TO THE ANNULUS GEOMETRY

16.6.1 Introduction

The following theory was undertaken by the author, to determine the major parameters upon which the limiting heat flux might depend, for counter-current flow, for the annular geometry with both saturated and subcooled liquid entry. For the following analysis we shall assume the flow pattern to be annular. By experimental observation this is a reasonable assumption to make for most of the annuli tested. The observed flow pattern was not annular however for annuli with very large flow areas or for annuli with very small flow areas.

16.6.2 Saturated Liquid Entry Conditions

In this section we shall develop the separated flow model for the situation of saturated liquid entry to the annulus. Initially then we will focus our attention on the vapour core.

16.6.2.1 Vapour core

In the following analysis the following general assumptions will be made:

(a) one dimensional flow

(b) vapour contains no 'Ultra' heated water (see Silver (10))

(c) the water films occupy a negligible volume

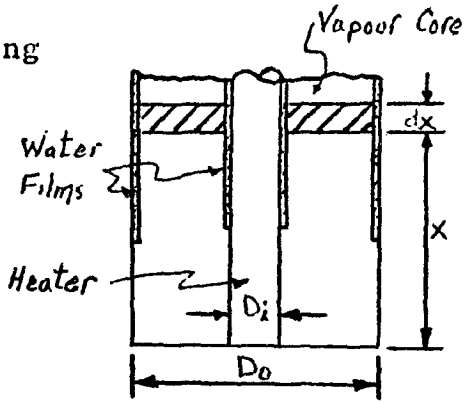

Annulus Assembly

We will now, by an energy balance, determine the vapour velocity increase across the control volume (shown in shaded in the diagram)

$$\therefore \quad q.\pi.D_i.dx = \rho_g.\frac{\pi}{4}(D_o^2-D_i^2).dV.h_{fg} \qquad 38$$

where dV represents the vapour velocity increase across the control volume. From equation 38 the rate of vapour velocity increase with 'x' the distance up the annulus is given by

$$\frac{dV}{dx} = \frac{4.q}{\rho_g.h_{fg}.D_h} \qquad 39$$

Now the vapour velocity at any distance 'x' up from the start of heating is given by integrating equation 39 as follows

$$\int_o^V dV = \frac{4.q}{\rho_g.h_{fg}.D_h}\int_o^X dX \qquad 40$$

$$\therefore V = \frac{4.q.x}{\rho_g.h_{fg}.D_h} \qquad 41$$

Equation 41 gives us an expression for the vapour velocity at any height up the annulus. Now the major forces acting on the vapour within the control volume are those due to interfacial shear, pressure, gravity, and inertia. A momentum balance across the control volume produces the following equation

$$-(p+dp)\frac{\pi}{4}(D_o^2-D_i^2)+p\frac{\pi}{4}(D_o^2-D_i^2)-(\tau_o.\pi.D_o+\tau_i\pi.D_i)dx-\frac{\pi}{4}(D_o^2-D_i^2)\rho_g.g.dx$$

$$= \rho_g.\frac{\pi}{4}(D_o^2-D_i^2)(V+dV)^2 - \rho_g.\frac{\pi}{4}(D_o^2-D_i^2)V^2 \qquad 42$$

We have assumed in formulating equation 42 that the evaporated molecules leave the water film with zero axial velocity and are completely accelerated within the vapour. Simplification of equation 42 thus produces the following form for the vapour momentum equation

$$-\frac{dp}{dx} - \rho_g.g. = \rho_g.2V.\frac{dV}{dx} + \frac{4.\tau_i}{D_h}\left(1 + \frac{\tau_o}{\tau_i}\frac{D_o}{D_i}\right) \qquad 43$$

Now assuming that the inner interfacial shear stress, τ_i, can be expressed in terms of an interfacial friction factor, f_i, in a similar manner to that assumed for single phase pipe flow then τ_i can be written as

$$\tau_i = \tfrac{1}{2} f_i.\rho_g.V^2 \qquad 44$$

and substitution of equation 44 into equation 43 gives for the vapour momentum equation

$$-\frac{dp}{dx} - \rho_g.g = \rho_g.2V.\frac{dV}{dX} + \frac{2.f_i.\rho_g.V^2}{D_h}\left(1 + \frac{\tau_o}{\tau_i}\frac{D_o}{D_i}\right) \qquad 45$$

Now we can put equation 45 in terms of the annulus central heater heat flux, q, by substituting into equation 45 for V and $\frac{dV}{dX}$ from equations 41 and 39. The resulting form of the vapour momentum equation is thus as follows

$$-\frac{dp}{dx} - \rho_g.g = \frac{32.q^2.x}{\rho_g.h_{fg}^2.D_h^2} + \frac{32.f_i.q^2.x^2}{\rho_g.h_{fg}^2.D_h.D_h^2}\left(1 + \frac{\tau_o}{\tau_i}\frac{D_o}{D_i}\right) \qquad 46$$

For saturated water entry conditions the vapour velocity is a maximum at x = L, that is, at the annulus mouth. Therefor the vapour acceleration forces and the shear forces will be a maximum at this position. It therefore follows that the required vapour driving pressure gradient as given by equation 46 will be a maximum at this position (x = L) also. We will therefore assume that the critical condition that determines the heater water film breakdown is determined by conditions at x = L for the saturated water entry condition. This assumption tends to be reinforced by the observed facts that for saturated water entry the heater water film destruction occurred mostly at or near the annulus mouth and that as the pool water subcooling increased so the water film destruction position

tended to move further down into the annulus. For high subcoolings the critical position occurred as much as two thirds of the way down into the annulus. Therefore putting $x = L$ into equation 46 and giving $\frac{dp}{dx}$ the subscript "R" to signify that it is a 'required' pressure gradient to remove the vapour from the annulus mouth then we can write equation 46, after substituting for N_s, as

$$-\left.\frac{dp}{dx}\right|_R - \rho_g.g = \frac{32.q^2.L^2}{\rho_g.h_{fg}^2.D_h.D_h^2}\left[\frac{1}{N_s} + f_i\left(1+\frac{\tau_o}{\tau_i}.\frac{D_o}{D_i}\right)\right] \qquad 47$$

Equation 47 can be further simplified by substituting for N_e, and N_s again, both of these dimensionless numbers being based, of course, on the heated equivalent diameter for the annulus, D_h.

$$-\left.\frac{dp}{dx}\right|_R = \rho_g.g\left[1 + 16.N_e.N_s^2\left(\frac{1}{N_s} + f_i\left(1 + \frac{\tau_o}{\tau_i}\frac{D_o}{D_i}\right)\right)\right] \qquad 48$$

Now if we neglect the weight of the vapour since this item is responsible for only a very small fraction of the total required pressure gradient, and put $U = \rho_f/\rho_g$ by making the assumptions, $x^1 = 1.0$ and $\rho_f >> \rho_g$ then equation 48 becomes

$$-\left.\frac{dp}{dx}\right|_R = 16.\rho_f.g.\frac{N_e.N_s^2}{U}\left[\frac{1}{N_s} + f_i\left(1 + \frac{\tau_o}{\tau_i}\frac{D_o}{D_i}\right)\right] \qquad 49$$

Finally by combining equations 30 and 49 we obtain the required pressure gradient in terms of the dimensionless parameter, J_g^*, as follows

$$-\left.\frac{dp}{dx}\right|_R = 16.\rho_f.g.J_g^{*2}\left[\left(\frac{1}{N_s} + f_i\left(1 + \frac{\tau_o}{\tau_i}\frac{D_o}{D_i}\right)\right)\right] \qquad 50$$

Now equation 50 gives us an expression for the axial pressure gradient required at the annulus mouth to supply the vapour acceleration force and to overcome the vapour frictional or shear forces.

In the next section we will consider the heater liquid film in order to determine the pressure gradient available at the annulus mouth to remove the vapour from the annulus.

16.6.2.2 Heater liquid film

Now consider the heater water film control volume shown shaded in the adjacent diagram. If we assume that the water momentum change across the control volume is negligible, then a force balance across the control volume gives us, assuming that the heater diameter, D_i, is much greater than the film thickness, δ_i,:

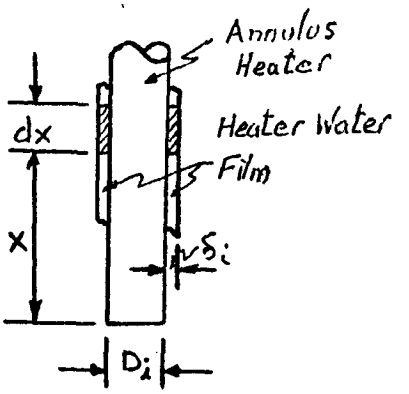

Annulus Heater

$$-(p+dp).\pi.D_i.\delta_i + p.\pi.D_i.\delta_i - \pi.D_i.\delta_i.dx\rho_f.g + \tau_i.\pi.D_i.dx + \tau_w.\pi.D_i.dx = 0 \quad 51$$

simplification of equation 51 gives us

$$-\frac{dp}{dx} = \rho_f.g - \frac{1}{\delta_i}(\tau_i + \tau_w) \quad 52$$

If we assume that the variables in equation 52 apply at the annulus mouth then the pressure gradient $\frac{dp}{dx}$ can be given the subscript "A" to signify that it is the available pressure gradient at the annulus mouth to remove the vapour from the annulus mouth. Thus equation 52 becomes

$$-\left.\frac{dp}{dx}\right|_A = \rho_f.g\left[1 - \frac{1}{\rho_f.g}\left(\frac{\tau_i+\tau_w}{\delta_i}\right)\right] \quad 53$$

We will now consider how the available pressure gradient, $\left.\frac{dp}{dx}\right|_A$, varies with the dimensionless gas velocity for the annulus, J^*_g.

16.6.2.3 Variation of $\left.\frac{dp}{dx}\right|_A$ with J^*_g

Now when J^*_g, the dimensionless vapour velocity is zero, that is, there is no vapour production in the annulus, then the pressure gradient made available by the system is zero. This is so because in film flow without evaporation all the hydrostatic head is balanced by the wall shear stress and the

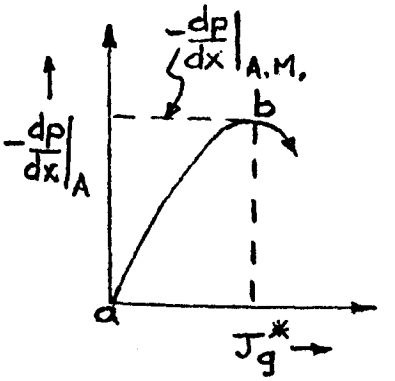

pressure outside the film is constant.

As we increase, J^*_g, the dimensionless vapour velocity, so a pressure gradient becomes necessary to drive the vapour produced from the system. This pressure gradient is achieved by the film flow being reduced and thus the wall shear stress becoming smaller. The pressure gradient now supplies the imbalance between the liquid weight and the wall shear force - assuming that the interfacial shear stress between the liquid film surface and the vapour is still negligible. Thus the system "makes available" the required pressure gradient. This process continues with an increasing pressure gradient available as J^*_g is increased until a situation is reached when the increase in the interfacial shear stress just equals the decrease in the wall shear stress and thus the available driving pressure gradient has reached its maximum value - see diagram, point 'b'. From here on the available pressure gradient falls because the interfacial shear stress rises faster than the wall shear stress falls. However as J^*_g passes point 'b' (see diagram) the increased vapour production requires a higher pressure gradient for its removal from the annulus. The system however is only capable of supplying a smaller pressure gradient and thus it becomes unstable.

16.6.2.4 Assumed critical condition

We will therefore assume that the critical heat flux occurs when, at the annulus mouth, the pressure gradient that is required for vapour removal, $\left.\frac{dp}{dx}\right|_R$ equals the "available maximum" driving pressure gradient, $\left.\frac{dp}{dx}\right|_{A.M.}$, that is

$$\left.\frac{dp}{dx}\right|_R = \left.\frac{dp}{dx}\right|_{A.M.} \qquad 54$$

We will now use the critical condition that we have defined in equation 54 to determine the maximum value for the dimensionless vapour velocity parameter, J^*_g, for various different physical situations.

16.6.2.5 Maximum J^*_g for negligible friction forces

For this situation when the vapour acceleration forces dominate, that is, when the friction forces can be considered zero then equation 50 which defines the "required" pressure gradient reduces to

$$-\left.\frac{dp}{dx}\right|_R = \frac{16.\rho_f.g.J^{*2}_g}{N_s} \qquad 55$$

and equation 53 which defines the "available" pressure gradient reduces to

$$-\left.\frac{dp}{dx}\right|_A = \rho_f.g = -\left.\frac{dp}{dx}\right|_{A.M.} \qquad 56$$

that is, for zero friction, the "available maximum" driving pressure gradient is equal to the hydrostatic pressure gradient.

Therefore if we substitute equations 55 and 56 into equation 54, which defines the condition for the critical heat flux to be attained, then we obtain for the maximum or limiting value of J^*_g

$$J^*_g = \frac{N_s^{\frac{1}{2}}}{4} \qquad 57$$

Now it is interesting to note that equation 57 can be rearranged in terms of the dimensionless parameter Y^*_g as defined by equation 36, as follows

$$\frac{J^*_g}{N_s^{\frac{1}{2}}} = Y^*_g = \frac{1}{4} \qquad 58$$

Reference to equation 35 indicates that Y^{*2}_g is proportional to the ratio of the vapour momentum force to the buoyancy force at the annulus exit. The critical situation therefore as defined by equations 57 or 58 is determined, as would be expected for this situation in which friction forces are neglected, by a balance between the vapour momentum force and buoyancy force only.

We will now determine the maximum or limiting value of J^*_g when only the friction effects on the water films are neglected.

16.6.2.6 Maximum J^*_g neglecting friction effects on water films only

For this situation both the acceleration and frictional

forces are considered to act on the vapour and therefore the "required" pressure gradient to drive the vapour out at the annulus mouth is given by equation 50. Since friction forces are considered to be absent from the water film, then the "available maximum" pressure gradient is the hydrostatic pressure gradient as given by equation 56. Therefore if we substitute equations 50 and 56 into the equation that defines the critical situation, that is equation 54, then we get

$$16.\rho_f.g.J_g^{*2}\left[\frac{1}{N_s} + f_i\left(1 + \frac{\tau_o}{\tau_i}.\frac{D_o}{D_i}\right)\right] = \rho_f.g \qquad 59$$

from which we obtain the maximum or limiting value of J_g^* as

$$J_g^* = \frac{N_s^{\frac{1}{2}}}{4}\left[\frac{1}{1 + f_i.N_s\left(1 + \frac{\tau_o}{\tau_i}.\frac{D_o}{D_i}\right)}\right]^{\frac{1}{2}} \qquad 60$$

If we now compare equation 60 to equation 57 it is seen that the addition of the friction effects on the vapour core is to reduce the maximum or limiting value of J_g^* as would be expected.

We will now determine the maximum value of J_g^* when all friction effects are included.

16.6.2.7 Maximum J_g^* including all friction effects

For this situation both the acceleration and frictional forces are considered to act on the vapour core and therefore the "required" pressure gradient is as given by equation 50.

Since friction forces are considered to be present on the water film, then the "available maximum" pressure gradient is given by equation 53. Therefore if we substitute equations 50 and 53 into the equation that defines the critical situation, that is equation 54, then we get

$$16.J_g^{*2}\left[\frac{1}{N_s} + f_i\left(1 + \frac{\tau_o}{\tau_i}.\frac{D_o}{D_i}\right)\right] = \left[1 - \frac{1}{\rho_f.g}\left(\frac{\tau_i + \tau_w}{\delta_i}\right)\right]_{A.M.} \qquad 61$$

where the subscript A.M. stands for "available maximum". Now we can obtain the maximum value of J_g^*, the dimensionless vapour velocity, from equation 61 as follows:

$$J^*_g = \frac{1}{4}\left[\frac{\left\{1 - \frac{1}{\rho_f . g}\left\{\frac{(\tau_i + \tau_w)}{\delta_i}\right\}\right\}_{A.M.}}{\frac{1}{N_s} + f_i\ (1 + \frac{\tau_o}{\tau_i}.\frac{D_o}{D_i})}\right]^{\frac{1}{2}} \qquad 62$$

or

$$J^*_g = \frac{N_s^{\frac{1}{2}}}{4}\left[\frac{\left\{1 - \frac{1}{\rho_f . g}\left\{\frac{\tau_i + \tau_w}{\delta_i}\right\}\right\}_{A.M.}}{1 + f_i . N_s\ (1 + \frac{\tau_o}{\tau_i}.\frac{D_o}{D_i})}\right]^{\frac{1}{2}} \qquad 63$$

If we now compare equation 63 to equation 60 it is seen that the inclusion of the film friction has further reduced the maximum value of J^*_g, the dimensionless vapour velocity.

We will now determine the maximum value of J^*_g for the situation when the vapour acceleration forces are excluded but all the friction effects are included.

16.6.2.8 Maximum J^*_g including all friction forces but excluding vapour acceleration forces

For this situation, in which we neglect the force required to increase the vapour momentum, then equation 50, the "required" pressure gradient equation, is reduced to:

$$-\left.\frac{dp}{dx}\right|_R = 16 . \rho_f . g . J^{*2}_g . f_i\ (1 + \frac{\tau_o}{\tau_i} . \frac{D_o}{D_i}) \qquad 64$$

That this is so can be seen by reference to equation 37 which shows that for annular systems in which both shear and vapour momentum forces are important that $\frac{J^{*2}_g}{N_s}$ equals Y^{*2}_g, the ratio of the vapour momentum force to the buoyancy force at x = L. Thus for zero vapour momentum force then Y^*_g equals zero and therefore equation 50 reduces to the form given above as equation 64.

Now the "available maximum" pressure gradient is obtained from equation 53 with the suffix A.M. representing the "available maximum", as

$$-\left.\frac{dp}{dx}\right|_{A.M.} = \rho_f . g\left[1 - \frac{1}{\rho_f . g}\left\{\frac{\tau_i + \tau_o}{\delta_i}\right\}\right]_{A.M.} \qquad 65$$

Therefore putting equations 64 and 65 into equation 54, the equation that defines the critical situation, then we get for the maximum value of J^*:

$$J_g^* = \frac{1}{4}\left[\frac{\left\{1 - \frac{1}{\rho_f g}\left\{\frac{\tau_i + \tau_w}{\delta_i}\right\}\right\}_{A.M.}}{f_i\left(1 + \frac{\tau_o}{\tau_i}\cdot\frac{D_o}{D_i}\right)}\right]^{1/2} \qquad 66$$

which becomes after defining B, and Dp as follows:

$$B = \frac{1}{\rho_f \cdot g}\left(\frac{\tau_i + \tau_w}{\delta_i}\right) \qquad 67$$

$$\text{and} \quad Dp = f_i\left(1 + \frac{\tau_o}{\tau_i}\cdot\frac{D_o}{D_i}\right), \qquad 68$$

$$J_g^* = \frac{1}{4}\left[\frac{(1 - B)_{A.M.}}{Dp}\right]^{\frac{1}{2}} \qquad 69$$

If we therefore compare equations 66 or 69 to equation 62 it is seen that the effect of assuming that the vapour momentum increase is zero is to increase the maximum value of J_g^*, as would be expected.

We will now proceed to examine the effect, upon the critical heat flux, of the water entering the annulus in a subcooled condition.

16.6.3 Subcooled Liquid Entry Conditions

In this section we shall develop the separated flow model for the situation of subcooled liquid entry to the annulus.

Consider therefore the annular system shown in the adjacent diagram in which the vapour produced by heating from the central heater leaves the annulus top in counter flow to the subcooled water entering the system by film flow on the annular surfaces. Now as the subcooled water flows down the annulus its temperature will be

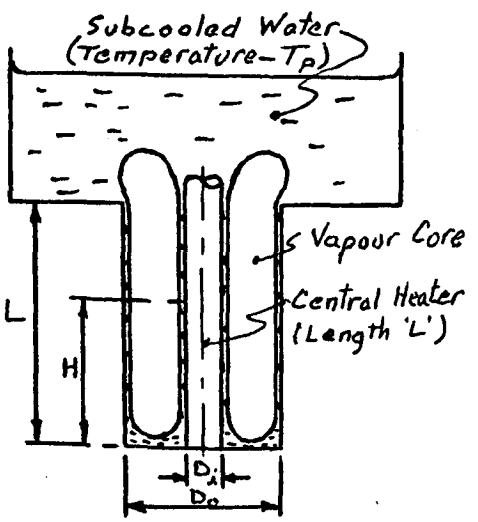

ANNULUS ASSEMBLY

increased until at some "effective" height "H" up the annulus the water can be considered to have just reached its saturation temperature. Therefore let the subcooled pool water temperature be T_p, and the water saturation temperature be T_s so that the pool subcooling, ΔT_s, is given by

$$\Delta T_s = (T_p - T_s) \qquad 70$$

Now if we assume that it is possible for some water to be recirculated, that is, water that enters the annulus in the subcooled state is heated up to the saturation temperature and then, not vaporised, but ejected from the annulus mouth as saturated water droplets then we can define a water recirculation parameter "n" as follows

$$n = \frac{m_f}{m_g} \qquad 71$$

Now when n = 1, then there is no water recirculation because $m_f = m_g$, therefore generally

$$m_f = n.m_g = n.\rho_g.A_F.V_g \qquad 72$$

and if we neglect the flow area occupied by the water films then A_F, the vapour flow area, is given by

$$A_F = \frac{\pi}{4}(D_o^2 - D_i^2) \qquad 73$$

We will now determine the "effective" distance from the annulus entry to the position where the water films reach saturation temperature, that is (L - H). Now an energy balance over this distance gives us

$$q.\pi.D_i\ (L - H) = n.m_g.C_{pf}.\Delta T_s \qquad 74$$

Now the maximum vapour velocity, V_g, that occurs at the position defined by "H" is given by equation 41 with "x" replaced by "H" as

$$V_g = \frac{4.q.H}{\rho_g.h_{fg}.D_h} \qquad 75$$

The implicit assumption, that we have made, that the maximum vapour velocity, for subcooled water entry, occurs at "H" implies that vapour condensation occurs above H to the subcooled water films. This assumption suggests that with subcooled water entry the critical position within the annulus

should move down the annulus with increased subcooling. This tendency was in fact observed during the experimental programme.

Substitution of equations 72, 73 and 75 into equation 74 gives for (L - H).

$$(L - H) = \frac{n.\rho_g . \frac{\pi}{4} (D_o^2 - D_i^2).4.q.H.C_{pf}.\Delta T_s}{q.\pi.D_i.\rho_g.h_{fg}.D_h} \qquad 76$$

from which we obtain the relationship

$$\frac{L}{H} = 1 + \frac{n.C_{pf}}{h_{fg}} . \Delta T_s \qquad 77$$

Now all the previous relationships developed for the annulus saturated entry conditions apply also to this subcooled entry situation provided that "L" is replaced by "H" and the heat flux "q" is replaced by "q_s", the critical heat flux for the subcooled entry situation.

Therefore rewriting equation 62 which applies, of course, for saturated entry conditions, using the definitions of B and D_p as given by equations 67 and 68 we obtain

$$J^*_g = \frac{1}{4} \left[\frac{(1 - B)_{A.M.}}{\frac{1}{N_s} + D_p} \right]^{\frac{1}{2}} \qquad 78$$

Now if we modify equation 78 so that it applies to the subcooled entry situation we obtain

$$J^*_g . \frac{q_s}{q} . \frac{H}{L} = \frac{1}{4} \left[\frac{(1 - B)_{A.M.}}{\frac{1}{N_s} . \frac{L}{H} + D_p} \right]^{\frac{1}{2}} \qquad 79$$

and defining J^*_{gs}, the limiting dimensionless vapour velocity for the subcooled water entry situation by

$$J^*_{gs} = J^*_g . \frac{q_s}{q} \qquad 80$$

then we obtain the relationship between the limiting dimensionless vapour velocities and the limiting heat fluxes for the two situations, as follows

$$\frac{J^*_{gs}}{J^*_g} = \frac{q_s}{q} \qquad 81$$

We can now obtain a general expression for J^*_{gs} by putting equations 80 and 77 into equation 79 to obtain the following relationship

$$J^*_{gs} = \frac{1}{4}\left[\frac{(1 - B)_{A.M.}}{\frac{1}{N_s}\cdot\frac{L}{H} + D_p}\right]^{\frac{1}{2}}\left[1 + \frac{n.C_{pf}}{h_{fg}}.\Delta T_s\right] \qquad 82$$

We will now determine the form of equation 82 when all friction forces are neglected.

16.6.3.1 Maximum J^*_{gs} for negligible friction forces

For this situation in which all friction forces are negligible then the parameters B and D_p in equation 82 both become zero and therefore after substituting in equation 82 for $\frac{L}{H}$ from equation 77, J^*_{gs} for this situation becomes

$$J^*_{gs} = \frac{N_s^{\frac{1}{2}}}{4}\left[1 + \frac{n.C_{pf}.\Delta T_s}{h_{fg}}\right]^{\frac{1}{2}} \qquad 83$$

Since for saturated water entry to the annulus with negligible friction forces we have, from equation 57 that

$$J^*_g = \frac{N_s^{\frac{1}{2}}}{4} \qquad 84$$

then putting equation 84 into equation 83 and combining the result with equation 81 we obtain the final form of equation 83 as

$$\frac{J^*_{gs}}{J_g} = \frac{q_s}{q} = \left[1 + \frac{n.C_{pf}}{h_{fg}}.\Delta T_s\right]^{\frac{1}{2}} \qquad 85$$

Now equation 85 relates the subcooled water entry critical heat flux, q_s, to the corresponding saturated water entry critical heat flux, q, for the situation in which all friction forces have been neglected.

We will now determine the form of equation 82 for the situation in which the vapour momentum increase force is neglected.

16.6.3.2 Maximum J^*_{gs} for negligible acceleration forces

For this situation when friction forces dominate then

equation 82 reduces to the following form

$$J^*_{gs} = \frac{1}{4}\left[\frac{(1 - B)_{A.M.}}{D_p}\right]^{\frac{1}{2}}\left[1 + \frac{n.C_{pf}}{h_{fg}} .\Delta T_s\right] \quad 86$$

Since for saturated water entry to the annulus with negligible vapour acceleration forces we have from equation 69 that

$$J^*_g = \frac{1}{4}\left[\frac{(1 - B)_{A.M.}}{D_p}\right]^{\frac{1}{2}} \quad 87$$

then putting equation 87 into equation 86 and combining the result with equation 81 we obtain the final form of equation 86 as

$$\frac{J^*_{gs}}{J^*_g} = \frac{q_s}{q} = 1 + \frac{n.C_{pf}}{h_{fg}}.\Delta T_s \quad 88$$

On rearrangement we obtain the following form for equation 88

$$\left[\frac{J^*_{gs}}{J^*_g} - 1\right]\frac{1}{\Delta T_s} = \left[\frac{q_s}{q} - 1\right]\frac{1}{\Delta T_s} = \frac{n.C_{pf}}{h_{fg}} \quad 89$$

We will now examine equation 84 for the situation in which the liquid recirculation is zero, that is n = 1.0.

16.6.3.3 Zero liquid recirculation

For this situation of zero liquid recirculation, that is, when the parameter "n" is unity then equation 89 reduces to

$$\left[\frac{q_s}{q} - 1\right]\frac{1}{\Delta T_s} = \frac{C_{pf}}{h_{fg}} \quad 90$$

Now the ratio $\frac{C_{pf}}{h_{fg}}$ is approximately constant over the pressure range investigated experimentally (760 torr. to 160 torr.) and has a value of $1.8 \times 10^{-3}/^{o}C$. Fig. 17 indicates how little this parameter varies over the pressure range investigated. It therefore follows that, for this situation, in which the water recirculation parameter tends to unity then the parameter $\left[\frac{q_s}{q} - 1\right].\Delta T_s^{-1}$ should tend to the constant value of $1.8 \times 10^{-3}/^{o}C$.

17.0.0.

D E S C R I P T I O N O F E X P E R I M E N T

DESCRIPTION OF EXPERIMENT

17.1.0 Experimental Rig

The two phase flow heat transfer rig is shown diagrammatically in Fig. 1 and photographically in Fig. 2. It consists of a spherically bottomed glass boiling cell 30 cm in diameter and 37 cm high which contains the distilled water (conductivity $< 2.5 \mu$mho), the glass-heater annulus assembly (see Fig. 5), Aluminium conductors, Aluminium cooling and condenser coils, a stirrer, a separate stainless steel heater coil, and stainless steel sheathed, MO_2 insulated, Ch.-Al. thermocouples. All these items were mounted (Fig. 3 and 4) via a stainless steel, Teflon lined, Tufnol top which formed the vacuum seal to the boiling cell. There were also connections to the vacuum system pumping unit and a Mercury manometer.

The electrical power supply to the annulus assembly heater was obtained from an autotransformer-rectifier set which was capable of delivering up to 2000 amp D.C. at 12 Volts. The power variation was continuous, was controlled remotely at the experiment, and could be tripped by a hand operated trip switch mounted at the experiment. To determine the power dissipated in the heater the current and heater voltage drop were measured, using a variable scale, dual channel pen recorder. To determine the heater current the voltage drop across an accurately calibrated shunt was used to drive one channel of the pen recorder. The heater voltage drop was taken from tappings at either end of the heater and recorded on the second channel of the pen recorder. The ability to change scales on the pen recorders allowed heaters of largely differing cross sections to be easily accommodated.

Vacuum was produced in the boiling cell by means of two water jet pumps working in parallel and driven by a centrifugal pump. This system was cheap and eliminated the possibility of contaminants entering the boiling cell from the vacuum system. Rig vacuum was determined by Mercury Manometer inconjunction with a Barometer.

The pool temperature was determined by two Ch.-Al. thermo-

couples (using an ice point cold junction) mounted 3 cm. above the annulus/heater tube top and 8 cm to each side of the heater. The outputs from these thermocouples were taken, through a rotary switch, to a digital voltmeter capable of a resolution of one microvolt.

The electrical supply to the separate one Kilowatt stainless steel water heater was taken from the normal 230 Volt A.C. supply via. an autotransformer that reduced the voltage to 120 Volts.

17.2.0 Annulus Assembly

A typical annulus-heater assembly is shown diagrammatically on Fig. 5. It consists of a vertical stainless steel cylindrical heater surrounded by an inner glass tube that forms the outer wall of the annulus. This glass tube is centralised with respect to the heater by a rubber water tight seal mounted at the base of the heater. Mounted around the inner glass tube was an outer glass tube which formed a small annular air gap, which acted as a heat shield around the annulus, the air to water seals being made with Neoprene 'O' rings. This heat shield was, of course, only of use for the subcooled water entry tests. Heater working lengths were normally 12.4 cm although one heater used had a working length of 13 cm. Details of a typical heater design are given in Fig. 5. Stainless steel heater tubes of three different diameters were used as follows:

a) 9.53 m.m. O.D. by 0.915 m.m. wall by 12.4 cm working length
b) 6.35 m.m. O.D. by 0.915 m.m. wall by 12.4 cm working length
c) 3.15 m.m. O.D. by 0.79 m.m. wall by 12.4 cm working length
d) 3.15 m.m. O.D. by 0.79 m.m. wall by 13.0 cm working length

A range of glass surrounds were used inconjunction with the specimen enumerated above to give a variation of the annuli inner and outer diameters. For a complete list of the annuli outer diameters see "D_o" on Figs. 27, 28, 29, 30.

Heater voltage drop taps were taken from small screws mounted in the heater Brass end pieces. For all specimen

the error in the voltage measurement, caused by not having the voltage taps exactly at each end of the heater working length, was determined by separate heater calibration tests. In these tests a monitored current was passed through the heater and voltage drop measurements made, using a digital voltmeter, across the voltage tappings and then across the specimen working length. From these readings the voltage difference was determined and was always less than 4%. Correction factors were applied accordingly.

The heat transfer area was then calculated for the heater and combined with the voltage correction factor to enable the specimen heat flux to be determined directly from the current and voltage measurements made during actual testing.

17.3.0 Boiling Cell Assembly

Before the annulus assembly was undertaken the heater was rubbed clean in a random manner with a fine emery cloth and then thoroughly washed in acetone. The wettability of the heater surface was tested by running water from a tap along its surface. With experience it was possible, by this technique, to confirm that the heater surface was completely wettable. The heater was then rinsed in Acetone, dried, and assembled centrally within the glass surround that formed the outer wall of the annulus. Care was taken that the annulus bottom seal was water tight and that the glass surround top was just level with the top of the heater working length. This annulus assembly was then connected across the rig electrical input conductors, care being taken to ensure that the heater was vertical and that the annulus gap was uniform around the heater.

The glass vessel was filled with distilled water whose conductivity was normally less than 1.5 μmho. and never greater than 2.5 μmho and the boiling cell inner assembly lowered into place and finally bolted into position. Electrical power, cooling water supply, vacuum, thermocouple and instrument connections were then made to complete the assembly. The distilled water level was set approximately 13 cm. above the annulus mouth.

17.4.0 Experimental Technique

Initially the rig water was boiled under vacuum for approximately ten minutes to check out the whole system and to remove most of the air from the water. The author found that the presence of air in small quantities did not affect the experimental results. Normally near the completion of the testing of a particular annulus assembly when check points were being obtained no air bubbles were visible at all and the water appeared to be effectively degassed. Experimental results obtained under these conditions always confirmed those obtained at the start of testing when small air bubbles were present in small numbers.

A typical annulus test series will now be described in which limiting heat fluxes were obtained for both saturated entry and subcooled entry to the annulus over the entire vacuum range.

For the subcooled water entry tests, the vessel water was brought to the required temperature by the rig heater/cooler, and the system vacuum set to the required value. Fine control of the system vacuum under testing was achieved by means of an adjustable leak into the vacuum pump extract line. The power to the annulus heater was then increased in steps until it was generating a heat flux at approximately 80% of the critical value. It is worth noting here that under high vacuum the initial nucleation within the annulus was explosive in nature.

After the system had run for approximately five minutes at approximately 80% of its critical heat flux the pool water was agitated to bring it to a uniform temperature throughout. The heater power was then increased by small increments until finally the critical condition was attained. For large annuli this condition was detected visually by the heater starting to glow red hot locally. For smaller annuli the condition was detected from the heater current and voltage drop traces on the dual channel recorder as follows: at the critical condition as the heater temperature rises because of local liquid starv-

ation, so its electrical resistance increases, the pen recorders therefore indicate simultaneously a falling current and an increasing heater voltage drop. By this method, for the smaller annuli, it was possible to detect the critical condition before the specimen was red hot locally. The system vacuum was then noted, the heater power supply tripped, the pool water temperature recorded, and the heater current and voltage drop noted from the pen recorder charts. It was also possible, in most instances, by observation of the water film front advancing down the heater, after the power trip, to see "sputtering" (see (9)) occurring at the film front until finally the heater surface was completely rewetted.

Further points with subcooled entry were then obtained in a similar manner, by raising the pool temperature to the required value and resetting the system vacuum as required.

To obtain results for the saturation line (see Fig. 9) the power to the annulus heater was again raised to approximately 80% of the estimated critical value. The pool water was then agitated to ensure that it was at a uniform temperature throughout, and the system vacuum increased until the pool temperature corresponded with the saturation temperature for the system pressure. The heater power was then increased in small steps until the critical condition was attained - observed in a similar manner to that described for subcooled entry. The system vacuum was then noted, the heater power supply tripped, the pool water temperature recorded, and the heater current and voltage drop noted from the pen recorder charts. Further results for higher pool temperatures up to 100°C were attained in a similar manner.

To obtain a complete set of results for one annulus (see Fig. 9) the tests would start at a low pool temperature and subcooled entry results obtained at the different system vacuums tested. As the pool temperature was increased above the saturation temperature corresponding to approximately 150 torr. pressure then results were also obtained for saturated entry conditions. This procedure was continued until the

pool temperature reached the saturation temperature corresponding to atmospheric pressure and the complete picture (Fig. 9) had been obtained. Check results were then taken for both saturated and subcooled entry, at atmospheric pressure and under vacuum conditions, as the pool water was cooled.

For saturated entry conditions the liquid-vapour flow, except for the very narrow and the very large annuli, was of an annular nature with a continuous vapour bubble at the annulus mouth. However this bubble slightly reduced its size, regularly to allow an increased inflow of water which then enabled the bubble to regenerate itself and thus rethrottle the annulus water inflow. A visually similar situation applied to the subcooled entry situation except that the bubble size at the annulus mouth was progressively reduced with increased subcooling.

A series of annuli were tested in which both the annulus outside, and inside diameter were systematically varied. A further test over the complete vacuum and subcooling range was carried out using the vertically mounted 3.15 cm. O.D. by 12.4 cm long specimen with no confinement, except of course for the boiling cell. This constituted the vertical pool boiling situation which is an upper limiting case for the confined annular geometry. The results obtained are shown on Fig. 8. After each geometry had been completely tested the boiling cell was refilled with a new charge of distilled water.

Fig. 6 shows an assembly, with a small annular gap, boiling at a heat flux of approximately 75% of the critical value. Fig. 7 shows the same assembly boiling with the heater flux having just attained the critical value. The heater "dry" section is shown having formed in the bottom half of the test section.

18.0.0.

R E S U L T S

RESULTS

18.1.0 General

In all, twenty one different annuli were tested at atmospheric pressure and under vacuum conditions for saturated water entry, and for subcooled water entry. Both the annuli inside and outside diameters were varied.

Basic experimental data together with the refined results calculated from this data are presented in tabular form in Figs. 27 to 34 inclusive. Figs. 27 to 30 apply to the saturated water entry situation while Figs. 31 to 34 apply to the subcooled water entry situation. Results for 20°C, 30°C, 40°C and 50°C of subcooling are given.

Three complete sets of results are shown graphically on Figs. 8, 9 and 10. Fig. 8 presents the results obtained when the 3.15 m.m. O.Dia. specimen was tested under vertical pool boiling conditions. Figs. 9 and 10 present similar results for the annular geometry situation. The results presented on Fig. 9 apply to an annulus with a "large" annular gap, while those presented on Fig. 10 apply to an annulus with a "small" annular gap. Comparison of Figs. 9 and 10 indicates that water subcooling at the annulus mouth has a large effect on the critical heat flux in the former situation while in the latter situation the effect is small. This effect is probably caused by an appropriate variation in the liquid recirculation.

18.2.0 Saturated Water Entry

Fig. 11 shows a plot of the dimensionless vapour velocity, J^*_g, against the inverse annulus number, N_a^{-1}, for all annuli tested at a system pressure of 760 torr. Reference to Fig. 11 indicates that there is still a dependence on the annulus inside diameter, D_i, that is not included in the major parameters J^*_g and N_a.

Fig. 12 shows that the three individual lines of Fig. 11 have been reduced to one line, by introducing the liquid viscosity number, N_f, based on the annulus inside diameter. Now N_f contains the liquid viscosity, which is a function of the system pressure, and as will be seen later this dependence on

pressure allows the slight dependence of J^*_g on pressure to be correlated also by N_f.

Fig. 13 and 14 are similar plots to Fig. 12 but for system pressures of 360 torr. and 160 torr. respectively. The lines drawn through the points on Figs. 12, 13 and 14 are identical and thus indicate that the water viscosity dependence on pressure, represented by the viscosity number N_f, allows the correlation of the experimental results over the pressure range tested.

Fig. 15 is a plot using the same co-ordinates as in Figs. 12, 13 and 14 but containing all the experimental results plotted on Figs. 12 to 14 inclusive. It is seen that the vast majority of the points are contained within the $\pm$ 25% dotted lines shown about the full correlating line.

Fig. 16 is a plot obtained directly from Fig. 15 which shows explicitly how the critical heat flux varies for saturated water entry. Also shown are the "vertical" pool boiling critical heat flux values at 760 torr., 360 torr., and 160 torr. pressures obtained from the saturated boiling curve on Fig. 8. These values constitute upper limits to the annulus situation, that is, when the annulus outer surface can be considered to be at "infinity".

18.3.0 Subcooled Water Entry

The author has attempted to correlate the critical heat flux values for the subcooled entry situation relative to the corresponding saturated critical heat flux in a similar manner to that successfully used in the past for the pool boiling situation (eg. see eqn. 4, Part I).

Fig. 18 is a plot for a particular annulus of (a) the saturated liquid entry critical heat flux, (b) the 50°C subcooled liquid entry critical heat flux, and (c) the ratio of (b) to (a), against the annulus $\frac{L}{D_e}$ ratio. Reference to Fig. 18 shows that although both the subcooled and saturated critical heat flux curves increase monotonically with reducing $\frac{L}{D_e}$, their ratio does not, but follows the curve shown in chain

dotted on Fig. 18. This unexpected behaviour is caused by the different rates of increase of the two composite curves.

Figs. 19 and 20 show, for a system pressure of 760 torr., for all annuli tested, the heat flux ratios q_{50}/q, and q_{40}/q, plotted against $\frac{L}{D_e}$. Also shown on these figures are the "no recirculation" limits obtained by using equation 90, and the "vertical" pool boiling limits obtained from the results given on Fig. 8. It is seen that for large $\frac{L}{D_e}$ the curves tend towards the "no recirculation" limits while for small $\frac{L}{D_e}$ they tend towards the vertical pool boiling values. In between these two limits the curves follow the unexpected shape described previously when discussing Fig. 18.

Fig. 21 is a similar curve to those shown on Figs. 19 and 20 except that the operating pressure is 360 torr.

Figs. 22, 23 and 24 are plots of the subcooled heat flux parameter defined by equation 90 against $\frac{L}{D_e}$ for system pressures of 760 torr., 360 torr., and 160 torr. respectively. The key to the points plotted is given on each figure. The dotted lines on each figure represent the $\pm$ 25% band and it is seen that the vast majority of the points lie within this band.

Fig. 25 shows the correlating lines of Figs. 22, 23 and 24 superimposed. It is seen, for the pressure range covered, that the results tend to be independent of pressure for the range of $\frac{L}{D_e}$ greater than 10.

19.0.0.
COMPARISON OF RESULTS WITH MODELS

COMPARISON OF RESULTS WITH MODELS

19.1.0 Saturated Water Entry

19.1.1 Experimental correlation

The final correlation for the results obtained, for all annuli, for saturated water entry, over the complete pressure range is shown on Fig. 15. The bend in the correlating line at approximately $J^*_g = 0.02$ represents the situation when the results start to move away from the annulus correlation line ($J^*_g > 0.02$) towards the pool boiling limit. This situation is more clearly illustrated on Fig. 16.

For the range when pool boiling effects are absent ($J^*_g > 0.02$) reference to Fig. 15 shows that the slope of the line on the log-log plot (ordinate and abscissa scales equal) is negative and equal to 1.0. It therefore follows that for the range investigated $0.02 < J^*_g < 0.6$ then

$$J^*_g = A \left[\left(\frac{D_o^2 - D_i^2}{D_i^2} \right)^{0.83} . N_f^{0.47} \right]^{-1} \qquad 91$$

A = Constant

Substituting N_a for $\frac{D_i^2}{D_o^2 - D_i^2}$ then equation 91 becomes

$$J^*_g = A . N_a^{0.83} . N_f^{-0.47} \qquad 92$$

from Fig. 15 for $J^*_g = 1.0$, then $N_a^{0.83} . N_f^{-0.47} = \frac{1}{11.8}$

putting these values into equation 92 gives A = 11.8

∴ the experimental correlation for the "annulus" range is represented by the equation

$$J^*_g = 11.8 . N_a^{0.83} . N_f^{-0.47} \qquad 93$$

To compare this experimental correlation with the theory, then equation 93 will be modified as follows

Now

$$J^*_g = 11.8 \left[\frac{D_i^2}{D_o^2 - D_i^2} \right]^{0.83} \left[\frac{\nu_l}{D_i^{\frac{3}{2}} . g^{\frac{1}{2}}} \right]^{-0.47}$$

$$= 11.8 \left(\frac{L}{D_h}\right)^{0.83} \left(\frac{\nu_l}{L^{\frac{3}{2}}.g^{\frac{1}{2}}}\right)^{0.47} \left(\frac{D_i}{L}\right)^{0.125}$$

$$\therefore \quad J_g^* = 11.8\, N_s^{0.83} \cdot N_{fL}^{-0.47} \cdot \left(\frac{D_i}{L}\right)^{0.125} \qquad 94$$

For the experimental range investigated, "L" was constant, "g" was constant, and the variation in "ν_l" due to pressure variation was not large. The major variation occurred in N_s due to annulus diameter variations. Therefore to compare the experimental correlation with the theoretical results mean values will be calculated for $(N_{fL})^{-0.47}$ and for $\left\{\frac{D_i}{L}\right\}^{0.12}$ and thus J_g^* written in the form

$$J_g^* \doteq \text{Const.}\ N_s^{0.83} = C_1 . N_s^{0.83} \qquad 95$$

Comparison of equations 94 and 95 show that

$$C_1 = 11.8 . N_{fL}^{-0.47} \left(\frac{D_i}{L}\right)^{0.125} \qquad 96$$

Evaluation of $N_{fL}^{-0.47}$

$$\therefore \quad (N_{fL})^{-0.47} = \left(\frac{\nu_l}{L^{\frac{3}{2}}.g^{\frac{1}{2}}}\right)^{0.47} = \frac{\nu_l^{0.47}}{L^{0.705}.g^{0.235}} \qquad 97$$

Data

$L = 0.41$ ft, $g = 32.2$ ft/sec^2

$\nu_l = 0.33 \times 10^{-5}$ ft^2/sec at 760 torr

$\nu_l = 0.53 \times 10^{-5}$ ft^2/sec at 160 torr

Substitution of this data into equation 97 gives

$(N_{fL})^{-0.47} = 2.2 \times 10^{-3}$ at 760 torr

" $= 2.75 \times 10^{-3}$ at 160 torr

$\therefore$ Mean value over the pressure range 760 torr to 160 torr is 2.5×10^{-3} and the variation about this mean is approximately $\pm$ 10%

Evaluation of $\left\{\frac{D_i}{L}\right\}^{0.125}$ 98

Data

$L = 4.875$ in

D_i (maximum) $= 0.375$ in

D_i (minimum) $= 0.125$ in

Substitution of this data in equation 98 gives

$$\left\{\frac{D_i}{L}\right\}^{0.125} = \left(\frac{0.375}{4.875}\right)^{0.125} = 0.725 \text{ maximum}$$

$$= \left(\frac{0.125}{4.875}\right)^{0.125} = 0.634 \text{ minimum}$$

∴ Mean value over heater diameter range investigated is 0.68 and the variation about this mean is approximately ± 7%

Putting these mean values into equation 96 gives

$$C_1 = 11.8 \times 2.5 \times 10^{-3} \times 0.68 = 0.02 \pm 17\%$$

Using this value for C_1 in equation 95 gives

$$J^*_g = 0.02.N_s^{0.83} \qquad 99$$

Equation 99 is a very good approximate representation of the experimental correlation given by equation 93 and in this form can be readily compared with the theoretical predictions.

Defining 'Y' as $$Y = \frac{4.J^*_g}{N_s^{\frac{1}{2}}} = 4.Y^*_g \qquad 100$$

then eqn. 99 becomes $$Y = 0.08.N_s^{0.33} \qquad 101$$

19.1.2.0 Model Predictions

19.1.2.1 Negligible friction forces

The one dimensional separated flow type model used, in which void fraction effects have been neglected predicts the relationship (equation 57) for negligible friction forces:

$$J^*_g = \frac{N_s^{\frac{1}{2}}}{4} \qquad 102$$

Using the definition of 'Y' given by equation 100, equation 102 becomes

$$Y = 1.0 \qquad 103$$

Equation 103 is shown plotted on Fig. 26 together with the experimentally determined correlation (as defined by equation 101) over the experimental range investigated. Reference to this graph indicates that for $N_s \sim 1.0$ the experimental curve lies well below the theoretical model upper limit obtained by neglecting frictional effects. However as N_s increases so the distance between the two lines diminishes, which indicates that the vapour acceleration forces become more important as the parameter N_s increases, that is, the

annulus, annular gap becomes smaller. It is worthwhile noting here that the annulus heated length was held essentially constant throughout the experimental programme.

19.1.2.2 Negligible water film friction forces

For this situation the model prediction is given by equation 60 which when written in terms of the parameter 'Y' gives

$$Y = \left[\frac{1}{1 + f_i N_s \left(1 + \frac{\tau_o}{\tau_i} \cdot \frac{D_o}{D_i}\right)}\right]^{\frac{1}{2}} \qquad 104$$

Now it can be shown that for single phase gas flow in annuli without evaporation (see Appendix 1) that

$$\left(1 + \frac{\tau_o}{\tau_i} \cdot \frac{D_o}{D_i}\right) = \frac{\log_e \left(1 + \frac{1}{N_a}\right)}{1 - N_a \log_e \left(1 + \frac{1}{N_a}\right)} \qquad 105$$

Therefore using equation 105 as an approximation to the present situation, together with a value of the interfacial friction factor, f_i, of 0.02 (the value applicable to very rough pipes in single phase flow) then equation 104 can be evaluated for the present situation. This evaluation has been made, over the experimental range applicable, and is shown as the curve, marked A = 1 on Fig. 26. Reference to Fig. 26 indicates that the major effect occurs in the region of large N_s. The major unknowns are, the interfacial friction factor and how this varies, at the critical situation, with N_s, and the effect on the shear stress ratio, $\frac{\tau_o}{\tau_i}$, of heating from only the annulus inner surface.

19.1.2.3 All force effects considered

For this situation the model prediction is given by equation 63, which when written in terms of the parameter 'Y' gives

$$Y = \left[\frac{\left\{1 - \frac{1}{\rho_f g}\left(\frac{\tau_i + \tau_w}{\delta_i}\right)\right\}_{A.M.}}{1 + f_i . N_s \left(1 + \frac{\tau_o}{\tau_i} \cdot \frac{D_o}{D_i}\right)}\right]^{\frac{1}{2}} - \left[\frac{A}{1 + f_i N_s \left(1 + \frac{\tau_o}{\tau_i} \cdot \frac{D_o}{D_i}\right)}\right]^{\frac{1}{2}} \qquad 106$$

It is seen that Y is further reduced by the film friction effects included in the numerator of equation 106. Because (to the authors knowledge) the information necessary to evaluate this term, at the critical condition, for the experimental conditions investigated is at present unavailable, the model approach has not been taken any further. However the numerator of equation 106 is proportional to the maximum available pressure gradient and it is unity when this pressure gradient equals the hydrostatic pressure gradient. Therefore the maximum value of A is unity and in all practical situations $A < 1.0$. Shown on Fig. 26 is equation 106 evaluated for A = 0.25, 0.1, and 0.05.

19.2.0 Subcooled Water Entry

19.2.1 Experimental correlation

The final graphical correlation of the results obtained for all annuli, for subcooled water entry, over the complete pressure range is given on Fig. 25. Fig. 25 is composed of the curves given on Figs. 22, 23 and 24. It is seen that the results correlate reasonably well by plotting

$$S = \left(\frac{q_s}{q} - 1\right).\Delta T_s^{-1} \text{ against } \frac{L}{D_e}$$

19.2.2.0 Model prediction and comparisons

19.2.2.1 Zero liquid recirculation

The model predicts (equation 89) for the situation when frictional forces are dominant

$$S = \left(\frac{q_s}{q} - 1\right).\Delta T_s^{-1} = \frac{n.C_{pf}}{h_{fg}} \qquad 107$$

where n = liquid recirculation parameter

Now for n = 1 it has been shown (see equation 90 and below) that $S = 1.8 \times 10^{-3}/^{o}C$. This value constitutes the liquid "no recirculation" condition shown on Figs. 22 to 25 inclusive and appears to be the lower limit to which all the experimental curves tend at large $\frac{L}{D_e}$.

19.2.2.2 Range $\frac{L}{D_e} > 10$

For the range $\frac{L}{D_e} > 10$, reference to Fig. 25 indicates that S is not very dependent on the system pressure, but is dependent on the $\frac{L}{D_e}$ ratio, or more accurately on D_e as the annulus length was held constant throughout the experiment. This ratio was used because it formed a convenient dimensionless quantity and this fact should be kept in mind when interpreting the following equations. It therefore follows by reference to the model prediction (equation 107) that for this range, the liquid re-circulation "n" is a function of D_e, but not of pressure,

that is, $n = f(D_e)$

19.2.2.3 Range $\frac{L}{D_e} < 10$

For the range $\frac{L}{D_e} < 10$, reference to Fig. 25 indicates that S is dependent on D_e and on the system pressure. It therefore follows by reference to the model prediction (equation 107) that for this range, the liquid recirculation "n" is a function of D_e and of the system pressure, that is,

$n = f(D_e, \text{pressure})$

This relationship applies only until the pool boiling situation is attained.

19.2.2.4 Range $\frac{L}{D_e} \rightarrow 0$ i.e. Pool Boiling

Reference to the "horizontal" pool boiling correlations such as that due to Kutateladze et al (11) shows that

$$S = \left(\frac{q_s}{q} - 1\right).\Delta T_s^{-1} = \text{Const.}\left(\frac{\rho_f}{\rho_g}\right)^{\frac{3}{4}} \cdot \frac{C_{pf}}{h_{fg}} \qquad 108$$

Comparison of equation 108 with equation 107 gives

$$n = \text{Const.}\left(\frac{\rho_f}{\rho_g}\right)^{\frac{3}{4}} = f(\text{pressure})$$

Therefore for the upper pool boiling limit then "n" is likely to be a function of the system pressure only. (For vertical pool boiling it is feasible that the heater length could be important)

$\therefore n = f(\text{pressure})$

Referring then to equation 107, the equation predicted by the model, it is seen that this equation can predict the

system behaviour provided a suitable function is formulated for the liquid recirculation parameter "n" in terms of D_e (possibly $\frac{L}{D_e}$), and the system pressure. However because of the complexity that such a function would take together with the relatively limited experimental range investigated it has been decided expedient to leave the final correlation in the graphical form as given on Fig. 25.

20.0.0.

D I S C U S S I O N

DISCUSSION

20.1.0. Vertical Pool Boiling

The 3.15 m.m. O.Dia. by 0.79 m.m. wall by 12.4 cm. long stainless steel specimen was tested under vertical pool boiling conditions, that is, without any annular surround apart from the boiling vessel. The results of this test are shown on Fig. 8. Comparison of the saturated critical heat flux results for vertical pool boiling (Fig. 8) with the corresponding results for horizontal pool boiling (Fig. 13 of Part I, bottom curve) indicates that the two curves are very nearly identical. Thus the ratio of the vertical pool boiling saturated critical heat flux to the corresponding horizontal pool boiling saturated critical heat flux can be taken as unity over the whole vacuum range tested. Kutateladze et al (Fig. 1 of Ref. 11) show that this ratio, at atmospheric pressure, is a function of the heater diameter and that for heater diameters greater than about 2.8 m.m. this ratio is unity. The present results thus support the findings of Kutateladze et al (11) and also show that this behaviour extends into the vacuum region. The critical heat flux positions for vertical saturated pool boiling were random along the heater length. However as the pool subcooling increased so the critical heat flux positions tended to occur at the top end of the heater. This behaviour was probably due to the water temperature around the heater increasing from heater bottom to top due to buoyancy effects. Under vertical subcooled pool boiling conditions therefore it is probable that the critical heat flux is a function of the heater length and thus the subcooled results presented in Fig. 8 are probably only applicable to the particular heater tested. This is not so under saturated boiling conditions when the water temperature surrounding the specimen will be constant.

20.2.0. Annuli Results

Figs. 9 and 10 show complete sets of results for a "large" annulus and a "small" annulus respectively (sizes are given on Figs. 9 and 10). The general behaviour of the large

annulus is very similar to the vertical pool boiling results given on Fig. 8 except that the critical heat flux level has been generally reduced. However the behaviour of the small annulus results shows not only that the critical heat flux levels have been very much reduced, but also that the critical heat flux characteristics in the subcooled region are different. The "flatter" subcooled characteristic applicable to the small annulus indicates that there is only a small gain, with pool subcooling, in the critical heat flux. This is most likely due to the water recirculation between the annulus and the main pool being relatively small for the small annulus and thus very little extra energy being removed by this process.

20.3.0. Saturated entry to annulus

For saturated water entry conditions Fig. 15 shows the final correlation of the mean experimental results obtained at three different system pressures of 760 torr., 360 torr., and 160 torr. The key to the results is given on Fig. 15. The correlation is obtained on Fig. 15 by plotting the dimensionless vapor velocity, J^*_g, against the product of $N_f^{0.47}$ and $N_a^{-0.83}$ and it has been previously shown (see equation 93) that the law of the line is

$$J^*_g = 11.8 . N_a^{0.83} . N_f^{-0.47}$$

This correlation applies over the range $0.6 > J^*_g > 0.02$ when pool boiling effects are no longer present and it can be rewritten approximately (see equation 99) for the present set of experiments, in which the heater length was held essentially constant, as

$$J^*_g = 0.02 . N_s^{0.83}$$

For comparison with the model predictions the above equation has been written in terms of the parameter, "Y", (see equation 101) as

$$Y = 0.08 . N_s^{0.33}$$

The actual comparison is given on Fig. 26 where it is seen that the approximate experimental correlation given above lies well below the model predicted line for small N_s for the situation when all frictional effects have been neglected, but that the two lines converge as the shape factor, N_s, becomes larger. This behaviour implies that the vapour acceleration forces could be significant in this region of operation. Shown in dotted on Fig. 26 are the model predictions when friction is considered present and acting on the vapour core and the maximum available pressure gradient is varied from hydrostatic (A = 1.0) down to 0.05 hydrostatic (A = 0.05). It is seen that the model predicts the dimensionless vapour velocity, J^*_g, as an important correlating parameter and also predicts, when all friction forces are considered absent, an upper limit to J^*_g as follows

$$J^*_g = 0.25.N_s^{\frac{1}{2}}$$

Further the model indicates the correct variations in J^*_g with increasing friction effects and with a reduced maximum available driving pressure gradient. However the trend of the experimental line is not correctly predicted. This is due to the authors inability to predict friction factor behaviour and liquid film behaviour at the annulus critical condition.

To present the magnitudes of the critical heat flux values determined, Fig. 15 has been replotted in the dimensional form of Fig. 16. This plot shows quite well how the points ultimately tend towards the limiting pool boiling values - shown as horizontal lines marked with the applicable pressure on Fig. 16. Reference to Fig. 16 suggests, that if the system pressure is increased above the levels tested, then the resulting points would continue to plot along the straight line shown in chain dotted until they finally broke away towards their appropriate pool boiling critical heat flux value. Fig. 16, which is applicable to annuli, is a comparable plot to that presented by Wallis (Fig. 14.17 of (7)) for tubes.

20.4.0. Subcooled Entry to Annulus

Fig. 18 shows, plotted against $\frac{L}{D_e}$, for a typical annulus assembly, the saturated entry critical heat flux, "q", the subcooled entry critical heat flux for 50°C of subcooling, "q_{50}", and the ratio of these two quantities, $\frac{q_{50}}{q}$. Reference to Fig. 18 shows that although both "q" and "q_{50}" increase monotonically with reducing $\frac{L}{D_e}$, the ratio $\frac{q_{50}}{q}$ does not, but has the unexpected shape shown. This unexpected shape is therefore caused by the different rates of increase of the composite curves with $\frac{L}{D_e}$.

Now the separated flow model predicts for the subcooled entry situation when friction forces dominate (equation 89) that

$$S = \left(\frac{q_s}{q} - 1\right).\Delta T_s^{-1} = n.\frac{C_{pf}}{h_{fg}}$$

For the pressure range investigated the ratio of the water specific heat to the enthalpy of vaporisation is essentially a constant. Therefore the experimental results should plot as "S" against "n", where "n", the liquid recirculation parameter could depend on the system geometry and pressure. Figs. 22 to 24 inclusive show the parameter "S" plotted against $\frac{L}{D_e}$ for system pressures of 760 torr., 360 torr., and 160 torr., respectively. It is seen by reference to these figures that the vast majority of the results are correlated to $\pm$ 25%. Further for large $\frac{L}{D_e}$ all these correlating curves appear to tend to the same constant value of "S" (1.8×10^{-3}/°C) predicted by equation 89 when the liquid recirculation "n" is taken equal to unity, that is, there is no liquid recirculation.

Now Fig. 25 shows the three curves taken from Figs. 22 to 24 inclusive superimposed on the same graph. Reference to this figure indicates, for $\frac{L}{D_e} > 10$, that "S" shows little dependence on pressure and is only dependant on the system geometry. Now the model could predict this behaviour by assuming that the liquid recirculation is only a function of geometry in this region and that for large values of $\frac{L}{D_e}$ this function becomes equal to unity. For the region $\frac{L}{D_e} < 10$,

Fig. 25 indicates that "S" is a function of both geometry and pressure until finally the pool boiling situation is reached when "S" becomes a function only of pressure. Again the choice of a suitable function of system geometry and pressure for the liquid recirculation parameter, "n", could predict this behaviour. It is therefore seen that the model could explain the experimental behaviour over the whole range by making "n" a suitable function of pressure and geometry. However because of the complexity of the required function, and the limited experimental results the author did not consider it expedient to attempt to formulate a suitable function and has therefore left the final correlation in the graphical form of Fig. 25.

It is worthwhile noting, that had $\frac{C_{pf}}{h_{fg}}$ been a significant function of pressure over the pressure range investigated, then it would have been better to plot the results in the form:

$$\frac{h_{fg}}{C_{pf}} \left(\frac{q_s}{q} - 1 \right) . \Delta T_s^{-1} \text{ against } \frac{L}{D_e}$$

21.0.0.

C O N C L U S I O N S

CONCLUSIONS

1. Critical heat flux values have been obtained, for both saturated and subcooled pool boiling, for a vertically mounted stainless steel specimen of outside diameter 3.22 m.m. For this diameter of heater specimen the ratio of the saturated critical heat flux for a vertically mounted heater to that for a horizontally mounted heater has been determined as unity over the vacuum range tested (760 torr. to 160 torr.). This finding agrees, at atmospheric pressure, with that due to Kutateladze et al (11) who determined this ratio for boiling at atmospheric pressure only. For subcooled boiling the positions on the heater at which the critical condition occurred tended to occur predominantly at the heater top and therefore these results are probably only applicable to this particular specimen.

2. Critical heat flux results have been obtained, for confined boiling in annuli, for both saturated and subcooled water entry, over a pressure range of 760 torr. to 160 torr. The saturated water entry results have been correlated to within $\pm$ 25% over the range $0.6 > J_g^* > 0.02$ by the equation

$$J_g^* = 11.8.Na^{0.83}.N_f^{-0.47}$$

The subcooled water entry results have been correlated by plotting the parameter "S" against $\frac{L}{D_e}$ and the correlation has been left in graphical form and is shown on Fig. 25. The vast majority of the results are correlated to within $\pm$ 25%. Reference to Fig. 25 indicates that for $\frac{L}{D_e}$ greater than ten, that the parameter "S" is virtually independant of pressure over the pressure range investigated (760 torr. to 160 torr.) and that for large $\frac{L}{D_e}$ the results appear to tend towards the value predicted by the separated flow model for zero water recirculation.

3. In a two phase counter current flow system with progressive evaporation there are three possible relevant forces acting at the critical or limiting situation. These are buoyancy, friction, and vapour momentum increase forces. Now Wallis (15)

devised the dimensionless vapour velocity parameter, j_g^* by considering the ratio of the first two of these forces and j_g^* is physically the same as the parameter J_g^* used by the present author - the only difference being a multiplying constant. Now the present author has shown that when the above three forces are important then two other dimensionless parameters could be important, they are Y_g^* and N_s. These two additional parameters have been derived by considering force ratios containing the vapour momentum increase force.

4. A one dimensional separated flow type of model in which void fraction effects have been neglected has been developed. This model has been applied to annuli subjected to both the saturated water entry and the subcooled water entry conditions. The model has shown J_g^* to be a relevant dimensionless quantity and has given an upper limit to J_g^* when friction forces are neglected. This upper limit to J_g^* is given by equation 57 as $J_g^* = \frac{1}{4} N_s^{\frac{1}{2}}$. Further it has been noted, equation 58, that if this relationship is rearranged as follows then we obtain $J_g^*/N_s^{\frac{1}{2}} = Y_g^* = \frac{1}{4}$, where Y_g^* is a new dimensionless parameter obtained from the ratio of the vapour momentum increase force and the corresponding buoyancy force (see equations 35 and 36). Thus this upper limit is obtained when in the absence of frictional forces the "required" vapour momentum increase force just equals the "available maximum" driving buoyancy force. However the model has been unable to predict in detail the experimental results due to the authors inability to predict friction factor and water film behaviour at the critical condition. The model, by the introduction of the water recirculation parameter, "n", could be made to predict the subcooled entry results if "n" was made a suitable function of the system geometry and pressure. For the subcooled water entry region the model highlighted the parameter, "S", as a correlating factor and allowed the limiting value of "S" to be predicted when the water recirculation parameter, "n" was taken as unity, that is the water recirculation was zero.

5. Had the author been working over a large pressure range then there would have been a significant variation in the fluid

property ratio $\frac{C_{pf}}{h_{fg}}$. Under these conditions, for the subcooled water entry condition, the model predicts as a correlating parameter, not "S", but "$\frac{h_{fg}}{C_{pf}}$. S".

22.0.0.

A P P E N D I X

APPENDIX

Approximate expression for $(1 + \frac{\tau_o}{\tau_i} \cdot \frac{D_o}{D_i})$ in terms of the annulus geometry number, Na

Let D_s be the diameter of the cylindrical surface of zero shear stress in the vapour core. If we neglect the volume occupied by the liquid films, and vapour acceleration effects then

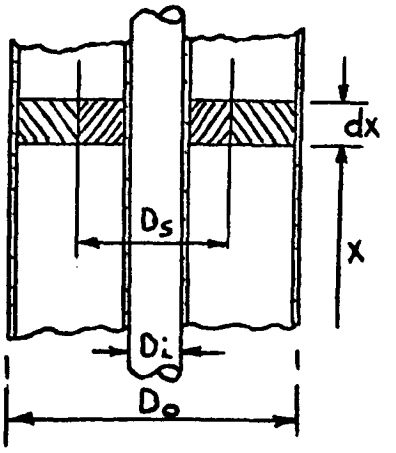

ANNULUS

1) A force balance across the control volume bounded by D_s and D_i and shown shaded in sketch gives

$$-\tau_i.\pi.D_i.dx - \rho_g.\frac{\pi}{4}(D_s^2-D_i^2)g.dx - dp\,\frac{\pi}{4}(D_s^2-D_i^2) = 0$$

rearranging

$$-\frac{dp}{dx} - \rho_g.g = \frac{4.\tau_i.D_i}{D_s^2 - D_i^2} \qquad 109$$

2) A force balance across control volume bounded by D_o and D_s and shown shaded in sketch gives us

$$-\tau_o.\pi.D_o.dx - \rho_g.\frac{\pi}{4}(D_o^2-D_s^2)g.dx - dp\,\frac{\pi}{4}(D_o^2-D_s^2) = 0$$

rearranging

$$-\frac{dp}{dx} - \rho_g.g = \frac{4.\tau_o D_o}{D_o^2 - D_s^2} \qquad 110$$

Now equating equations 109 and 110 gives

$$\frac{\tau_o.D_o}{D_o^2-D_s^2} = \frac{\tau_i.D_i}{D_s^2-D_i^2}$$

$$\therefore\ 1 + \frac{\tau_o}{\tau_i}\cdot\frac{D_o}{D_i} = \frac{D_o^2 - D_i^2}{D_s^2 - D_i^2} \qquad 111$$

Now an expression is required for D_s, the diameter of the cylindrical surface of zero shear in terms of D_o and D_i.

Therefore assuming, in a similar manner to Lee and Barrow (12), that for steady flow in an annulus

1) the zero shear stress plane in the annulus occurs at the radius of maximum velocity

2) the radius of maximum velocity in turbulent flow in an annulus coincides with the radius of maximum velocity in laminar flow in an annulus.

Now Lamb (13) gives the velocity profile for laminar flow in an annulus as

$$V = C_1 \left[D_o^2 - D^2 + \frac{D_o^2 - D_i^2}{\log_e \frac{D_o}{D_i}} \cdot \log_e \frac{D}{D_i} \right] \qquad 112$$

To find the diameter $D = D_s$ for which V is a maximum then equation 112 must be differentiated and equated to zero

$$\therefore \frac{dV}{dD} = C_1 \left[-2.D + \frac{D_o^2 - D_i^2}{\log_e \frac{D_o}{D_i}} \cdot \frac{1}{D} \right] = 0, \text{ for } D = D_s$$

$$\therefore D_s^2 = \frac{D_o^2 - D_i^2}{\log_e \frac{D_o^2}{D_i^2}} \qquad 113$$

$\therefore$ we substitute equation 113 into 111 to obtain

$$1 + \frac{\gamma_o}{\gamma_i} \frac{D_o}{D_i} = \frac{(D_o^2 - D_i^2)\log_e \frac{D_o^2}{D_i^2}}{D_o^2 - D_i^2 - D_i^2 \log_e \frac{D_o^2}{D_i^2}} \qquad 114$$

Now substituting into 114 for $N_a = \frac{D_i^2}{D_o^2 - D_i^2}$ then equation 114 becomes

$$\left(1 + \frac{\gamma_o}{\gamma_i} \cdot \frac{D_o}{D_i}\right) = \frac{\log_e \left(1 + \frac{1}{Na}\right)}{1 - Na \cdot \log_e \left(1 + \frac{1}{Na}\right)} \qquad 115$$

Now equation 115 is only an approximation to the present experimental situation as the fact that evaporation is occurring and that this evaporation is mainly from the centre surface is likely to significantly influence the vapour velocity profile. Thus the assumption that the velocity peak coincides with that due to laminar flow in an annulus is probably only approximately correct.

23.0.0.

REFERENCES

REFERENCES

1. Wallis G. Flooding Velocities for Air/Water in Vertical Tubes. U.K.A.E.A. Report A.E.E.W.-R.123 Dec. 1961.

2. Silver, R. S. A Thermodynamic Theory of Circulation in Water-tube Boilers. Proc. Instn. Mech. Engrs. 1945, 153, Pages 261,281.

3. Silver, R. S. Written Discussion of Paper No. 9 - Symp. Two-Phase Flow Instn. of Mech. Engrs. 1962, Page 105.

4. Silver, R. S. Opening Address at "Designing for Two-Phase Flow" Meeting Jan. 1968. N.E.L. Report 385, Ministry of Technology.

5. Griffith et.al. Flooding and Burn-Out in Closed-End Vertical Tubes. Symp. Two-Phase Flow, Paper 5, Instn. of Mech. Engrs. 1962, Pages 35-44.

6. Gambill, W. R. Overheating and Burn-Out of Blocked Vertical Channels Cooled Internally by Water. 2nd Int. Congress on Chemical Eng. Mariebad, Czechoslovakia, Paper B1.9, Sept. 1965.

7. Wallis and Collier. Two Phase Flow and Heat Transfer. Vol. III. Notes for Summer Course at (i) Stanford University and (ii) Glasgow University, 1967

8. Frea, W. J. Two Phase Heat Transfer and Flooding in Counter Current Flow. Int. Conf. on Heat Transfer, Paris 1970, Paper B.5.10.

9. Shires et al. Film Cooling of Vertical Fuel Rods. U.K.A.E.A., Report A.E.E.W.-R.343, May 1964.

10. Silver, R. S. Letter to the Editors, Int. J. Heat Mass Transfer, Vol. 14, No. 12, 1971. Page 2175.

11. Kutateladze et al. Effects of Heater Size on Critical Heat Loads in the Boiling of a Liquid with Free Convection. High Temperature Vol. 5, Part 5, 1967, pp 747-752.

12. Kutateladze et al. The Critical Heat Flux at the Pool Boiling of some Binary Mixtures. Paper 96. Third International Heat Transfer Conference, Chicago, August 1966.

13. Lee et al. Turbulent flow and Heat Transfer in Concentric and Eccentric Annuli. Thermodynamics and Fluid Mechanics Convention. I.Mech.E. Cambridge 1964, Paper 12.

14. Lamb. Hydrodynamics. Pub. Cambridge University Press, Sixth Edition, Page 586.

15. Wallis, G. B. One Dimensional Two-Phase Flow. Pub. McGraw-Hill Book Company, 1969, Page 336.

24.0.0.

PART II - FIGURES

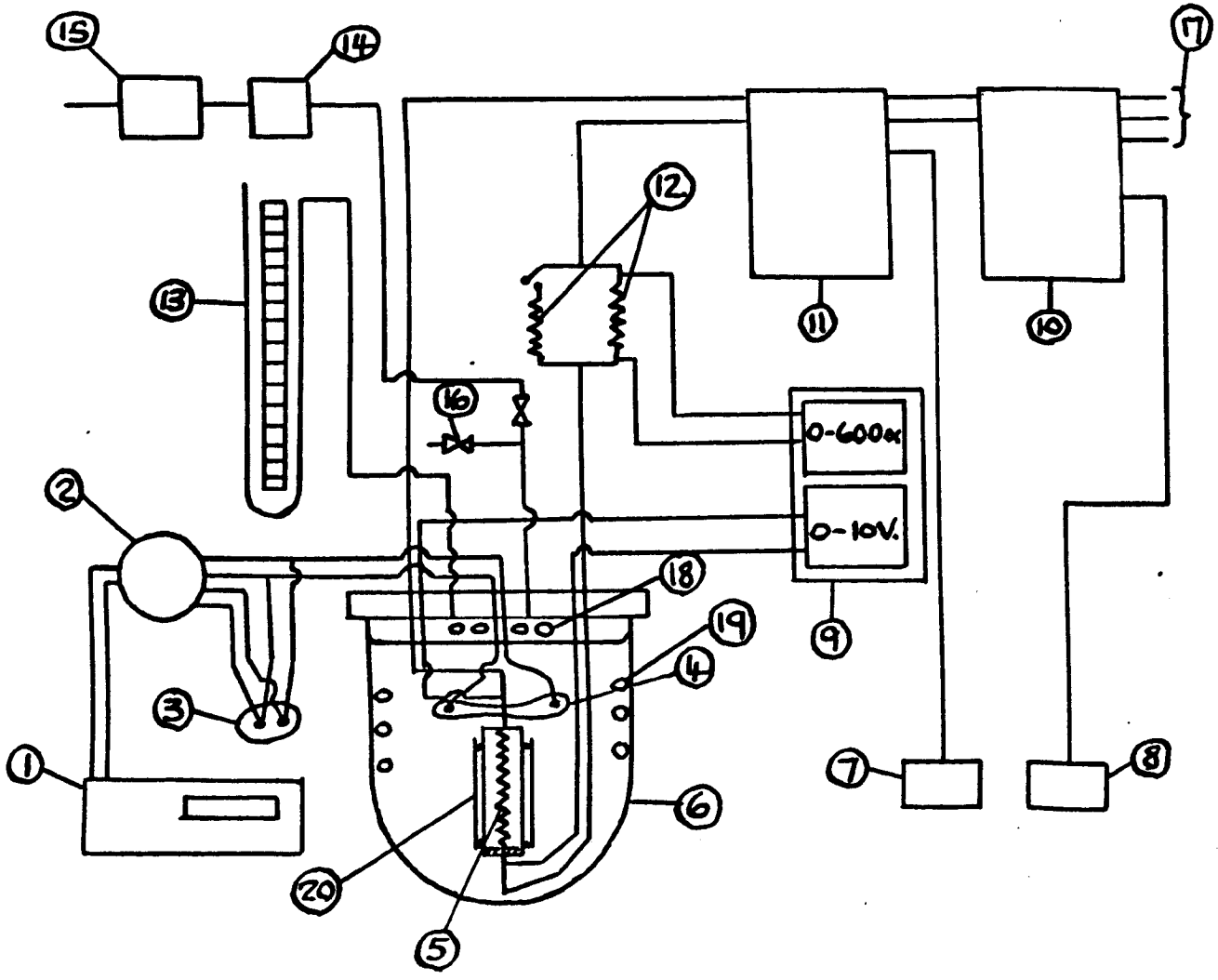

ITEM	Nº
Digital Voltmeter	1.
Rotary Switch	2.
Thermocouple Cold Junctions	3.
Thermocouple Hot Junctions	4.
Annulus Heater	5.
Boiling Cell	6.
Trip Unit	7.
Remote Drive Unit	8.
Dual Channel Pen Recorder	9.
Autotransformer	10.
Rectifier	11.
Calibrated Shunts	12.
Mercury Manometer	13.
Water Trap	14.
Jet Pump Vacuum Unit	15.
Controllable Air Leak	16.
Three Phase Supply	17.
Condenser Coil	18.
Cooling Coil	19.
Annulus Glass Surround	20.

FIG. 1. SCHEMATIC LAYOUT OF TWO-PHASE FLOW RIG

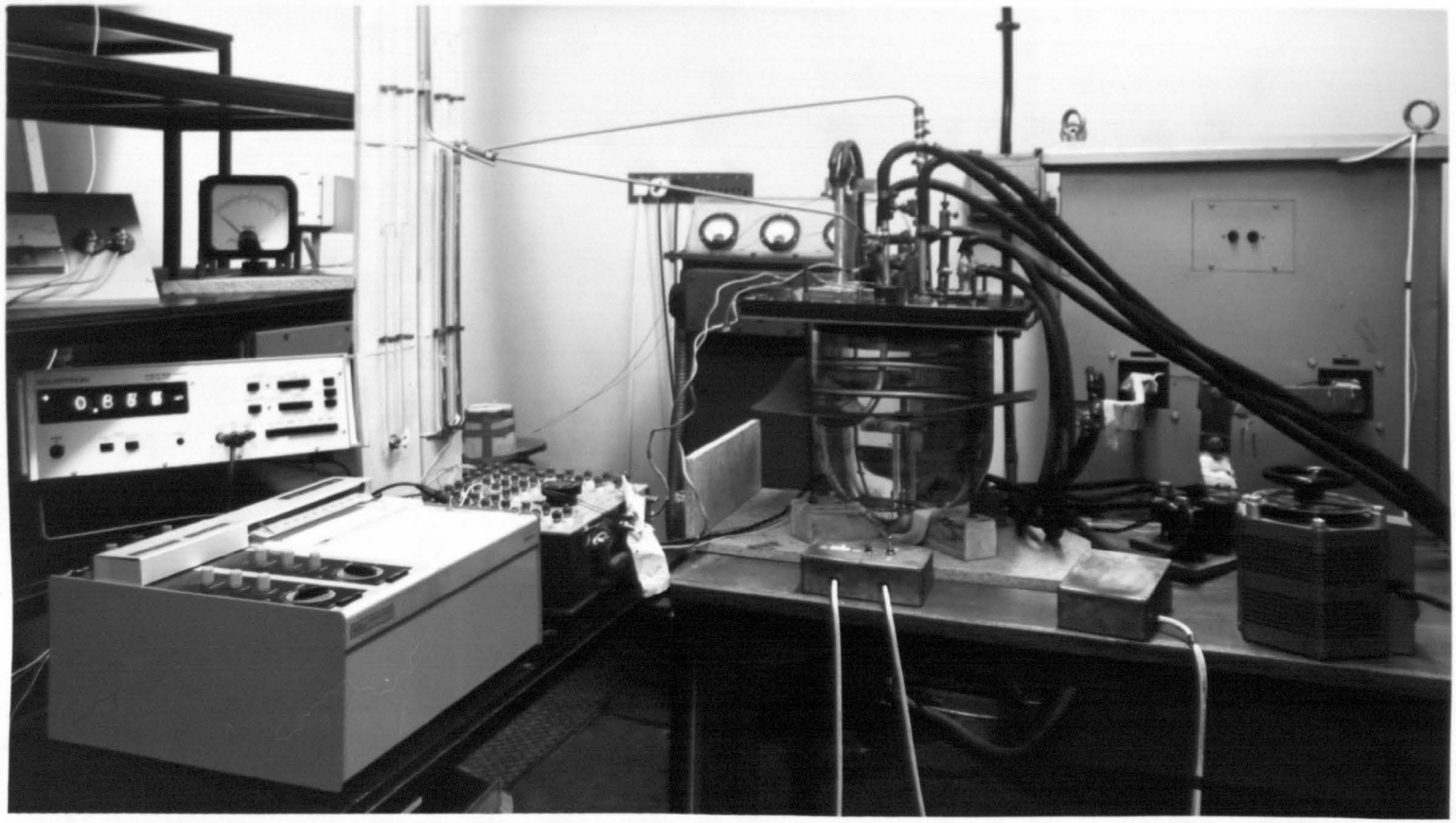

FIG. 2 TWO PHASE FLOW RIG

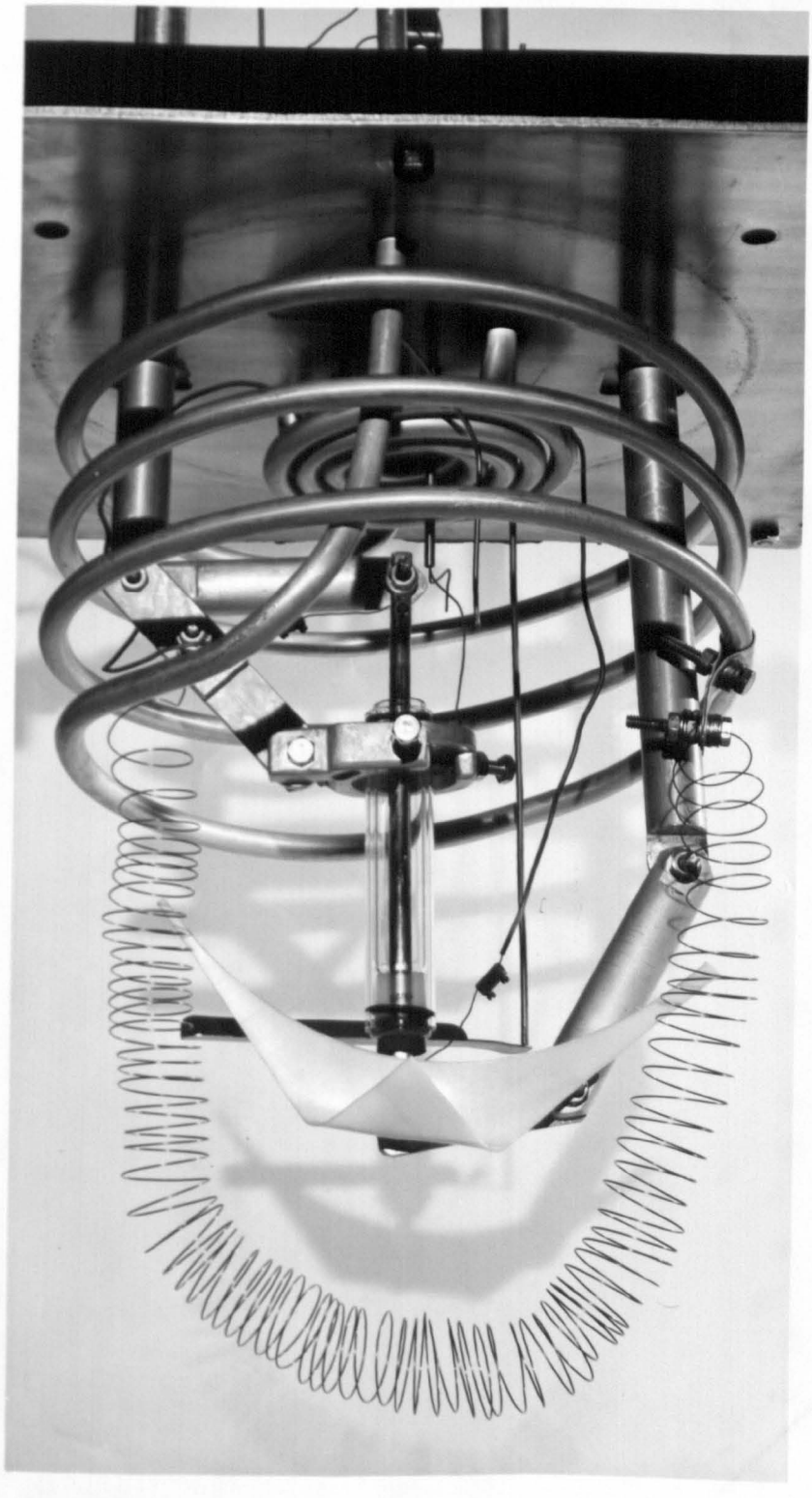

FIG. 3 INNER ASSEMBLY OF BOILING CELL

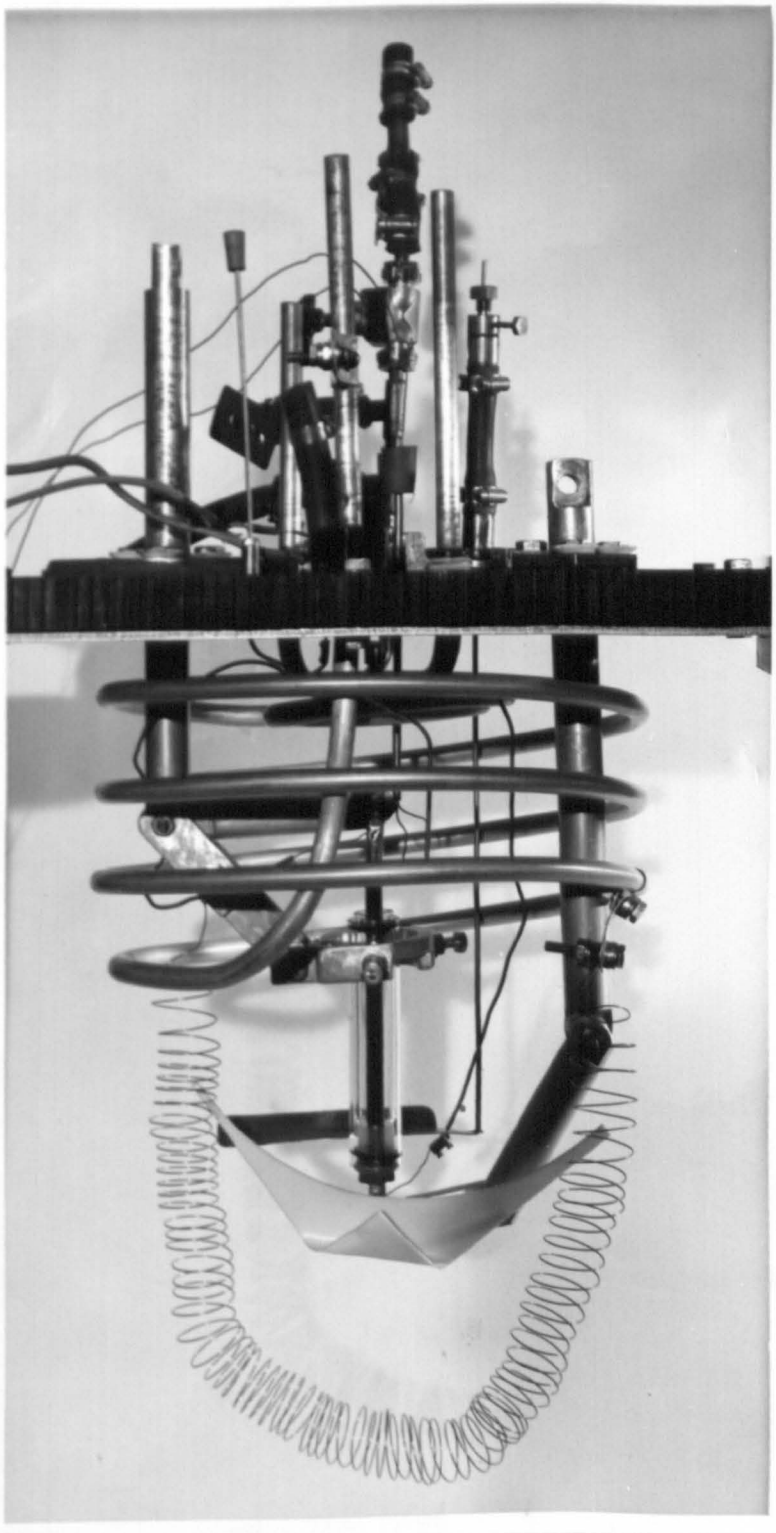

FIG. 4 UPPER SURFACE AND INNER ASSEMBLY OF BOILING CELL

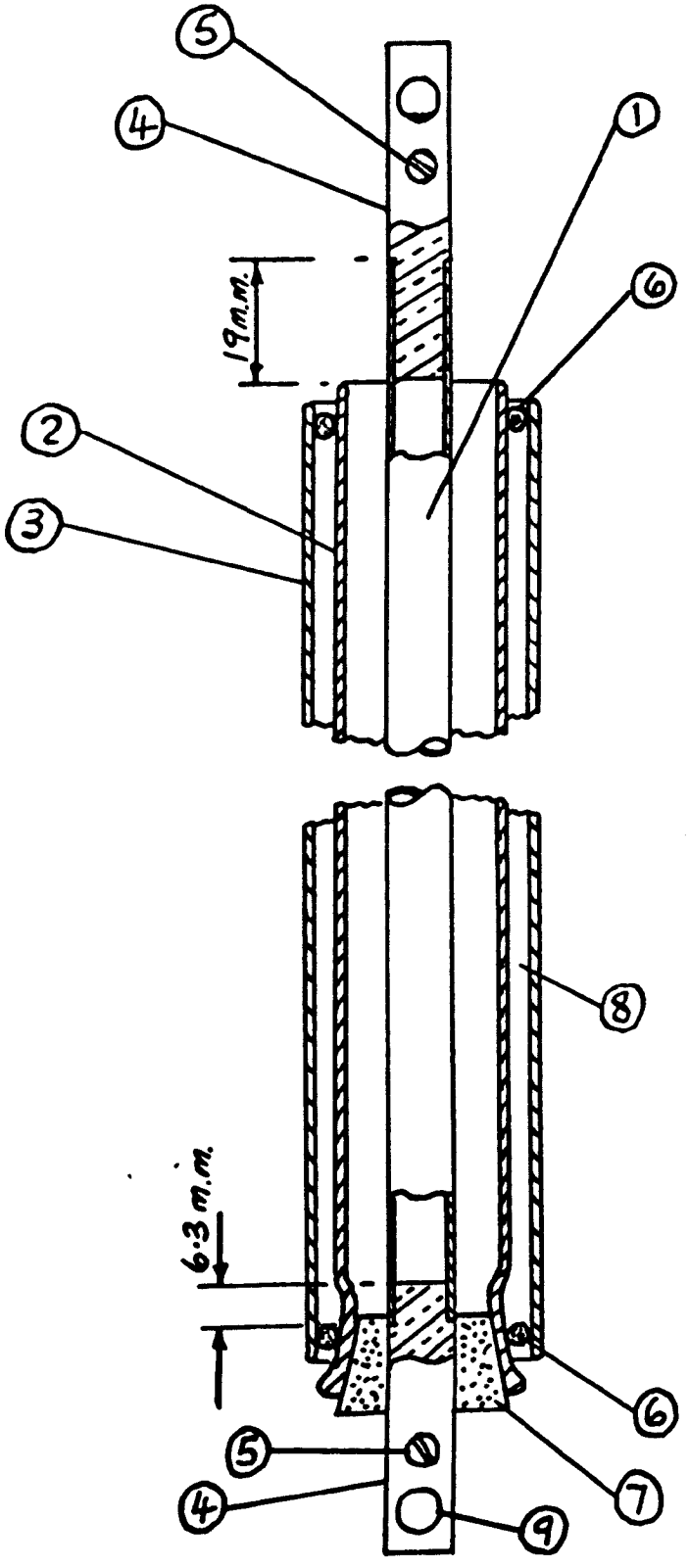

ITEM	Nº
S/S Heater	1.
Annulus Glass Wall	2.
Outer Glass Wall	3.
Brass End Piece	4.
Voltage Tap	5.
'O' Ring Seal	6.
Rubber Base Seal	7.
Annular Air Gap.	8.
Clamping Hole	9.

FIG. 5. TYPICAL HEATER - ANNULUS ASSEMBLY

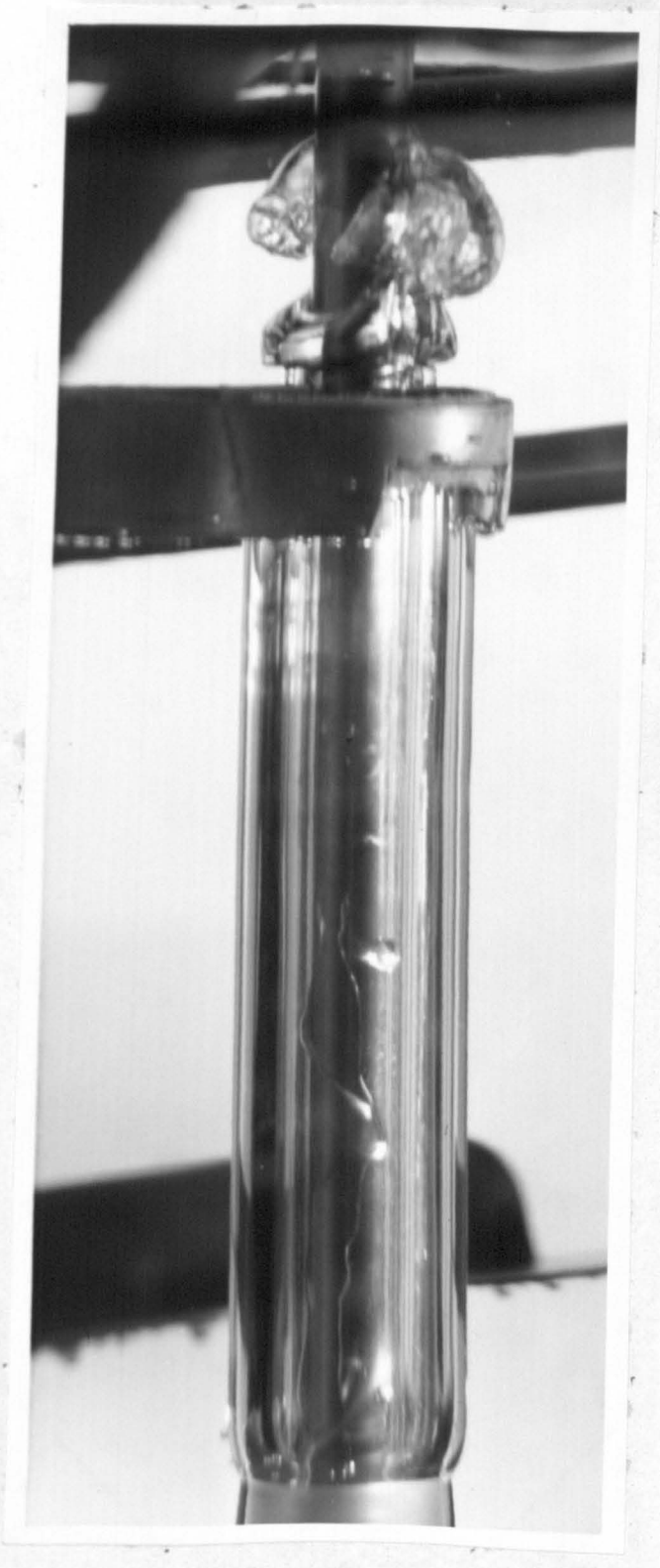

FIG. 6 ANNULUS (11.3 m.m. O.D. x 9.53 m.m. I.D.) BOILING AT 75% OF LIMITING HEAT FLUX. POOL TEMPERATURE - 86°C, PRESSURE - 760 torr.

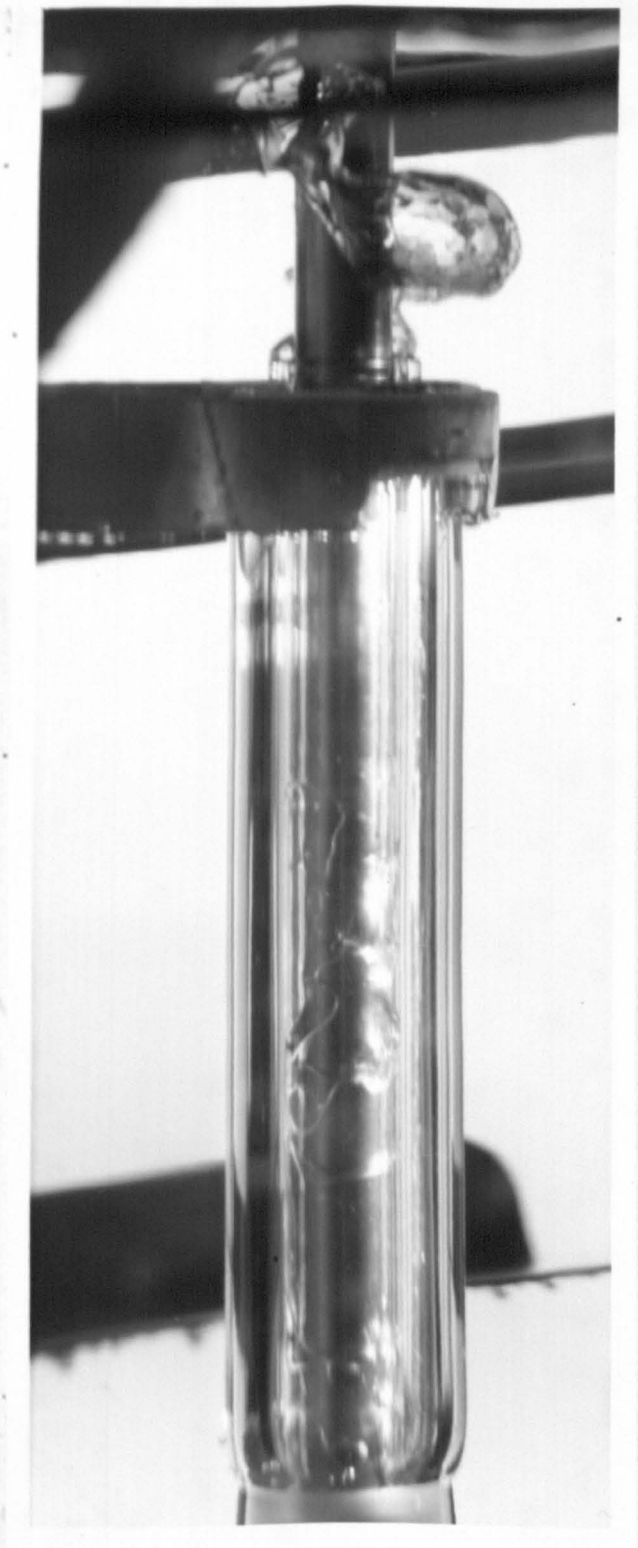

FIG. 7 ANNULUS (11.3 m.m. O.D. x 9.53 m.m. I.D.) BOILING AT LIMITING HEAT FLUX. CIRCUMFERENTIAL DRY AREA FORMED AND HEATER TEMPERATURE CONTINUOUSLY RISING. POOL TEMPERATURE - 88°C, PRESSURE - 760 torr.

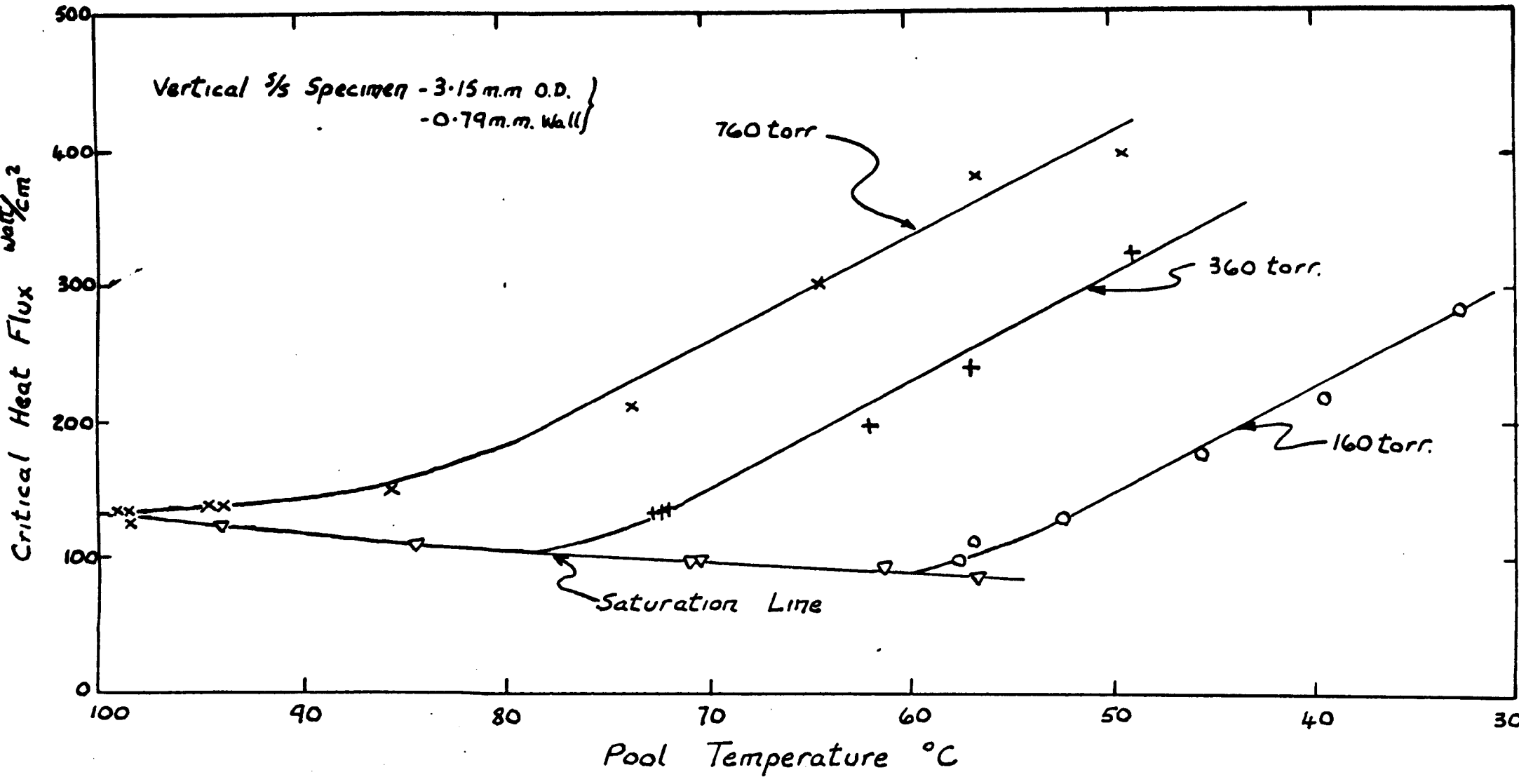

FIG. 8. CRITICAL HEAT FLUX VERSUS POOL TEMPERATURE FOR SUBCOOLED AND SATURATED CONDITIONS WITH PRESSURE VARIABLE. SPECIMEN VERTICAL – POOL BOILING

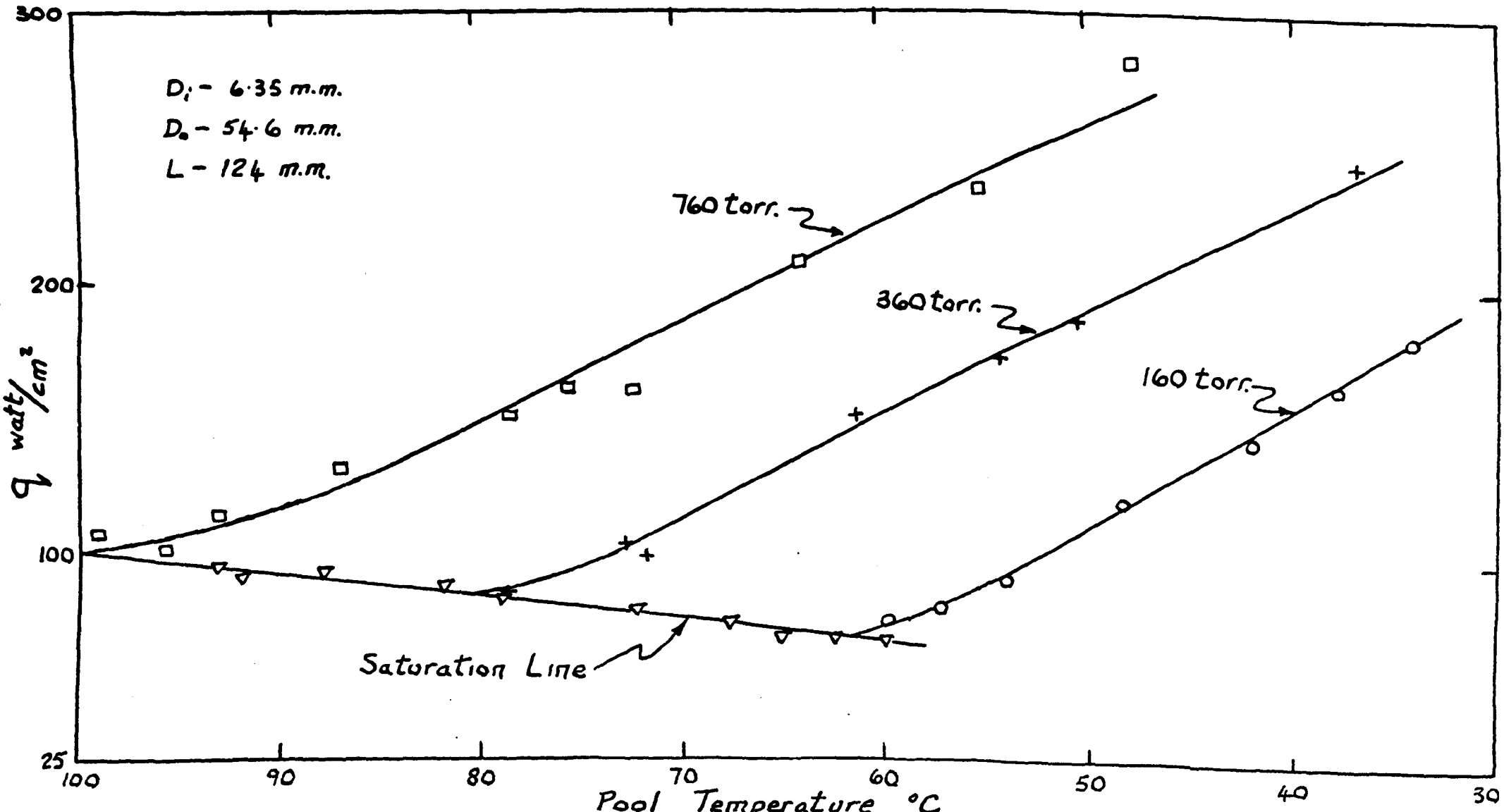

FIG. 9. CRITICAL HEAT FLUX VERSUS POOL TEMPERATURE FOR SUBCOOLED AND SATURATED CONDITIONS

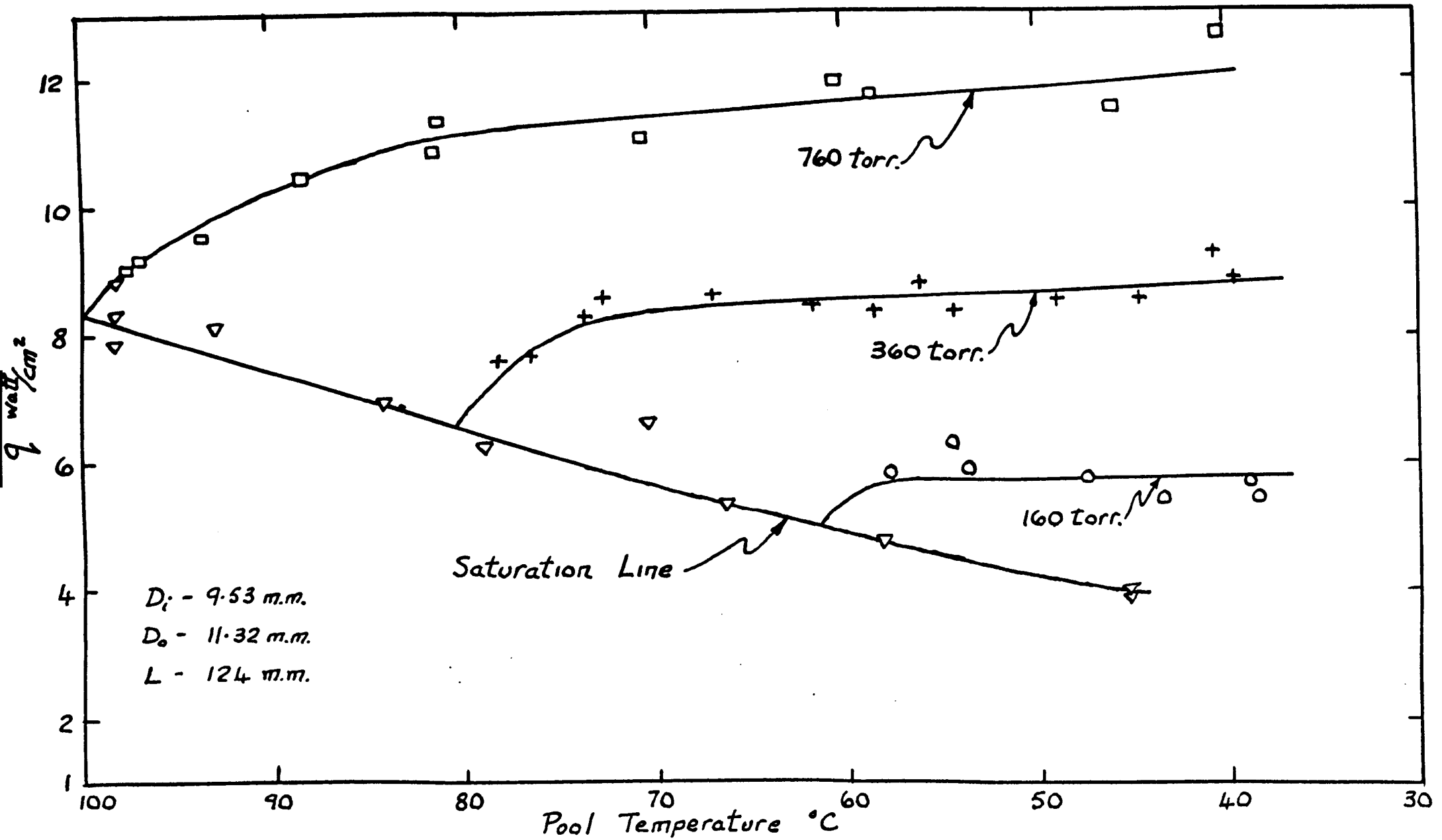

FIG.10. CRITICAL HEAT FLUX VERSUS POOL TEMPERATURE FOR SUBCOOLED AND SATURATED CONDITIONS

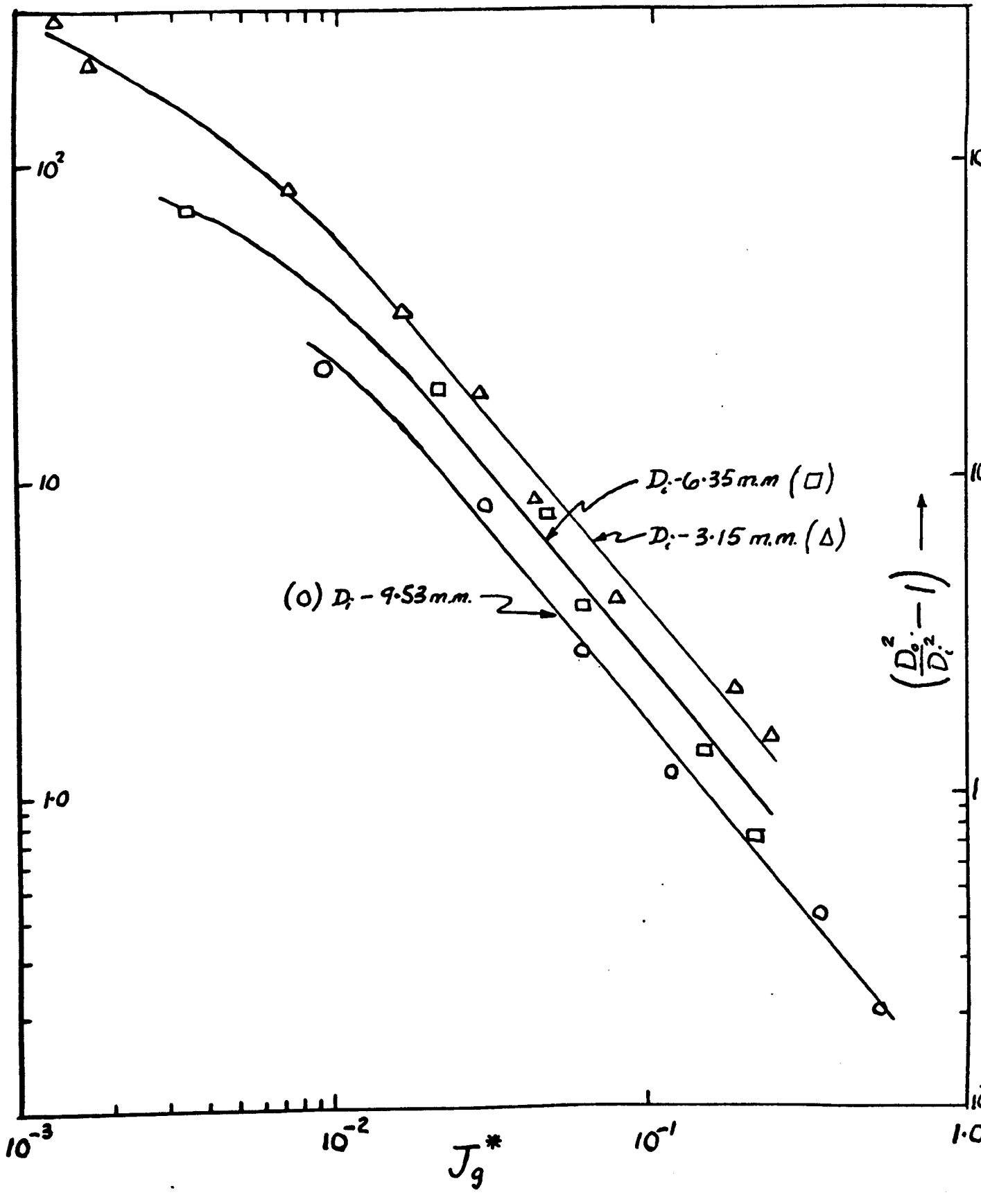

FIG. 11. VARIATION OF DIMENSIONLESS VAPOUR VELOCITY AT PRESSURE OF 760 TORR.

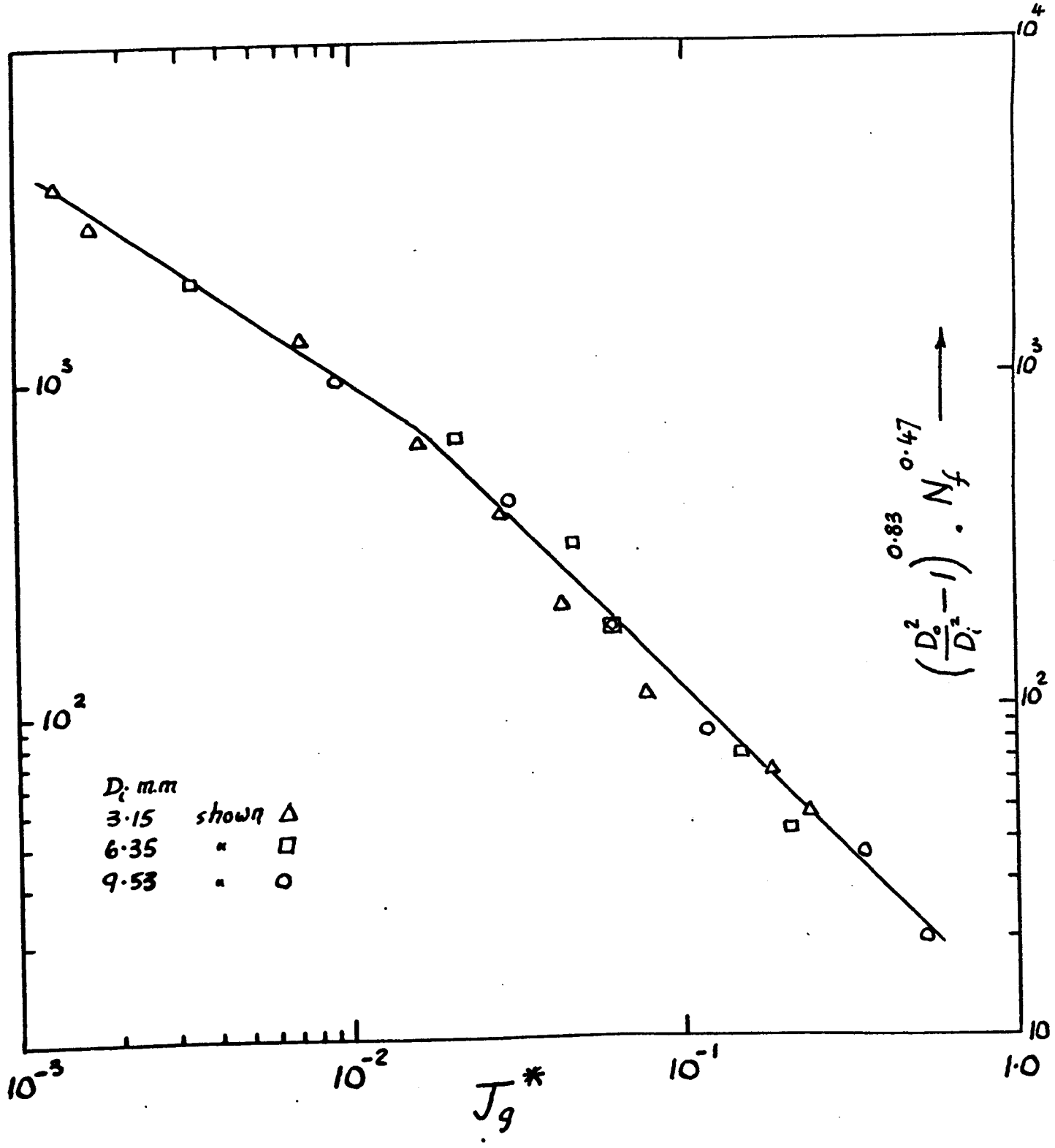

FIG. 12. VARIATION OF DIMENSIONLESS VAPOUR VELOCITY - PRESSURE 760 TORR.

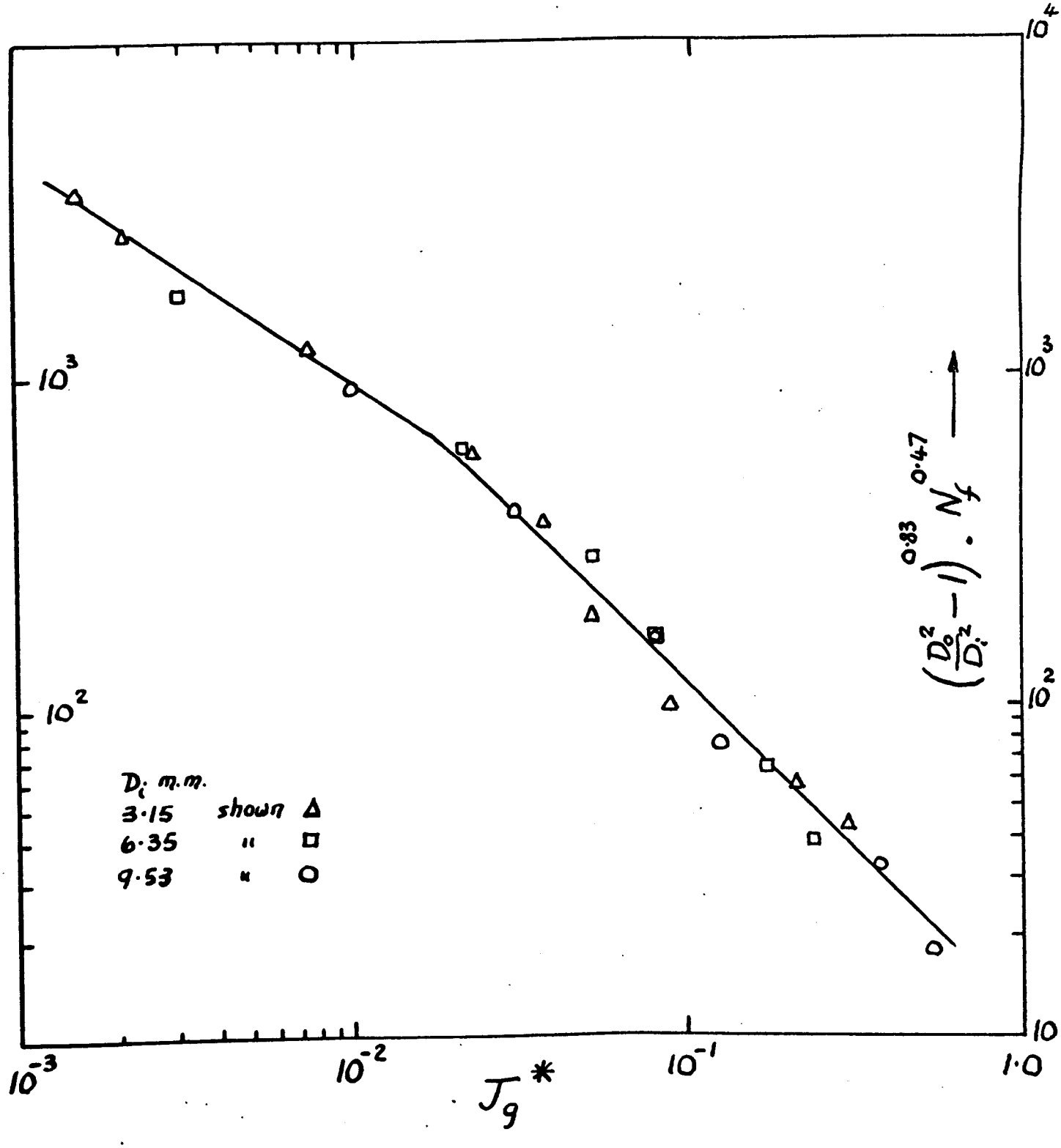

FIG. 13. VARIATION OF DIMENSIONLESS VAPOUR VELOCITY - PRESSURE 360 TORR.

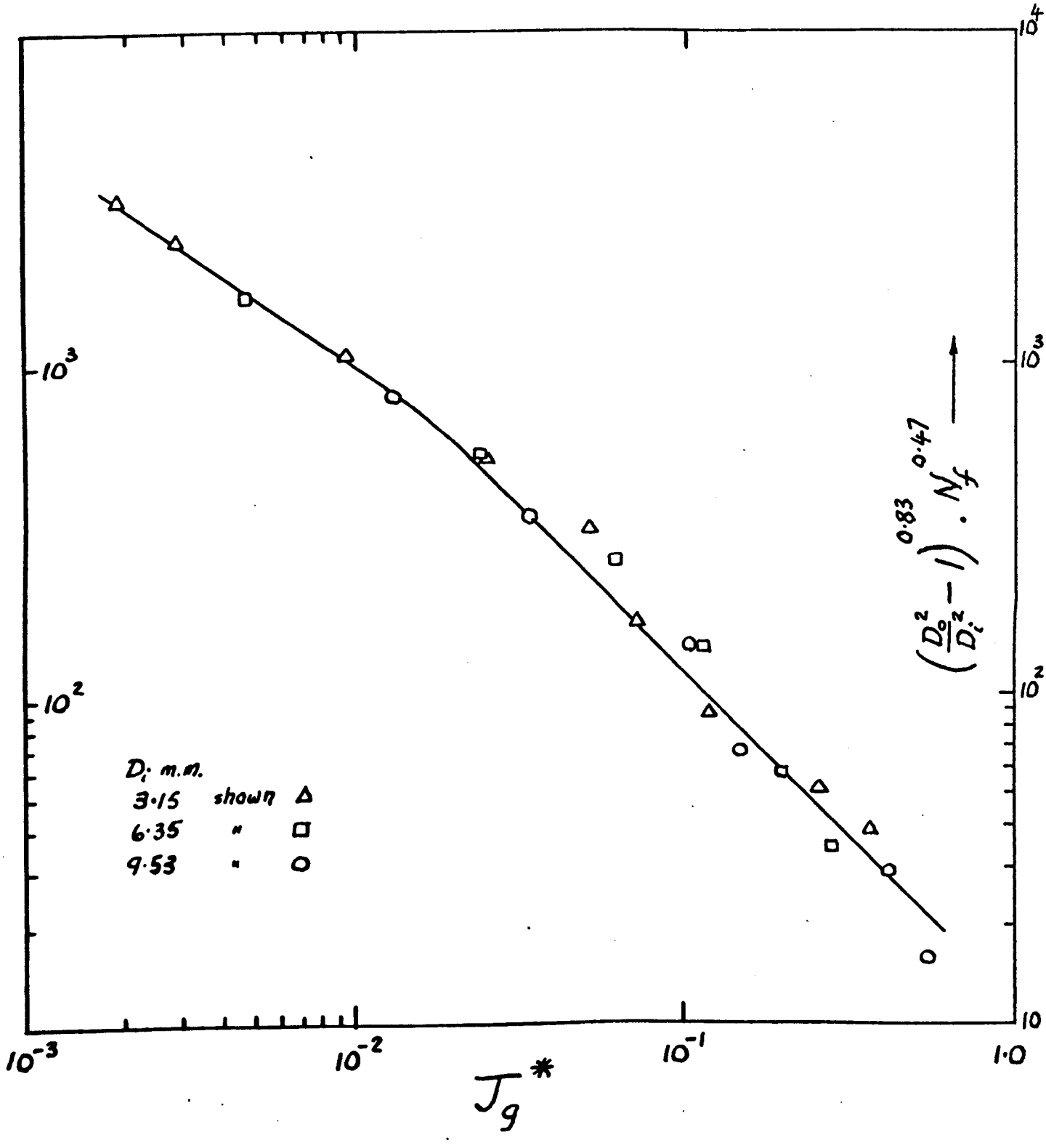

FIG. 14. VARIATION OF DIMENSIONLESS VAPOUR VELOCITY - PRESSURE 160 TORR.

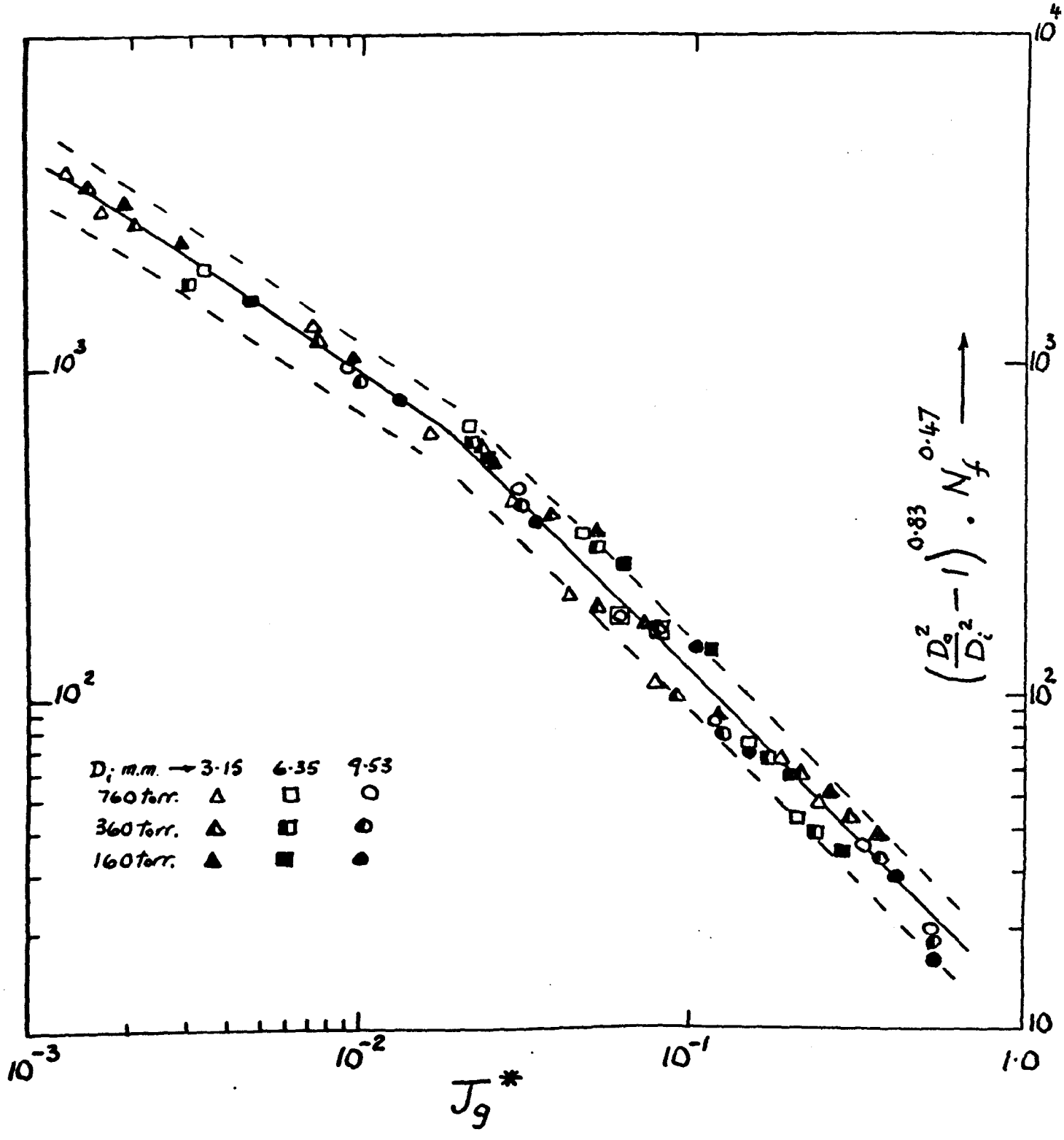

FIG. 15. VARIATION OF DIMENSIONLESS VAPOUR VELOCITY

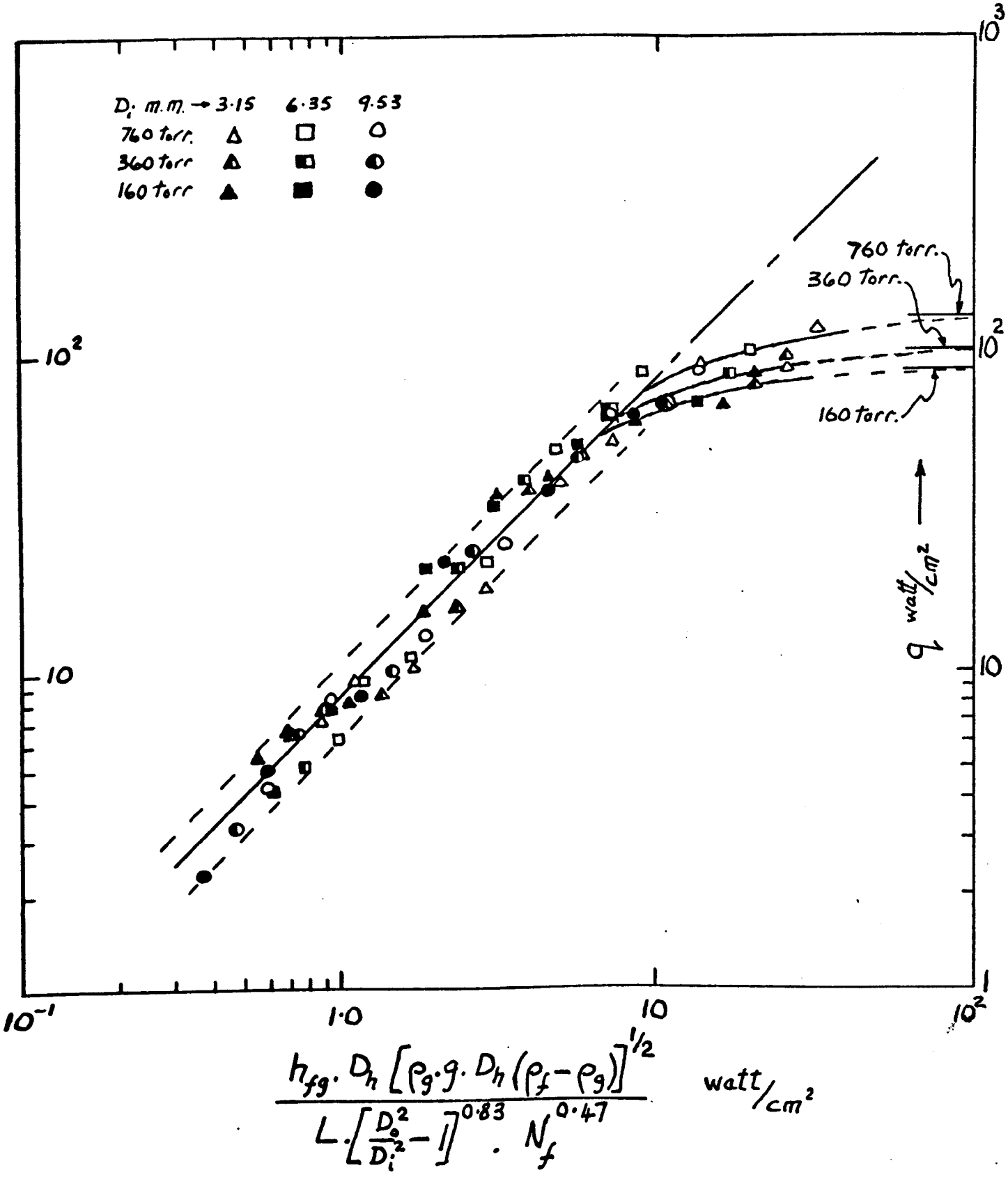

FIG. 16. VARIATION OF CRITICAL HEAT FLUX

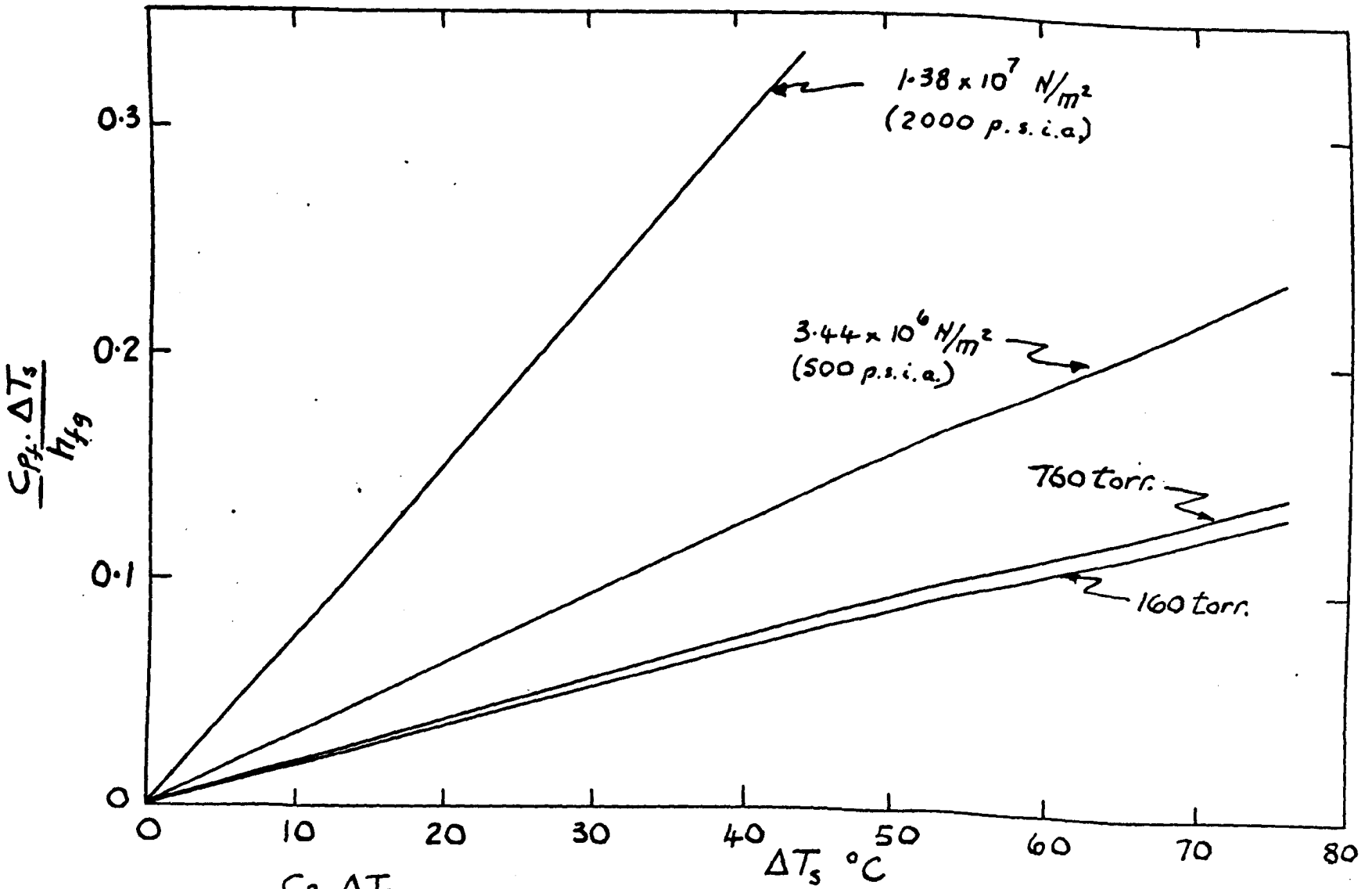

FIG. 17. $\frac{C_{p_f}.\Delta T_s}{h_{fg}}$ VERSUS POOL SUBCOOLING FOR DIFFERENT PRESSURES

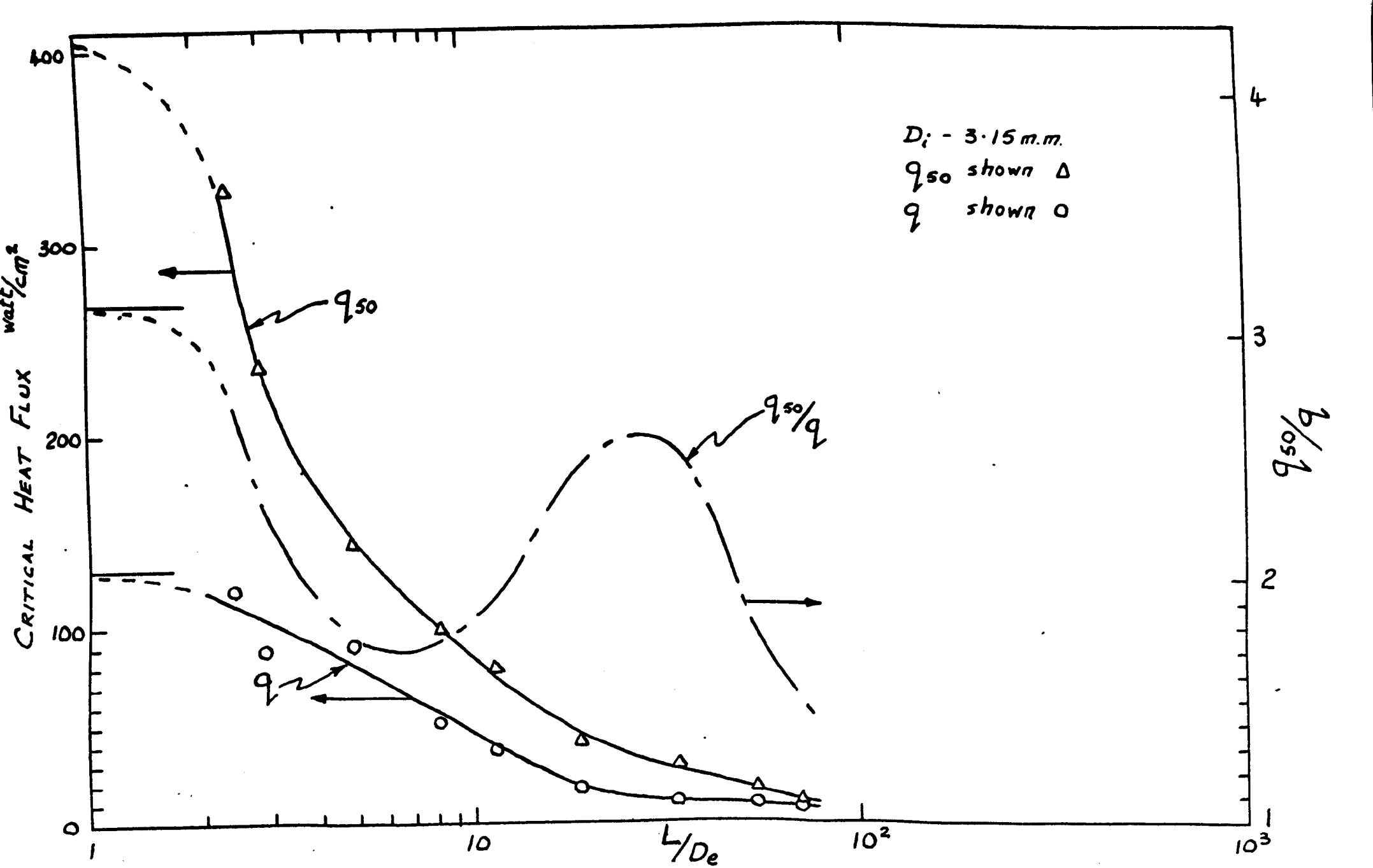

FIG. 18. q, q_{so}, AND q_{so}/q VERSUS L/D_e — PRESSURE 760 TORR.

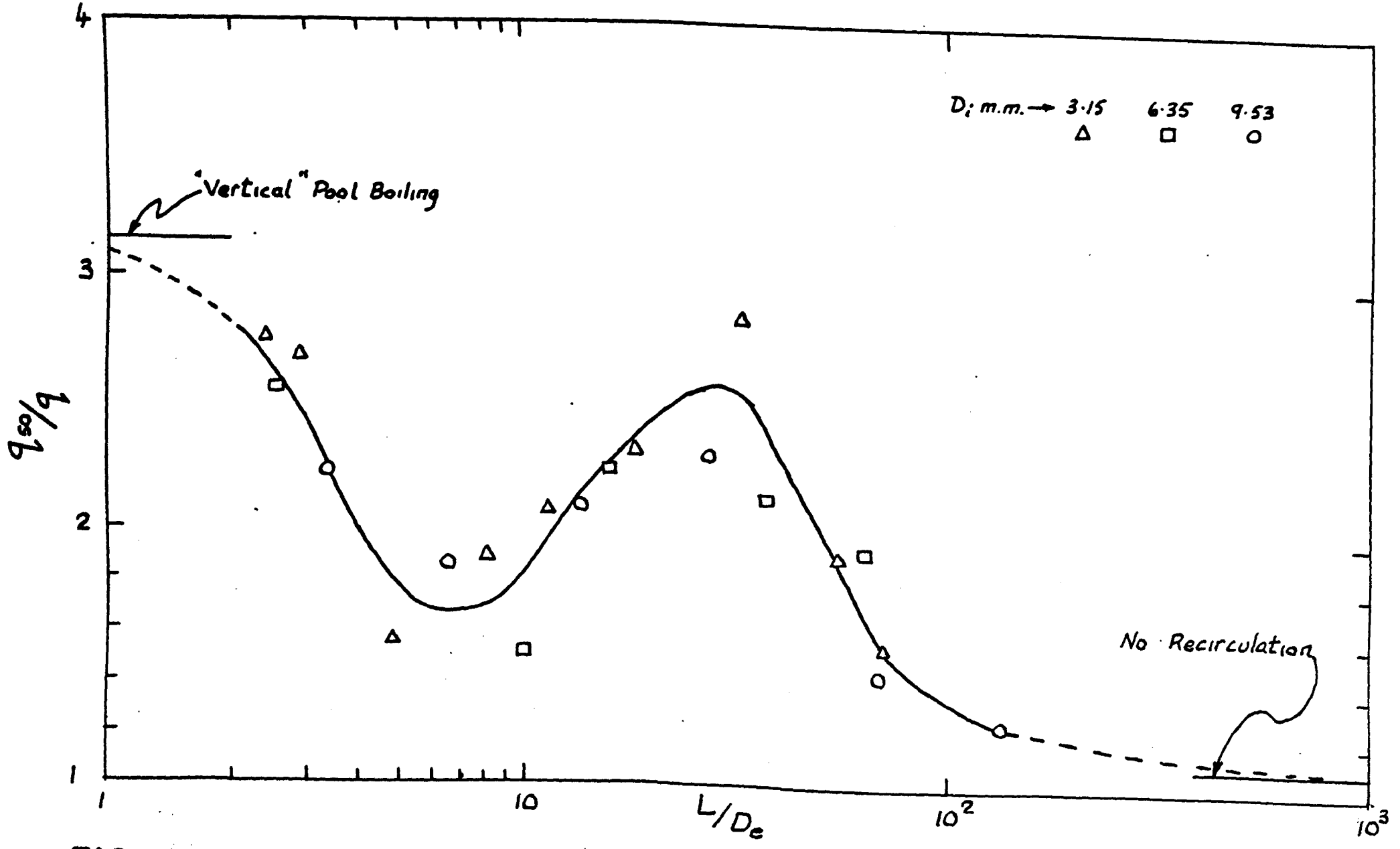

FIG. 19. VARIATION OF CRITICAL HEAT FLUX RATIO WITH L/D_e AT PRESSURE OF 760 TORR.

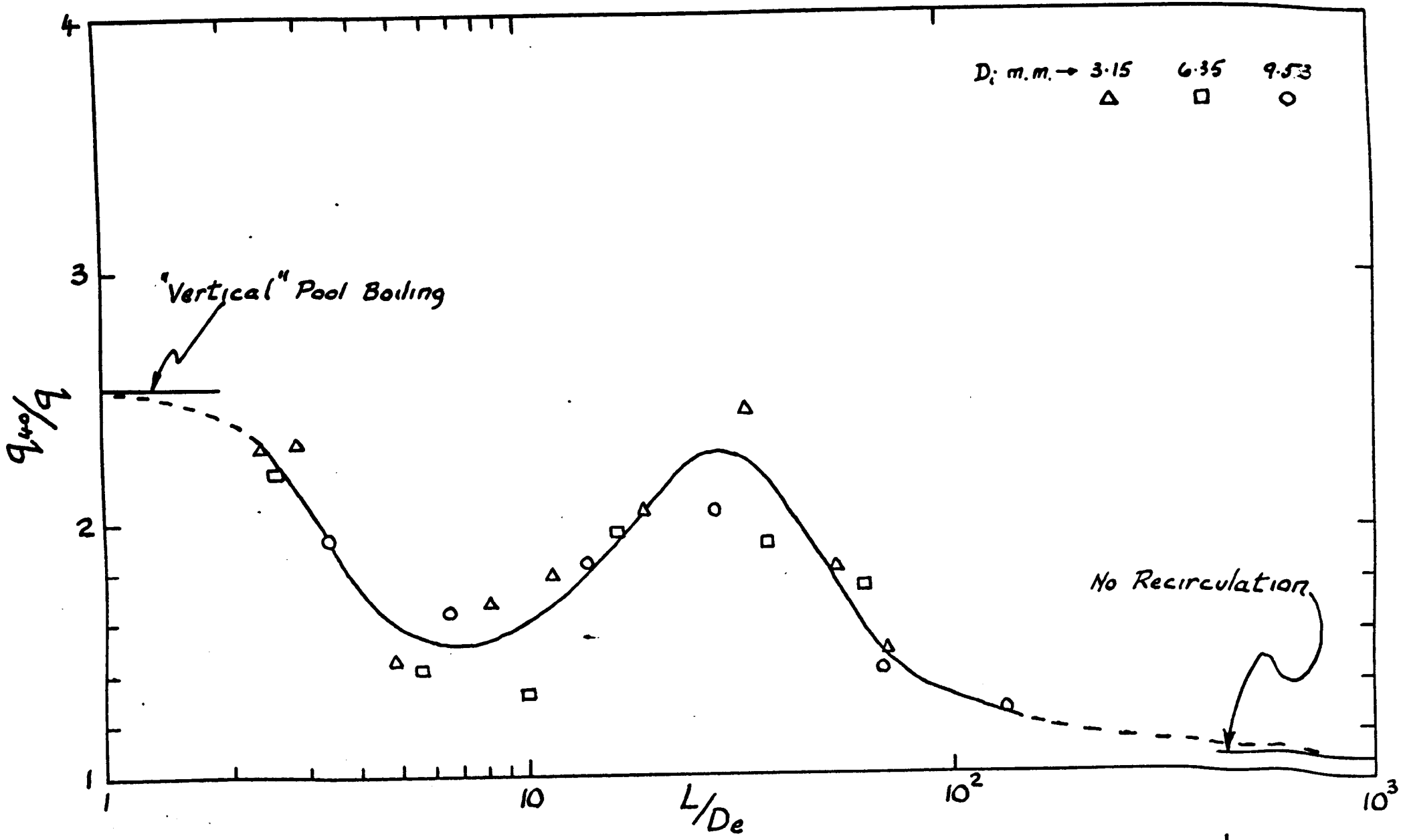

FIG. 20. VARIATION OF CRITICAL HEAT FLUX RATIO WITH L/D_e AT PRESSURE OF 760 TORR.

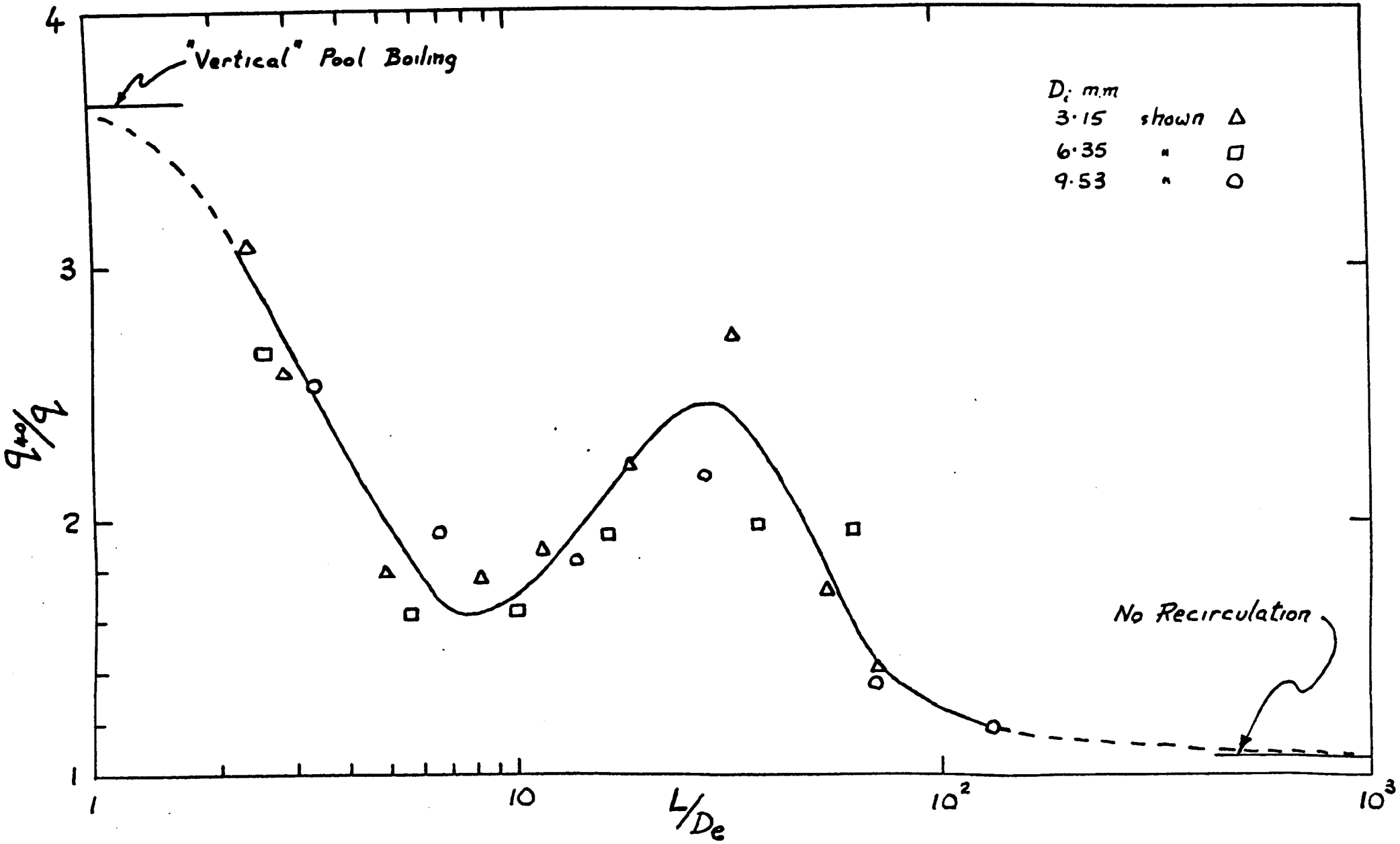

FIG. 21. VARIATION OF CRITICAL HEAT FLUX RATIO WITH L/D_e AT PRESSURE OF 360 TORR.

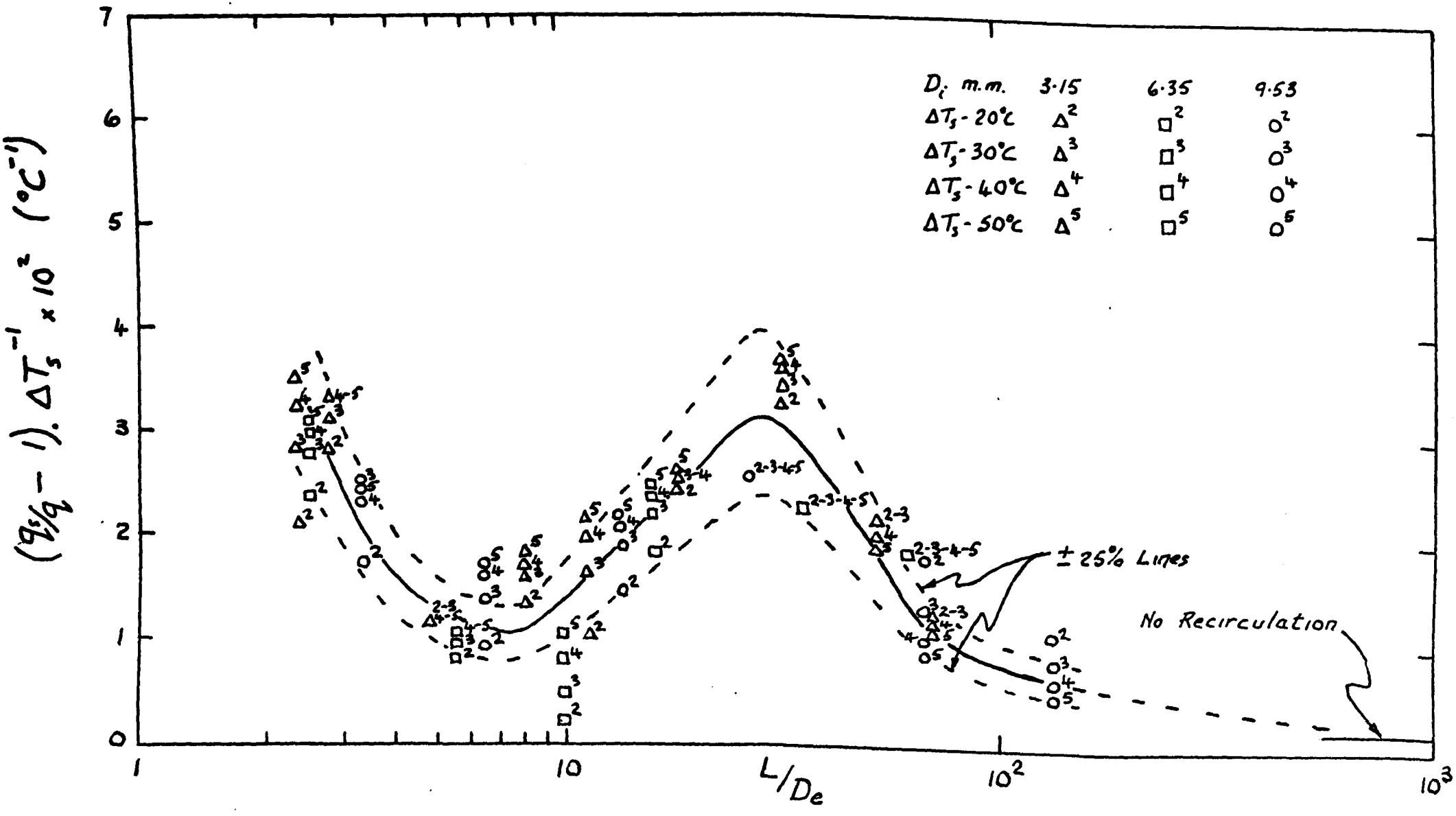

FIG. 22. POOL SUBCOOLING PARAMETER VERSUS L/D_e FOR PRESSURE OF 760 TORR.

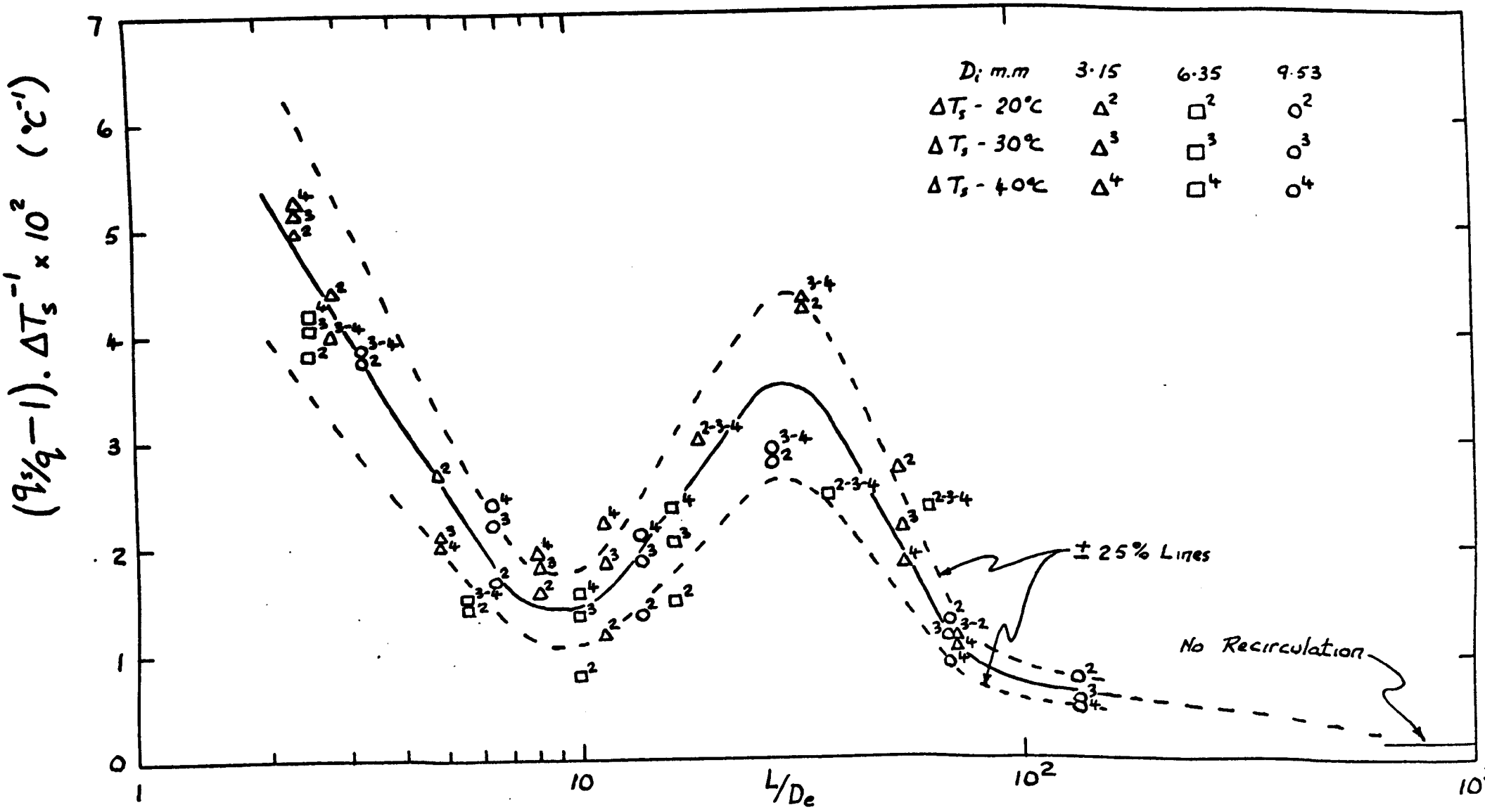

FIG. 23. POOL SUBCOOLING PARAMETER VERSUS L/D_e FOR PRESSURE OF 360 TORR.

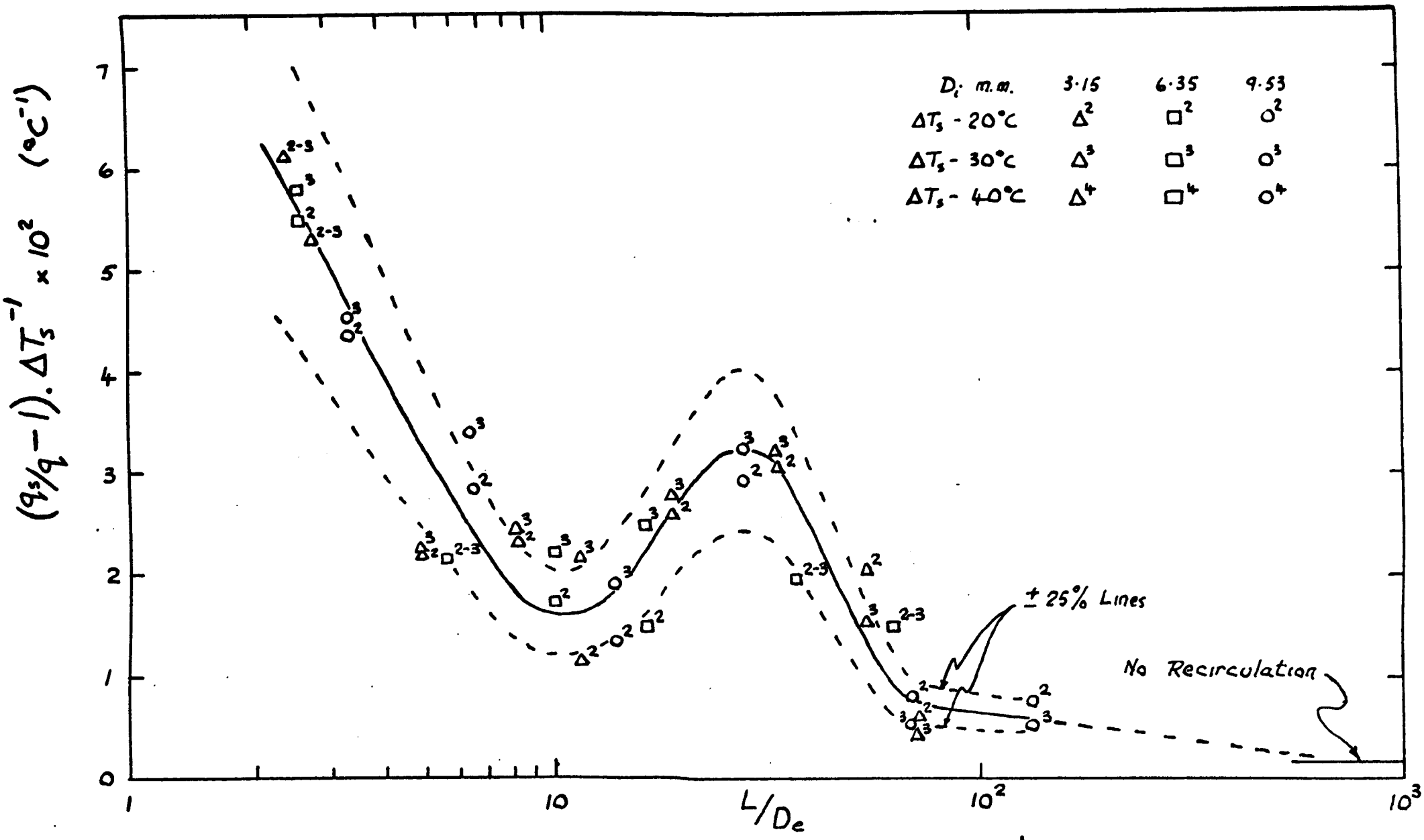

FIG. 24. POOL SUBCOOLING PARAMETER VERSUS L/D_e FOR PRESSURE OF 160 TORR.

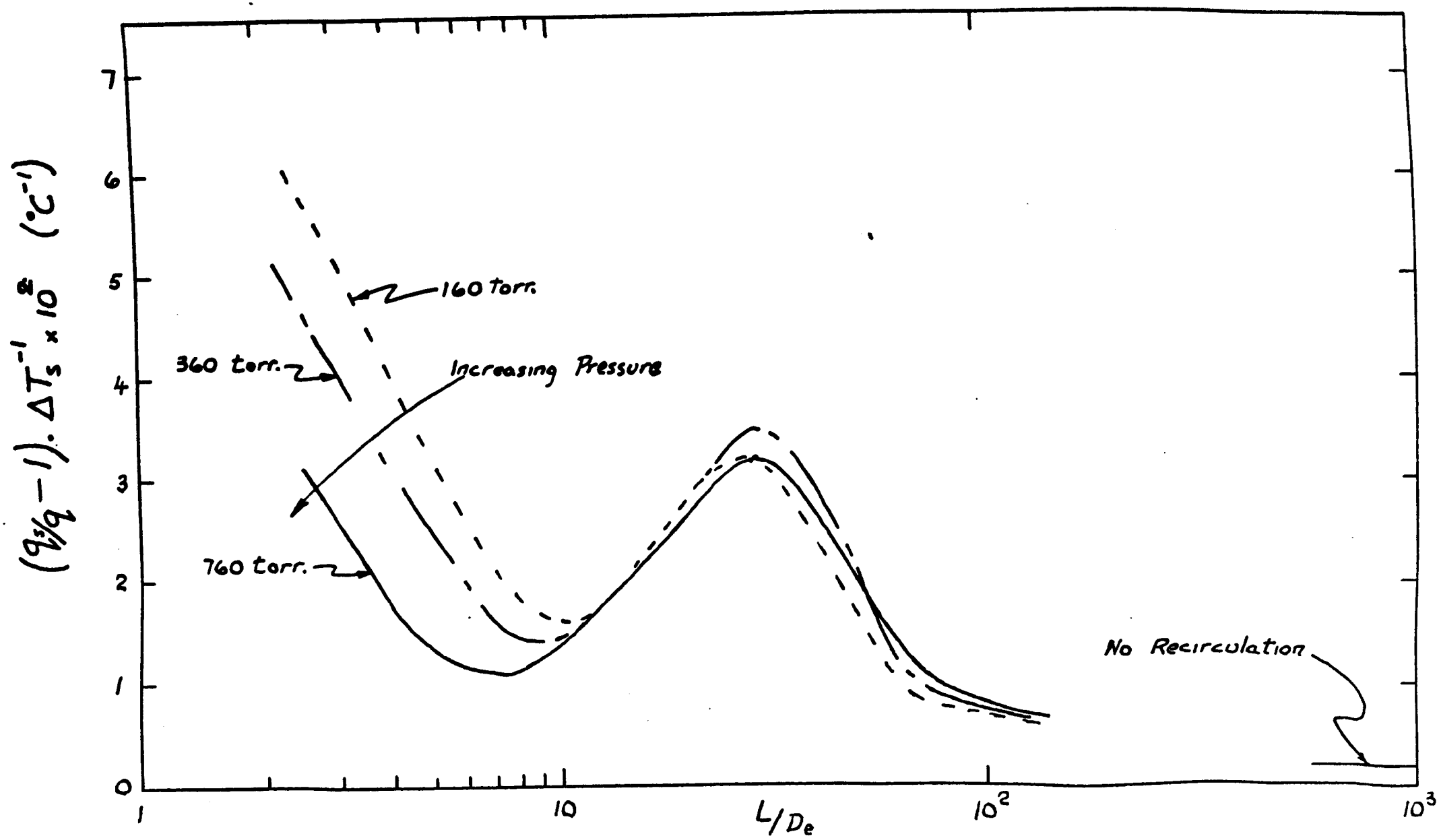

FIG. 25. POOL SUBCOOLING PARAMETER VERSUS L/D_e FOR PRESSURES OF 160, 360, AND 760 TORR.

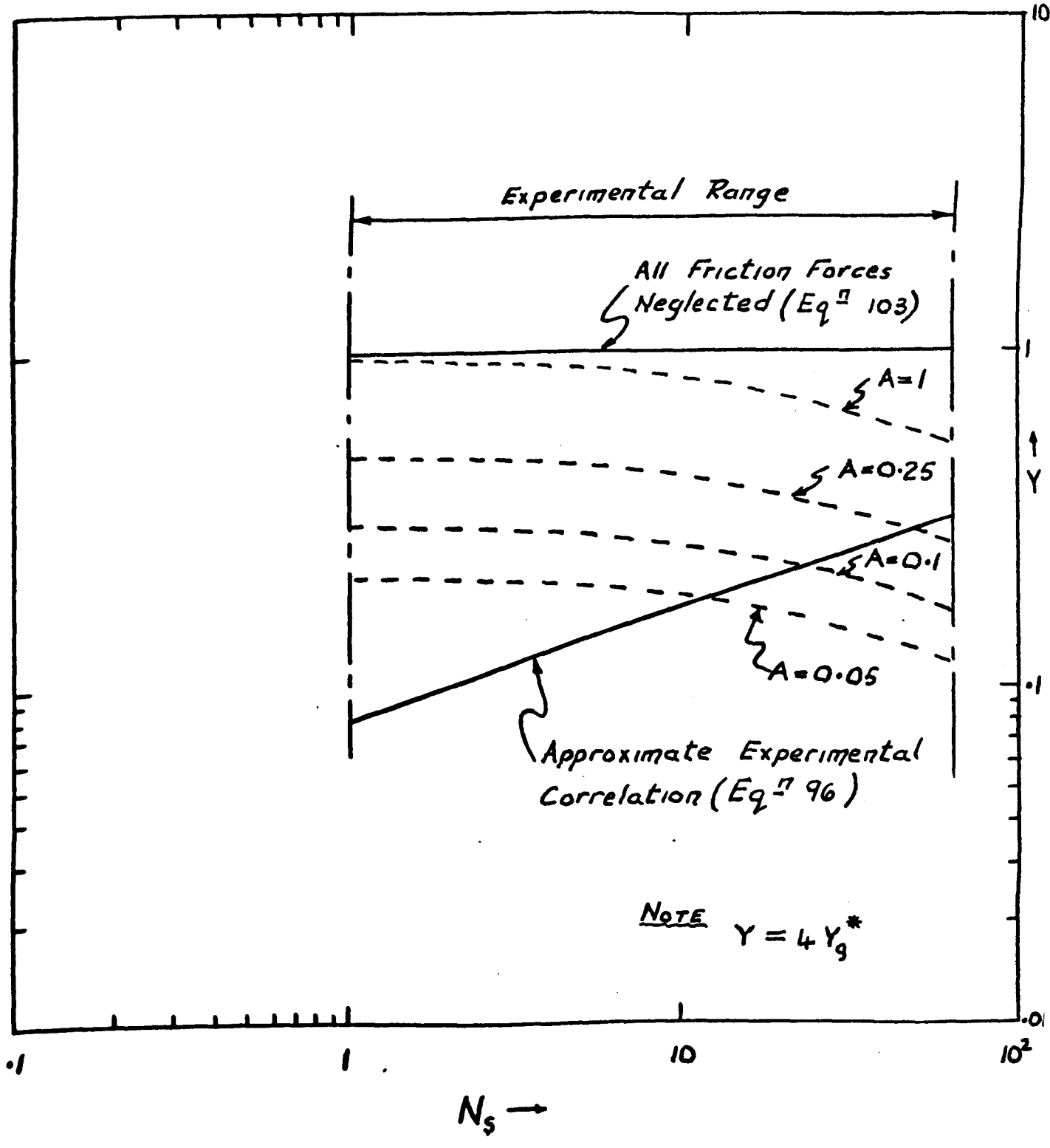

FIG. 26. COMPARISON OF MODEL PREDICTIONS WITH EXPERIMENT

1	2	3	4	5	6	7	8	9	10	11	12	13	14	15	16	17	18	19	20
Pressure (torr.)	D_o (cm)	D_h^{-1} (cm^{-1})	$N_s = (\frac{L}{D_h})$	q ($watt/cm^2$)	N_{Bi}	$\sqrt{N_e}$	$\sqrt{U}$	$\sqrt{\frac{N_g \cdot N_s}{U}} \times 10$	$J_g^* \times 10^2$	$\left(\frac{D_o^2}{D_i^2}-1\right)$	$\left(\frac{D_o^2}{D_i^2}-1\right)^{0.83}$	$N_f \times 10^{-3}$	$N_f^{0.47}$	$\left(\frac{D_o^2}{D_i^2}-1\right)^{0.83} \cdot N_f^{0.47}$	$g^{\frac{1}{2}} h_{fg} (\rho_g \cdot D_H(\beta))^{\frac{1}{2}}$ $\times 10^{-3}$ ($watt/cm^2$)	(16)/(4) ($watt/cm^2$)	(17)/(16) $watt/cm^2$	$Re_g \times 10^{-3}$	
760	1.05	5.1	63.1	4.4	0.023	0.33	40.0	0.66	52.4	0.21	0.27	9.75	74.7	20.2	0.75	11.9	0.59	4.46	
	1.13	2.53	31.4	8.2	0.079	0.44		0.61	34.2	0.42	0.48			36.2	1.06	33.9	0.94	7.97	
	1.4	0.91	11.3	13.0	0.199	0.42		0.35	11.8	1.15	1.12			83.9	1.77	156.5	1.86	11.2	
	1.85	0.38	4.7	25.2	0.75	0.52		0.28	6.12	2.76	2.32			173.3	2.74	583	3.36	18.2	
	2.87	0.12	1.6	64.0	4.82	0.74		0.23	3.0	8.07	5.65			422	4.90	3050	7.23	33.9	
	4.63	0.046	0.57	87.0	8.91	0.63		0.12	0.90	22.6	13.4			1001	7.86	13695	13.7	31.5	
360	1.05	5.1	63.1	3.3	0.049	0.49	57.1	0.68	53.9	0.21	0.27	7.98	68.0	18.3	0.54	8.6	0.47	3.41	
	1.13	2.53	31.4	6.5	0.194	0.68		0.67	37.6	0.42	0.48			33.0	0.76	24.4	0.74	6.51	
	1.4	0.91	11.3	9.9	0.45	0.63		0.37	12.4	1.15	1.12			76.4	1.28	112.7	1.47	8.82	
	1.85	0.38	4.7	23.9	2.63	0.98		0.37	8.05	2.76	2.32			158	1.98	420	2.66	17.9	
	2.87	0.12	1.6	47.0	10.2	1.07		0.24	3.04	8.07	5.65			384	3.54	2200	5.73	25.7	
	4.63	0.046	0.57	69.0	21.8	0.98		0.131	0.99	22.6	13.4			911	5.66	9870	10.8	25.8	
160	1.05	5.1	63.1	2.3	0.107	0.72	84.0	0.68	54.0	0.21	0.27	6.16	60.1	16.2	0.38	6.0	0.37	2.51	
	1.13	2.53	31.4	5.0	0.505	1.10		0.74	41.3	0.42	0.48			29.2	0.54	17.2	0.59	5.25	
	1.4	0.91	11.3	8.4	1.41	1.11		0.44	14.9	1.15	1.12			67.5	0.89	79.0	1.17	7.78	
	1.85	0.38	4.7	22.0	9.61	1.87		0.48	10.5	2.76	2.32			139.5	1.42	301.5	2.16	17.1	
	2.87	0.12	1.6	37.0	27.5	1.77		0.27	3.4	8.07	5.65			340	2.54	1578	4.65	21.1	
	4.63	0.046	0.57	64.0	82.0	1.90		0.17	1.3	22.6	13.4			805	3.96	6910	8.57	25.0	

FIG. 27 EXPERIMENTAL AND CALCULATED RESULTS FOR THE 9.53 m.m. DIA. (D_i) X 12.4 cm. LENGTH (L) ANNULUS HEATER WITH SATURATED ENTRY CONDITIONS

1	2	3	4	5	6	7	8	9	10	11	12	13	14	15	16	17	18	19	20
Pressure (torr)	D_o (cm)	D_h^{-1} (cm^{-1})	$N_s = (L/D_h)$	q (watt/cm^2)	$N_{e,i}$	$\sqrt{N_e}$	$\sqrt{U}$	$\sqrt{\frac{N_e \cdot N_s}{U}} \times 10$	$J_g^* \times 10^2$	$\left(\frac{D_o^2}{D_i^2}-1\right)$	$\left(\frac{D_o^2}{D_i^2}-1\right)^{0.83}$	$N_f \times 10^{-3}$	$N_f^{0.47}$	$\left(\frac{D_o^2}{D_i^2}-1\right)^{0.83} \cdot N_f^{0.47}$	$g^{1/2} h_{fg} (\rho_g D_h \rho_f)^{1/2} \times 10^{-3}$ (watt/cm^2)	(16)/(4) (watt/cm^2)	(17)/(15) (watt/cm^2)	$Re_g \times 10^{-3}$	
760	0.83	2.18	27.0	6.2	0.07	0.31	40.0	0.4	20.7	0.72	0.76	5.3	56.4	43.0	1.15	42.5	0.99	5.7	
	0.97	1.18	14.6	11.1	0.22	0.4		0.39	14.8	1.33	1.27			71.7	1.56	106.7	1.68	9.3	
	1.4	0.41	5.1	21.9	0.88	0.48		0.27	6.1	3.84	3.06			172	2.59	510	2.96	14.5	
	1.88	0.20	2.52	49.8	4.4	0.75		0.3	4.7	7.76	5.48			309	3.76	1492	4.83	26.7	
	2.87	0.081	1.0	86.5	13.3	0.82		0.21	2.1	19.4	11.7			660	5.95	5950	9.0	33.4	
	5.45	0.022	0.27	101.0	18.0	0.5		0.065	0.33	73.0	35.2			1985	10.5	38900	19.6	22.3	
360	0.83	2.18	27.0	5.1	0.18	0.5	57.1	0.45	23.6	0.72		4.34	51.1	39.0	0.83	30.6	0.78	4.85	
	0.97	1.18	14.6	9.3	0.6	0.67		0.45	17.1	1.33				65.0	1.13	76.9	1.18	8.1	
	1.4	0.41	5.1	21.0	3.18	0.91		0.36	8.1	3.84	ditto			156.0	1.87	368	2.36	14.4	
	1.88	0.20	2.52	39.4	10.7	1.17		0.33	5.2	7.76				280.0	2.71	1078	3.85	21.8	
	2.87	0.081	1.0	64.8	29.0	1.22		0.21	2.13	19.4				598	4.3	4300	7.19	25.8	
	5.45	0.022	0.27	85.0	29.1	0.63		0.06	0.3	73.0				1798	8.3	30750	17.1	19.5	
160	0.83	2.18	27.0	4.3	0.55	0.88	84.0	0.54	28.1	0.72		3.35	45.3	34.6	0.58	21.5	0.62	4.2	
	0.97	1.18	14.6	7.6	1.75	1.15		0.52	19.9	1.33				57.5	0.79	53.8	0.94	6.9	
	1.4	0.41	5.1	21.0	13.8	1.9		0.51	11.5	3.84	ditto			138.2	1.31	258	1.87	15.0	
	1.88	0.20	2.52	33.0	32.8	2.05		0.39	6.2	7.76				248	1.90	755	3.04	19.0	
	2.87	0.081	1.0	51.5	79.9	2.02		0.24	2.4	19.4				530	3.01	3010	5.68	21.4	
	5.45	0.022	0.27	70.5	150	1.43		0.09	0.46	73.0				1593	5.81	21520	13.5	16.8	

FIG 28 EXPERIMENTAL AND CALCULATED RESULTS FOR THE 6.35 m.m. DIA. (D_i) × 12.4 cm. LENGTH (L) ANNULUS HEATER WITH SATURATED ENTRY CONDITIONS

1	2	3	4	5	6	7	8	9	10	11	12	13	14	15	16	17	18	19	20
Pressure (torr.)	D_o (cm)	D_h^{-1} ($cm.^{-1}$)	$N_S = (L/D_h)$	q ($watt/cm^2$)	Ne	$\sqrt{Ne}$	$\sqrt{U}$	$\frac{\sqrt{Re.N_S}}{U} \times 10$	$J_g^* \times 10^2$	$\left(\frac{D_o^2}{D_i^2}-1\right)$	$\left(\frac{D_o^2}{D_i^2}-1\right)^{0.83}$	$N_f \times 10^{-3}$	$N_f^{0.47}$	$\left(\frac{D_o^2}{D_i^2}-1\right)^{0.83} \cdot N_f^{0.47}$	$j^{*\frac{1}{2}} h_{fg} \left(\frac{g \cdot D_h \rho_l}{\sigma}\right)^{\frac{1}{2}} \times 10^{-3}$ ($watt/cm^2$)	(16)/(4) ($watt/cm^2$)	(17)/(15) ($watt/cm^2$)	$Re_g \times 10^{-3}$	
760	0.97	0.37	4.63	18.0	1.15	0.37	40.0	0.2	4.3	8.48	5.9	1.85	34.2	202.5	2.77	598.5	2.95	9.4	
	1.4	0.17	2.11	38.6	5.31	0.53		0.19	2.8	18.7	11.3			388.5	4.10	1947	5.01	15.1	
	1.85	0.10	1.18	52.5	9.85	0.54		0.15	1.6	33.4	18.4			630	5.49	4650	7.38	16.3	
	2.87	0.039	0.47	92.0	30.2	0.61		0.10	0.71	82.0	38.7			1325	8.62	18,340	13.8	19.3	
	4.63	0.015	0.18	88.0	27.6	0.36		0.04	0.16	215	86.5			2960	14.0	76700	25.9	12.5	
	5.45	0.01	0.13	119.0	50.6	0.41		0.04	0.13	299.5	114			3905	16.5	126900	32.5	13.8	
360				15.9	3.52	0.64	57.1	0.24	5.22			1.51	31.2	184.4	2.0	431	2.34	8.5	
				37.1	19.1	1.01		0.26	3.74					354	2.96	1404	3.97	15.0	
	ditto	ditto	ditto	47.7	40.3	1.10		0.21	2.27	ditto	ditto			574	3.95	3,352	5.84	15.3	
				69.0	66	0.9		0.11	0.74					1208	6.22	13,240	11.0	15.0	
				80.0	88.8	0.64		0.048	0.21					2700	10.1	55,400	20.5	11.7	
				96.0	128.3	0.65		0.041	0.15					3557	11.9	91,500	25.7	11.5	
160				15.5	14.6	1.31	84.0	0.34	7.24			1.17	27.6	163.4	1.4	301	1.84	8.7	
				35.9	78.3	2.05		0.35	5.15					313.5	2.08	984	3.14	15.1	
	ditto	ditto	ditto	40.8	104.0	1.76		0.23	2.48	ditto	ditto			509	2.77	2,345	4.61	13.6	
				62.0	233	1.68		0.14	0.94					1070	4.35	9,260	8.65	14.0	
				78.0	369	1.31		0.067	0.28					2391	7.05	38,750	16.2	11.9	
				86.0	450	1.22		0.052	0.19					3150	8.34	64,200	20.4	10.7	

FIG. 29 EXPERIMENTAL AND CALCULATED RESULTS FOR THE 3.15 m.m. DIA. (D_i) × 12.4 cm. LENGTH (L) ANNULUS HEATER WITH SATURATED ENTRY CONDITIONS

1	2	3	4	5	6	7	8	9	10	11	12	13	14	15	16	17	18	19	20
Pressure (torr.)	D_o (cm.)	D_h^{-1} (cm^{-1})	$N_s = (L/D_h)$	q (watt/cm^2)	Ne	$\sqrt{Ne}$	$\sqrt{U}$	$\sqrt{\frac{Ne \cdot N_s}{U}} \times 10$	$J_g^* \times 10^2$	$\left(\frac{D_o^2}{D_i^2}-1\right)$	$\left(\frac{D_o^2}{D_i^2}-1\right)^{0.83}$	$N_f \times 10^{-3}$	$N_f^{0.47}$	$\left(\frac{D_o^2}{D_i^2}-1\right)^{0.83} \cdot N_f^{0.47}$	$g^{1/2} h_{fg} (\rho_g \cdot D_h \cdot P_H)^{1/2} \times 10^{-3}$ (watt/cm^2)	(19)/(4) (watt/cm^2)	(17)/(15) (watt/cm^2)	$Re_g \times 10^{-3}$	
760	0·5	2·12	27·6	7·1	0·18	0·348	40	0·456	24	1·5	1·4	1·85	34·2	48	1·16	42	0·88	6·2	
	0·56	1·5	19·5	9·3	0·31	0·381		0·421	18·5	2·12	1·87			64	1·38	71	1·11	7·5	
	0·71	0·79	10·2	10·2	0·42	0·304		0·274	7·8	4·02	3·17			108·6	1·91	183·4	1·72	7·0	
360	ditto	ditto	ditto	6·4	0·57	0·616	57·1	0·566	29·8	ditto	ditto	1·51	31·2	43·7	0·84	30·4	0·70	5·7	
				7·7	0·82	0·623		0·481	21·2					58·2	1·0	51·2	0·88	6·4	
				8·5	1·0	0·5		0·280	8·96					98·8	1·37	134	1·36	6·0	
160	ditto	ditto	ditto	5·5	1·84	1·11	84·0	0·694	36·5	ditto	ditto	1·17	27·6	38·7	0·59	21·3	0·55	5·1	
				6·6	2·63	1·11		0·585	25·8					51·5	0·7	35·9	0·70	5·7	
				8·0	3·9	0·98		0·374	12·0					87·6	0·96	94·1	1·07	5·9	

FIG 30. EXPERIMENTAL AND CALCULATED RESULTS FOR THE 3·15 m.m. DIA. (D_i) x 13·0 cm. LENGTH (L) ANNULUS HEATER WITH SATURATED ENTRY CONDITIONS

D_o (cm)	D_e (cm)	L/D_e	q watt/cm²			q_{20} watt/cm²			q_{20}/q			$\left(\frac{q_{20}}{q}-1\right)\Delta T_s^{-1}\times 10$		
			760 torr	360 torr	160 torr	760 torr	360 torr	160 torr	760 torr	360 torr	160 torr	760 torr	360 torr	160 torr
1.05	.094	132	4.4	3.3	2.3	5.4	3.8	2.7	1.22	1.15	1.15	1.12	0.76	0.75
1.13	.18	68.7	8.2	6.5	5.0	11.2	8.5	5.8	1.37	1.31	1.16	1.83	1.54	0.80
1.4	.445	27.8	13.0	9.9	8.4	19.7	15.4	13.3	1.51	1.55	1.58	2.57	2.77	2.91
1.85	.895	13.8	25.2	23.9	22	32.6	30.3	27.9	1.29	1.27	1.27	1.47	1.34	1.54
2.87	1.92	6.5	64	47	37	76.0	62.5	58.0	1.19	1.33	1.57	0.93	1.65	2.84
4.63	3.68	3.4	87	69	64	117	121	120	1.34	1.75	1.87	1.72	3.76	4.37

D_o (cm)	D_e (cm)	L/D_e	q watt/cm²			q_{30} watt/cm²			q_{30}/q			$\left(\frac{q_{30}}{q}-1\right)\Delta T_s^{-1}\times 10^2$		
			760 torr.	360 torr	160 torr	760 torr.	360 torr.	160 torr.	760 torr.	360 torr.	160 torr.	760 torr.	360 torr.	160 torr.
ditto			ditto			5.5	3.82	2.67	1.25	1.17	1.16	0.83	0.56	0.52
						11.4	8.7	5.8	1.4	1.34	1.16	1.33	1.13	0.53
						23.1	18.5	16.5	1.78	1.87	1.97	2.6	2.91	3.23
						39.4	37.2	34.5	1.56	1.55	1.57	1.88	1.85	1.9
						90.0	78.0	75.0	1.41	1.66	2.03	1.37	2.2	3.4
						153	14.9	151	1.76	2.16	2.36	2.5	3.9	4.5

D_i (cm)	D_e (cm)	L/D_e	q watt/cm²			q_{40} watt/cm²			q_{40}/q			$\left(\frac{q_{40}}{q}-1\right)\Delta T_s^{-1}\times 10^2$		
			760 torr	360 torr	160 torr	760 torr.	360 torr.		760 torr.	360 torr.		760 torr.	360 torr.	
ditto			ditto			5.54	3.9		1.26	1.19		0.64	0.47	
						11.6	8.8		1.41	1.36		1.04	0.89	
						26.5	21.5		2.04	2.17		2.61	2.94	
						46.2	44		1.83	1.84		2.09	2.10	
						105	92		1.64	1.95		1.61	2.39	
						168	175		1.93	2.54		2.33	3.84	

D_o (cm)	D_e (cm)	L/D_e	q watt/cm²			q_{50} watt/cm²			q_{50}/q			$\left(\frac{q_{50}}{q}-1\right)\Delta T_s^{-1}\times 10^2$		
			760 torr.	360 torr.	160 torr.	760 torr.			760 torr.			760 torr		
ditto			ditto			5.54			1.26			0.51		
						11.8			1.44			0.88		
						30.0			2.31			2.62		
						53.0			2.10			2.21		
						119			1.86			1.72		
						194			2.23			2.46		

FIG 31 EXPERIMENTAL AND CALCULATED RESULTS FOR THE 9.53 m.m. DIA. (D_i) × 12.4 cm. LENGH (L) ANNULUS HEATER WITH SUBCOOLED ENTRY CONDITIONS

D_o (cm)	D_e (cm)	L/De	q (watt/cm²)			q_{20} watt/cm²			q_{20}/q			$\left(\frac{q_{20}}{q}-1\right)\Delta T_s^{-1}\times 10^2$		
			760 torr	360 torr	160 torr	760 torr	360 torr	160 torr	760 torr	360 torr	160 torr	760 torr	360 torr	160 torr
0·83	·198	62·5	6·2	5·1	4·3	8·5	7·5	5·6	1·37	1·47	1·30	1·86	2·35	1·51
0·97	·335	36·9	11·1	9·3	7·6	16·2	13·9	10·5	1·46	1·49	1·38	2·3	2·48	1·91
1·4	·76	16·2	21·9	21·0	21·0	30	26·9	27·2	1·37	1·28	1·29	1·85	1·45	1·47
1·88	1·24	10	49·8	39·4	33·0	52	45·5	44·3	1·04	1·15	1·34	0·22	0·77	1·71
2·87	2·24	5·5	86·5	64·8	51·5	100	83	73·5	1·16	1·28	1·43	0·81	1·4	2·14
5·45	4·82	2·56	101	85·0	70·5	149	150	148	1·48	1·76	2·1	2·38	3·82	5·5
D_o (cm)	D_e (cm)	L/De	q watt/cm²			q_{30} watt/cm²			q_{30}/q			$\left(\frac{q_{30}}{q}-1\right)\Delta T_s^{-1}\times 10^2$		
			760 torr	360 torr	160 torr	760 torr	360 torr	160 torr	760 torr	360 torr	160 torr	760 torr	360 torr	160 torr
ditto			ditto			9·7	8·7	6·2	1·56	1·70	1·45	1·88	2·35	1·49
						18·7	16·2	12·1	1·69	1·74	1·59	2·29	2·47	1·96
						36·5	33·8	32·4	1·66	1·61	1·74	2·22	2·03	2·47
						57·0	55·3	55·0	1·14	1·40	1·67	0·48	1·34	2·22
						112	94·2	84·5	1·29	1·45	1·64	0·97	1·51	2·13
						185	188	193	1·84	2·21	2·74	2·79	4·04	5·8
D_o (cm)	D_e (cm)	L/De	q watt/cm²			q_{40} watt/cm²			q_{40}/q			$\left(\frac{q_{40}}{q}-1\right)\Delta T_s^{-1}\times 10^2$		
			760 torr	360 torr	160 torr	760 torr	360 torr		760 torr	360 torr		760 torr	360 torr	
ditto			ditto			10·8	10		1·74	1·96		1·85	2·4	
						21·2	18·5		1·91	1·99		2·28	2·48	
						43	40·8		1·96	1·94		2·4	2·36	
						66	64·8		1·32	1·64		0·81	1·61	
						123	105·5		1·42	1·63		1·06	1·57	
						221	227		2·2	2·67		2·99	4·18	
D_o (cm)	D_e (cm)	L/De	q watt/cm²			q_{50} watt/cm²			q_{50}/q			$\left(\frac{q_{50}}{q}-1\right)\Delta T_s^{-1}\times 10^2$		
			760 torr	360 torr	160 torr	760 torr			760 torr			760 torr		
ditto			ditto			12·0			1·94			1·87		
						23·7			2·14			2·27		
						49·5			2·26			2·51		
						75·5			1·52			1·03		
						134			1·55			1·10		
						258			2·56			3·12		

FIG 32 EXPERIMENTAL AND CALCULATED RESULTS FOR THE 6·35 m.m. DIA. (D_i) × 12·4 cm LENGTH (L) ANNULUS HEATER WITH SUBCOOLED ENTRY CONDITIONS

D_o (cm)	D_e (cm)	L/D_e	q watt/cm² 760 torr	q watt/cm² 360 torr	q watt/cm² 160 torr	q_{20} watt/cm² 760 torr	q_{20} watt/cm² 360 torr	q_{20} watt/cm² 160 torr	q_{20}/q 760 torr	q_{20}/q 360 torr	q_{20}/q 160 torr	$(q_{20}/q-1)\Delta T_s^{-1}\times 10^2$ 760 torr	$(q_{20}/q-1)\Delta T_s^{-1}\times 10^2$ 360 torr	$(q_{20}/q-1)\Delta T_s^{-1}\times 10^2$ 160 torr
0.97	0.655	18.9	18	15.9	15.5	26.8	25.3	23.5	1.49	1.59	1.52	2.45	3.0	2.58
1.4	1.08	11.4	38.6	37.1	35.9	46.5	45.5	44	1.20	1.23	1.23	1.03	1.13	1.13
1.85	1.53	8.1	52.5	47.7	40.8	66.5	62.5	59.5	1.27	1.31	1.46	1.33	1.55	2.3
2.87	2.55	4.8	92	69	62	114	99	89	1.24	1.44	1.44	1.19	2.67	2.18
4.63	5.15	2.4	119	96	86	169	191	191	1.42	1.99	2.22	2.1	4.95	6.1
5.45	4.32	2.9	88	180	78	138	144	161	1.57	1.88	2.06	2.84	4.4	5.3

D_o (cm)	D_e (cm)	L/D_e	q watt/cm² 760 torr	q watt/cm² 360 torr	q watt/cm² 160 torr	q_{30} watt/cm² 760 torr	q_{30} watt/cm² 360 torr	q_{30} watt/cm² 160 torr	q_{30}/q 760 torr	q_{30}/q 360 torr	q_{30}/q 160 torr	$(q_{30}/q-1)\Delta T_s^{-1}\times 10^2$ 760 torr	$(q_{30}/q-1)\Delta T_s^{-1}\times 10^2$ 360 torr	$(q_{30}/q-1)\Delta T_s^{-1}\times 10^2$ 160 torr
ditto			ditto			31.8	30.2	28.4	1.77	1.90	1.83	2.56	3.0	2.77
						57.7	57.5	59.0	1.5	1.55	1.64	1.65	1.83	2.14
						77.6	73.4	70.5	1.48	1.54	1.73	1.59	1.80	2.43
						124	112	104	1.35	1.62	1.68	1.16	2.08	2.26
						221	244	244	1.86	2.54	2.84	2.85	5.13	6.13
						171	176	202	1.94	2.2	2.59	3.13	4.0	5.3

D_o (cm)	D_e (cm)	L/D_e	q watt/cm² 760 torr	q watt/cm² 360 torr	q watt/cm² 160 torr	q_{40} watt/cm² 760 torr	q_{40} watt/cm² 360 torr		q_{40}/q 760 torr	q_{40}/q 360 torr		$(q_{40}/q-1)\Delta T_s^{-1}\times 10^2$ 760 torr	$(q_{40}/q-1)\Delta T_s^{-1}\times 10^2$ 360 torr	
ditto			ditto			36.8	35.4		2.05	2.22		2.62	3.06	
						69.2	70.0		1.79	1.89		1.98	2.22	
						88.5	84.3		1.68	1.77		1.71	1.92	
						134	124		1.46	1.8		1.15	1.99	
						274	297		2.3	3.09		3.25	5.23	
						204	207		2.32	2.59		3.3	3.98	

D_o (cm)	D_e (cm)	L/D_e	q watt/cm² 760 torr	q watt/cm² 360 torr	q watt/cm² 160 torr	q_{50} watt/cm² 760 torr			q_{50}/q 760 torr			$(q_{50}/q-1)\Delta T_s^{-1}\times 10^2$ 760 torr		
ditto			ditto			41.8			2.32			2.65		
						80.5			2.08			2.17		
						99.6			1.89			1.79		
						144			1.56			1.13		
						328			2.76			3.52		
						237			2.69			3.38		

FIG 33 EXPERIMENTAL AND CALCULATED RESULTS FOR THE 3·15 m.m. DIA. (D_i) × 12·4 cm. LENGTH (L) ANNULUS HEATER WITH SUBCOOLED ENTRY CONDITIONS

D_o (cm)	D_e (cm)	L/D_e	q watt/cm²			q_{20} watt/cm²			q_{20}/q			$(q_{20}/q - 1)\cdot\Delta T_s^{-1} \times 10^2$		
			760 torr	360 torr	160 torr	760 torr	360 torr	160 torr	760 torr	360 torr	160 torr	760 torr	360 torr	160 torr
0·5	·183	71·2	7·1	6·4	5·5	9·0	7·95	6·15	1·27	1·24	1·12	1·34	1·21	0·59
0·66	·242	53·9	9·3	7·7	6·6	13·5	11·9	9·3	1·45	1·54	1·41	2·25	2·72	2·05
0·71	·291	33·3	10·2	2·5	8·0	16·9	15·7	12·9	1·66	1·85	1·61	3·28	4·24	3·06
D_o (cm)	D_e (cm)	L/D_e	q watt/cm²			q_{30} watt/cm²			q_{20}/q			$(q_{30}/q - 1)\cdot\Delta T_s^{-1} \times 10^2$		
			760 torr	360 torr	160 torr	760 torr	360 torr	160 torr	760 torr	360 torr	160 torr	760 torr	360 torr	160 torr
ditto			ditto			9·9	8·6	6·2	1·39	1·35	1·13	1·3	1·15	0·42
						15·4	12·7	9·6	1·66	1·65	1·46	2·19	2·17	1·53
						20·8	19·5	15·7	2·04	2·29	1·96	3·47	4·32	3·21
D_o (cm)	D_e (cm)	L/D_e	q watt/cm²			q_{40} watt/cm²			q_{40}/q			$(q_{40}/q - 1)\Delta T_s^{-1} \times 10^2$		
			760 torr	360 torr	160 torr	760 torr	360 torr		760 torr	360 torr		760 torr	360 torr	
ditto			ditto			10·6	9·1		1·49	1·42		1·22	1·05	
						16·8	13·2		1·81	1·73		2·03	1·83	
						25·0	23·3		2·45	2·74		3·63	4·35	
D_o (cm)	D_e (cm)	L/D_e	q watt/cm²			q_{50} watt/cm²			q_{50}/q			$(q_{50}/q - 1)\Delta T_s^{-1} \times 10^2$		
			760 torr	360 torr	160 torr	760 torr			760 torr			760 torr		
ditto			ditto			11·1			1·56			1·11		
						17·7			1·91			1·81		
						29·1			2·85			3·7		

FIG 34 EXPERIMENTAL AND CALCULATED RESULTS FOR THE 3·15 m.m. DIA. (D_i) x 13·0 cm. LENGH (L) ANNULUS HEATER WITH SUBCOOLED ENTRY

THE CRITICAL HEAT FLUX UNDER POOL BOILING AND CONFINED BOILING CONDITIONS

by

J. A. RILEY

This research project entailed investigation of the critical heat flux behaviour for horizontally orientated self heated heaters under low pressure pool boiling conditions, and for vertically orientated self heated heaters under low pressure pool boiling and confined boiling conditions. The confined boiling condition was obtained by mounting the tubular heater vertically and surrounding this heater by a thermally insulated glass tube which formed an adiabatic outer surface. The base of this annular assembly was sealed so that, under boiling conditions, the water entering the annulus did so in opposition to the vapour outflow.

The rig developed for this investigation consisted essentially of a spherically bottomed glass boiling cell 30 cm in diameter and 37 cm high which contained the distilled water and the heater assembly. The rig services and sensors were taken into the boiling cell via. a stainless steel lined Tufnol top which formed the boiling cell closure. The heaters were driven electrically using a low voltage-high current supply. Rig vacuum was obtained using two stainless steel water jet pumps working in parallel. The rig was suitably controlled and instrumented.

For pool boiling, both horizontal and vertical heater placement have been investigated. Stainless steel tubular and rod heaters were used. Critical heat fluxes were determined at atmospheric pressure and under vacuum for sub-cooled and saturated pool water conditions. These results have been correlated and compared with other workers results where possible.

Confined geometry boiling conditions were investigated for the annulus geometry with the inner surface heated and the outer surface adiabatic. Annuli of different sizes were used but the assembly length was not varied. Critical heat fluxes have been determined for each annulus geometry under atmospheric pressure and vacuum for both saturated and sub-cooled pool conditions.

A one dimensional separated flow model has been developed which (a) predicts a dimensionless vapour velocity parameter as a relevant variable and (b) predicts the correlating format used to correlate the annulus sub-cooled water entry critical heat flux results. The annulus saturated water entry critical heat flux results both at atmospheric pressure and under vacuum were successfully correlated using a dimensionless vapour velocity parameter whose characteristic dimension is the annulus heated equivalent diameter. The annulus sub-cooled water entry critical heat flux results both at atmospheric pressure and under vacuum were successfully correlated using a dimensionless parameter that was predicted by the mathematical model developed.

It has been shown that for such confined geometry conditions in which vapour momentum forces may be important as well as frictional and buoyancy forces, that the critical heat flux behaviour should be correlated in terms of parameters which contain two of the following dimensionless quantities: J_g^*, Y_g^* and N_s. J_g^* is a dimensionless parameter that is proportional to the ratio of the relevant system shear forces to the system buoyancy forces. Y_g^* is a dimensionless parameter that is proportional to the ratio of the relevant system momentum forces to the system buoyancy forces. N_s is a dimensionless parameter that is proportional to the ratio of the relevant system shear forces to the relevant system momentum forces.